NTNU
Norwegian University of
Science and Technology

Breakdown at Multiple Protrusions and Surface Roughness in SF6 and CO2

A Study of the Enlargement Law

Odd Christian Feet

Master of Energy and Environmental Engineering
Submission date: August 2018
Supervisor: Kaveh Niayesh, IEL
Co-supervisor: Frank Mauseth, IEL
Martin Seeger, ABB

Norwegian University of Science and Technology
Department of Electric Power Engineering

Summary

Gas insulated components are important in the modern transmission system. The most common gas used in high pressure insulation is Sulphur Hexafluoride (SF_6). SF_6 has been classified as a greenhouse gas and a potential replacement is CO_2, either by itself or in mixtures with other gases. The insulation properties of gas insulation depends on several parameters, e.g. surface roughness. An electrode with a built-in precision motor was used in a quasi-uniform gap. This thesis aims to investigate the impact of needle protrusions with lengths in the range 0.05 – 2 mm in SF_6 at 4 bar absolute pressure and CO_2 at 6 bar absolute pressure. Another aim is to investigate the applicability of the enlargement law. The results with a single needle were used to create predictions, according to the enlargement law, for 20 and 100 identical needle protrusions. The electrode used allowed needle arrays of 20 and 100 needles to be tested with needle lengths in the range 0.05 – 2 mm. The enlargement law was also investigated for two sandblasted surface areas.

The results in SF_6 showed a decrease in the 50 % average background breakdown field, E_{50}, with increasing needle lengths for both polarities. With 20 needles E_{50} decreased from the single needle results and agreed well with the predictions for both polarities. With positive polarity and 100 needles, there was no significant change in the results between the 20 and 100 needles and there was a discrepancy with the predictions. With 100 negative needles there was a good agreement between predictions and results, showing a decrease from the results with 20 needles. The sandblasted surfaces showed a decrease from the small area (2.383 cm^2) to the large area (64.465 cm^2). The reduction in E_{50} showed good agreement with predictions with negative and disagreed significantly with positive polarity.

The obtained results in CO_2 showed an insensitivity to single needle protrusion with needle lengths shorter than 1 mm with positive and 0.75 mm with negative polarity. With 20 needles, there was an increased sensitivity and reduction for both polarities. E_{50} with positive polarity decreased with increasing needle lengths. Negative polarity had a significant decrease of E_{50} from 0.1 to 0.5 mm where it seemed to saturate between 0.5 – 2 mm needle lengths. For 20 needles both polarities agreed well with predictions. With 100 needles, there was no longer an agreement between predictions and results for either polarities. the results with positive polarity decreased further. With negative polarity similar behavior as with 20 needles was seen, where the saturation occurred at 0.2 mm needle lengths and ended at the same field strengths as with 20 needles. The sandblasted surfaces showed much more of a decrease than what was predicted based on the small area.

The experimental results were analyzed with *Turnbull's algorithm* to determine the empirical cumulative distribution function, which was fitted with the three parameter Weibull distribution. From the distribution functions the 2 % average background breakdown field was found. Possible physical explanations and breakdown mechanisms of the results were discussed. The results showed that SF_6 was more sensitive to the needle protrusion than CO_2. The main conclusion is that the enlargement law must be used with care. It is possible that the mechanisms involved in breakdowns scale differently than just with increased number of needles or area and require further investigation to understand.

Sammendrag

Gassisolerte komponenter er viktige i det moderne strømnettet. Den mest brukte gassen i isolasjon under høyt trykk er Svovelheksafluorid (SF_6). SF_6 er klassifisert som en drivhusgass og en mulig erstatter er CO_2, enten alene eller i blandinger med andre gasser. Isolasjonsegenskapene til gassisolasjon er avhengig av flere parametre, f.eks. overflateruhet. En elektrode med en presisjonsmotor innebygd ble brukt i et tilnærmet uniformt gap. Denne avhandlingen har som mål å undersøke virkningen av nåler med lengder fra 0.05 til 2 mm i SF_6 med 4 bar absolutt trykk og CO_2 med 6 bar absolutt trykk. Et annet mål er å undersøke anvendbarheten til utvidelsesloven (Enlargement law). Resultatene med en enkelt nål ble brukt til å lage prediksjoner, etter utvidelsesloven, for 20 og 100 identiske nåler. Elektroden som ble brukt tillot et matriseoppsett med 20 og 100 nåler som kunne testes med lengder fra 0.05 til 2 mm. Utvidelsesloven ble også undersøkt for to sandblåste overflater med forskjellig areal.

Resultatene i SF_6 viste, for begge polariteter, en reduksjon i 50 % gjennomsnittlig bakgrunns gjennomslagsfeltet, E_{50}, med økende nållengder. Med 20 nåler ble E_{50} redusert fra resultatene med enklet nål for begge polaritetene og stemte godt overens med prediksjonene. Med positiv polaritet og 100 nåler var det ingen signifikant endring mellom 20 og 100 nåler. Det var også et avvik mellom resultatene og prediksjonene. Med negativ polaritet og 100 nåler stemte resultatene godt overens med prediksjonene og viste en reduksjon fra resultatene med 20 nåler. De sandblåste overflatene viste en reduksjon fra det lille arealet (2.383 cm^2) til det store arealet (64.465 cm^2). Resultatene stemte godt overens med prediksjonene for negative polaritet, positiv polaritet hadde et signifikant avvik.

Resultatene i CO_2 viste en ufølsomhet til den enkle nålen med lengder kortere enn 1 mm med positiv polaritet og kortere enn 0.75 mm med negativ polaritet. Med 20 nåler var det en reduksjon for økende nållengder, som startet tidligere enn for en enkelt nål. For negativ polaritet kom en reduksjon mellom 0.1 og 0.5 mm, hvor resultatene nådde en horisontal asymptote for økende nållengder. Med 20 nåler stemte resultatene godt overens med prediksjonene. Med 100 nåler var det signifikante avvik for begge polaritetene. Med positive polaritet ble E_{50} redusert fra 20 nåler. Med negativ polaritet og 100 nåler ble samme oppførsel som med 20 nåler observert, hvor asymptoten ble nådd med 0.2 mm nåler. De sandblåste overflatene viste også større reduksjoner enn hva prediksjonene forutså.

De eksperimentelle resultatene ble analysert med *Turnbulls algoritme* for å fastslå den empirisk kumulative fordelingsfunksjonen, som ble kurvetilpasset til Weibullfordelingen med tre parametre. Fra fordelingsfunksjonene ble 2 % gjennomsnittlig bakgrunn gjennomslagssfeltet funnet. Mulige fysiske forklaringen og sammenbruddsmekanismer til resultatene ble diskutert. Resultatene viser at SF_6 er mer følsom til nålene enn CO_2. Hovedkonklusjonen er at utvidelsesloven må brukes med forsiktighet. Det er mulig at de involverte mekanismene i gjennomslag skaleres forskjellig enn kun med økende antall nåler eller areal og det krever mer forskning for å få full forståelse.

Preface

This thesis was performed in cooperation with ABB Corporate Research in Baden-Dättwil, Switzerland. I had the honor of spending 6 months there performing experiments. Working with Senior Principal Scientist Martin Seeger was a great honor. Through advice, discussions and guidance he taught me more than what is possible to reproduce in a single thesis. For which I am very grateful. I would also like to thank Daniel Over for all of his help with the experimental equipment and especially when some of it broke. I also wish to thank him for designing the needle electrode, a vital component in this thesis. I wish to extend my gratitude to Filip Halak who worked with this project during his internship at ABB in the fall 2017. Due to his work, I had a flying start with a good test procedure and system in place. I also wish to thank the rest of the P1 Gas Circuit Breaker team, who were helpful when I had questions and provided a great working environment with their friendliness.

I would like to thank Associate Professor Frank Mauseth and Professor Kaveh Niayesh at NTNU, for providing guidance and insights.

Gol, Norway, August 8th 2018.

Odd Christian Feet

Table of Contents

Chapter 1

Introduction

1.1 Problem Background

It is an aim in the electric transmission system to keep voltages as high as possible to minimize power losses. In air, the high voltage equipment require large distances between conducting materials to prevent failures. If the distance is too short the air can be ionized and conductive plasma channels, arcs, can form between the conductors. As the Transmission voltage increases, so does the physical footprint of the equipment. K. Natterer discovered in 1889 that substances like CCl_4 and $SiCl_4$ had higher electric strength than air [1; 2]. Further investigations led to the discovery of the insulation properties of sulfur hexaflouride (SF_6) and in 1938 the first patent involving SF_6 for usage in electric equipment was registered [3; 2]. The first usage of SF_6 in as arch quenching medium in circuit breakers occurred in the 1950s and in gas insulated systems (GIS) in the 1960s [4]. Using SF_6 at pressures higher than atmospheric air allows high voltage transmission to be used where open air equipment is not possible due to physical or aesthetic limitations. Since the 1960's, SF_6 has been the dominating insulation gas in high voltage equipment that is not insulated by air.

Technology advances pushes components in the power system to have higher ratings while minimizing the physical footprint of the component [5]. To keep reliability, while increasing ratings and reducing the size, it is necessary to have a good understanding of how the insulation medium behaves with varying parameters. Research has in recent years been able to understand the behavior and parameter dependence of SF_6 [6; 7]. The literature review shows in Chapter 2, that SF_6 is sensitive to surface roughness of the materials encapsulating the gas and particle contamination within the pressure vessel (e.g. GIS). This sets a limitation for how small the physical size of the equipment can be while keeping the insulation properties required for reliable operation. It has been thoroughly investigated, but is still not fully understood.

Even though SF_6 is an excellent insulation medium, it was classified as a climate gas with a global warming potential of 23,900 times that of CO_2 in a 100 year perspective [8]. Due to its global warming potential SF_6 was listed as one of six climate gases in the Kyoto protocol in 1997 [2]. Since then, research of climate friendly alternatives has increased with the goal of replacing SF_6 [9; 10; 2]. Due to all the criteria required of an insulation gas, some promising natural alternatives with no or low global warming potential, compared with SF_6, are Nitrogen (N_2), dry air (80 % N_2 and 20 % O_2) and CO_2. The latter has been used as the insulation medium in circuit breakers produced by ABB [11]. The literature review will show that the insulation properties of CO_2 is significantly lower than that of SF_6. It is not researched as an insulation gas as much as SF_6. More research is required to be able to increase the performance and reliability of equipment with CO_2 as a part or the main insulation gas.

Another parameter that has an impact on gas insulation is the so called *area law*, which is also known as the *enlargement law* [12]. This show that when increasing the insulated area the probability of a critical weak point and thus the probability of failure increases. The effect has been investigated in high voltage equipment, as presented in the literature review. However, the author has found no work where the enlargement law was used for predictions of the breakdown strength compared with experimental results. Understanding of how the underlying processes of a breakdown, e.g. first electron and leader propagation, scale according to the enlargement law is of interest for designing purposes. This is due to limitations for testing full scale equipment, like long gas insulated lines (GIL). A good understanding of how the different mechanisms scale might lead to better reliability without the need to test the full scale equipment.

1.2 Objective of Thesis

With what is presented in the problem background and the findings of the literature study, this thesis aim to:

- Investigate the impact of needle protrusions on the 50 % breakdown field strength and the 2 % breakdown field strength of lightning impulse voltages through the application of very fast rising step-like voltages. The setup to be tested are
    - Single needle, 20 needles and 100 needles protrusions with lengths in the range 0.05-2 mm in SF_6 at 4 bar and CO_2 at 6 bar.
- Investigate the enlargement effect on two different (rough) areas in SF_6 at 4 bar and CO_2 at 6 bar.
- Compare the results of the two above points with predictions from the enlargement law based on experimental results.
- Briefly investigate the difference and precision of the Normal distribution and the three parameter Weibull distribution.

1.3 Structure of the Report

This thesis will, after this introduction in Chapter 1, present a thorough literature review of the topics surface roughness in SF_6, CO_2 and the enlargement law in Chapter 2. Chapter 3 will present the required theory of surface roughness, electric fields, breakdown mechanisms in gas and statistics. The experimental method will be presented in Chapter 4. The results will be presented in Chapter 5 and discussion of the results will follow in Chapter 6. The thesis will finally be concluded in Chapter 7.

Chapter 2

Literature Study

Gas as insulation medium has been investigated since its potential for application was discovered. Different aspects of the insulation properties, dependencies, etc. has been discovered and investigated for insulation gases. Due to its superior insulation properties SF_6 as an insulation medium has been thoroughly investigated. There are very many publications and even specialist literature from Mosch and Hauschild [13] which investigate the different parameters and properties of SF_6. There is also literature which looks at the state of the art of gas insulated subsystems, e.g. Mazzanti et al [9], other have done reviews of the alternative insulation gases to SF_6, as done by Li et al [14] and Seeger et al [15].

This literature study will look into the more specific research of the impact of surface roughness in SF_6. CO_2 as an insulation medium as well as the impact of surface roughness in CO_2. The literature study will also look into the work investigating the enlargement law.

2.1 Surface Roughness and SF6

The following section will present the research that has been preformed in the area the impact of surface roughness in SF_6. The considered surface roughness was in the form of actual rough surfaces, particle contamination and fixed protrusions. In this field there was quite a number of publications, so only the most significant will be summarized.

One of the earlier investigations into the effect of surface roughness on breakdowns in SF_6 was performed by Nitta et al [16]. They investigated the area effect of four different electrode configurations with applied AC voltage. They observed a significant change in the breakdown voltage due to increasing area, conditioning effect and due to surface roughness [16]. To investigate the polarity effect of surface roughness, Nitta et al applied DC voltage of negative and positive polarity to a sphere-plane gap where only the sphere was roughened. Their results given in Figure 2.1 indicated that surface roughness was more significant when on the cathode than the anode [16].

Pedersen et al approximated surface roughness as an idealized smooth surface with a single hemispherical protrusion with a radius ρ shown in Figure 2.2a [17; 18]. This was used to calculate an approximation of the electric field enhancement of the actual rough surface. Pedersen et al approximated the ρ to be equal the height parameter R_{max}. They argued that the height parameter R_{max} was a better value to use instead of the more commonly variable R_a, the average height variation from the mean line. Using R_{max} as ρ in their calculations gave satisfactory results up to pressures of 6 bar when compared to previous work by Nitta et al [16]. This model for approximation has later been known as the *Pedersen model*.

In similar way as Pedersen et al, Berger used a hemispherical protrusion as an approxima-

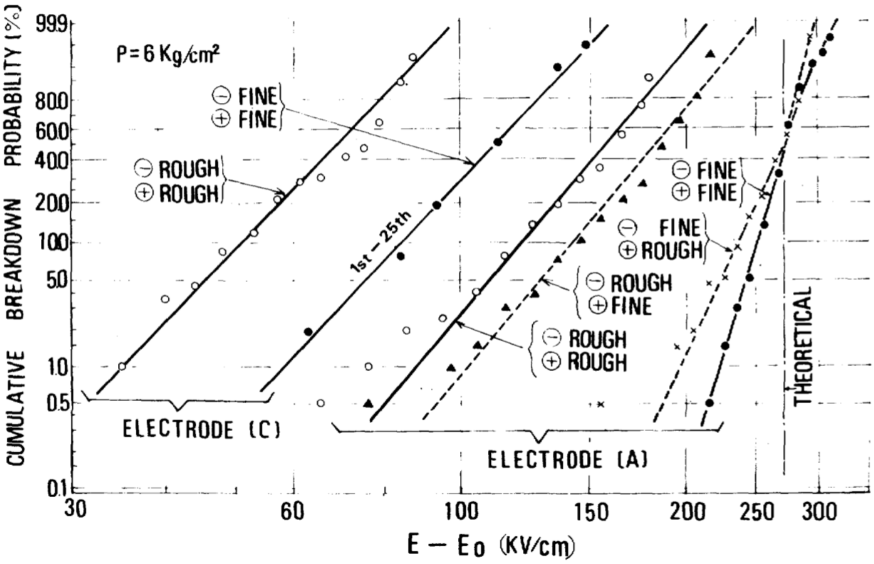

Figure 2.1: Effect of Electrode Roughness on Weibull probability Distribution [16].Electrode A is a 2 cm diameter sphere - plane stainless steel setup with a 0.1 cm spacing. Electrode C is 13.2 cm diameter - 15.2 cm diameter x 11.6 coaxial cylinder setup with a spacing of 1.0 cm of the materials stainless steel and aluminum [16].

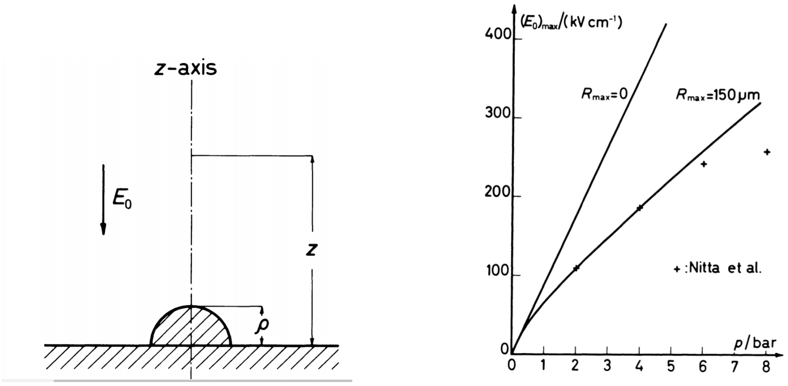

(a) Idealized model of a rough electrode surface as a smooth surface with a single hemispherical protrusion [17; 18].

(b) Maximum withstand field strength in SF_6 for R_{max} = 160 μm. The ideal curve for R_{max} = 0 is shown for comparison. Values marked with crosses refer to data for a large system, Nitta et al [17; 18].

Figure 2.2: Figures from Pedersen and Pedersen et al [17; 18]

tion of rough surfaces. However, he introduced a small cylinder shape with a hemispherical

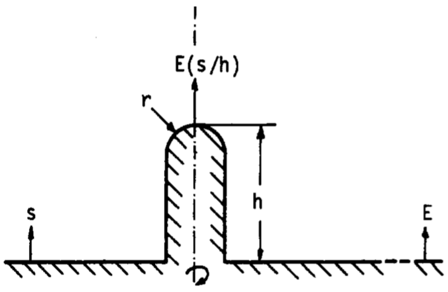

Figure 2.3: Cylindrical protrusion proposed by Berger [19]

tip from the smooth surface, see Figure 2.3. To define the protrusion Berger introduced a parameter h/r, where h was the protrusion height and r was the radius of the hemispherical tip. When $h/r = 1$ it was identical to the approximation of Pedersen model shown in Figure 2.2a. Berger's results from using this approximation showed a good agreement with the results from Pedersen et al when $h/r = 1$. The results Berger obtained was also in good agreement with what was found by Nitta et al [19; 16]. Berger provided electron scanning microscope pictures of an actual electrode after 100 sparks in air, which showed conditioning of the surface. Berger concluded that both the height and the shape of the protrusion(s) had an impact on the onset and breakdown voltage [19].

McAllister argued that using a single protrusion model exaggerateed the magnitude and extent of any probable field perturbation and was thus of limited validity [20]. Instead McAllister proposed a model consisting of protrusions of cylindrical symmetry. Figure 2.4a shows a single ridge and Figure 2.4b shows multiple ridges proposed as models by McAllister. McAllister performed calculations of both the single and multiple protrusion models, the results are presented in Figure 2.4c. The field calculations showed that the neighbouring ridges lead to a decrease of roughly 30 $\%$ in the overall field enhancement along the apex line. Where the field enhancement was found as the field strength at the tip of the protrusion divided by the average background field strength [20].

Crichton et al investigated how simple and idealized spherical protrusions of radius of 390 μm and 500 μm in a 20 mm gap influenced the pre-breakdown in SF_6 and SF_6/N_2 mixes [21]. Crichton et al tested with a 10 mm uniform gap with SF_6 and a 390 μm spherical protrusion. Their results showed that the static breakdown field (DC breakdown field) was higher when the protrusion was applied to the anode compared to when the protrusion was applied to the cathode. Increasing the number of protrusions, from one to seven, had a bigger reduction of the breakdown field for the anode protrusions than for the cathode protrusion. Increasing the number of protrusions reduced the scatter of the results For both polarities[21].

Bortnik et al investigated the impact of a single needle protrusion with tip curvature of 50 μm in a gap with Bruce profile electrodes of 80 mm in diameter. The needle was adjustable above the plane by a micro-metric screw which allowed the height of the needle to be varied in the range from 50 to 500 μm. The setup was tested in SF_6 in the pressure range of 0.1-0.7 MPa with negative polarity direct voltage. Their results were compared

(a) Single ridge.

(b) Multiple ridges.

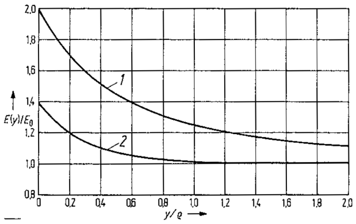

(c) Field distribution associated with the single (1) and the multiple ridges (2).

Figure 2.4: Figures from McAllister [20].

to estimated values from the streamer criteria for different protrusion shapes, presented in Figure 2.5 [22].

Oiu et al investigated how surface roughness of coaxial electrodes affected the breakdown strength of SF_6. They tested three separate electrodes with the roughness parameter R_z of 0.86, 15.7 and 48.6 μm. Their results showed a reduction of the breakdown voltage with increasing roughness. Oiu et al concluded with that for large surface areas the surface roughness effect was not a function of the product of gas pressure and roughness height as done in previous work. They also concluded that gas pressure had a stronger influence of the breakdown than surface roughness in SF_6 [23].

Li and Qui continued the work using a multi-ridge model to represent the surface roughness of machined electrodes [24]. They argued that only one of the three parameters was independent in the model proposed by McAllister. They proposed a new model, shown in Figure 2.6, with the parameters: r - the curvature of the ridge peak(s). s - the spacing between adjacent profile ridges. h - the height of the profile ridges. The new parameter Li and Qui included was a_l indicating the asymmetry of the ridges. Their calculations showed that an assumption of a_l being half the value of s was sufficient in engineering applications [24].

Through calculations of line charges, Li and Qui calculated the electric field enhancement, used streamer inception criterion and calculated the surface roughness factor $\zeta = (E_0/p)/(E/p)_{lim}$. Where E_0/p is the macroscopic background field and $(E/p)_{lim} =$ 88.8kV/mm · MPa [24]. ζ represents the reduction of the breakdown strength from the critical field due to surface roughness. This was then compared to an experimental setup where three rough surfaces were used. Two of the surfaces were machined and one had

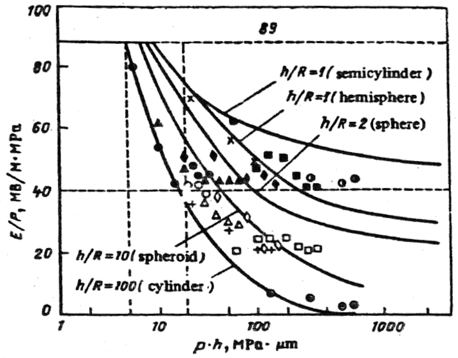

The onset and breakdown strengths referred to pressure and in relation to the product of the projection height with the pressure for an electrode system with a uniform macro-field:

breakdown — ● — h=54 μм, ▲ — h=94 μм, ◆ — h=220 μм, × — h=270 μм, ■ — h=530 μм, ◑ — h=1500 μм; corona discharge ignition — h/R=1,8—○, h/R=3—△, h/R=3,4—◇, h/R=3,5—+, h/R=8,8—□, h/R=100—⊙

Figure 2.5: Results from Bortnik et al [22]

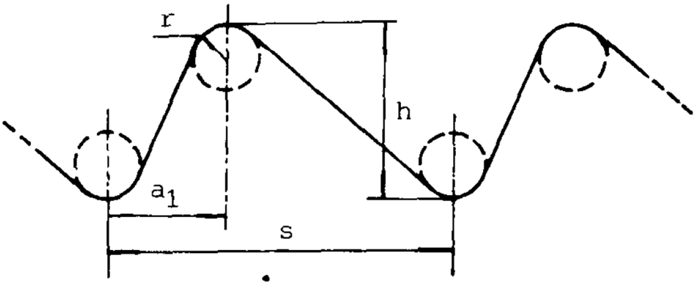

Figure 2.6: Multiple ridge model proposed by Li and Qui [24].

a copper wire placed in a spiral. Using measured values of these surfaces Li and Qui concluded from their results (not shown), that their model could be used to predict the surface roughness effect for machined electrodes (turntable). Li and Qui also concluded that the surface effect from an electrode with multiple protrusions was less severe than for a surface with a singular protrusion, predicted with Pedersen's model [24].

El-Makkawy simulated and calculated the onset and breakdown voltage with a single needle protrusion on an ideally smooth electrode in SF_6 [25]. The calculations took into account the space charge field distribution and showed that for increasing needle lengths, a reduction in the onset and breakdown voltage was expected. El-Makkawy's experimental results confirmed these expectations [25].

As a part of the investigation of the effect of electrode coatings, Lederle and Kindersberger investigated the effects of surface roughness on sphere-plane electrodes. Their setup had for different degrees of surface roughness (given in R_z) and stressed with positive and negative lightning impulse (LI). Their results are presented for positive and negative polarity of the spherical electrode in Figures 2.7a and 2.7b respectively.

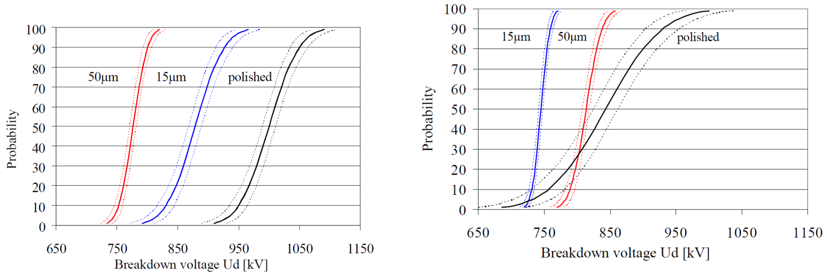

(a) Normal distribution with 95 % confidence region. Applied positive lightning voltage to sphere-plane electrodes, with 40 mm gap and 30 mm radius hemisphere. From [26]

(b) Normal distribution with 95 % confidence region. Applied negative lightning voltage to sphere-plane electrodes, with 40 mm gap and 30 mm radius hemisphere. From [26]

Figure 2.7: Figures from Lederle and Kindersberger [26].

Lederle and Kindersberger concluded that for positive LI-voltage the breakdown voltage decreased with increasing surface roughness. However, for negative LI-voltage, no definite correlation between breakdown voltage and surface roughness (for aluminum electrodes) could be found [26]. Lederle and Kindersberger investigated the effects of surface roughness and coatings for AC and DC voltages, and made similar conclusions as for LI-voltages [27].

Seeger et al investigated the partial discharges and breakdowns of small protrusions in SF_6 [28]. They used an electrode setup with uniform background field with a 1 mm needle protrusion on one of the electrodes. This electrode setup was tested in the pressure range of 0.1 MPa to 0.5 MPa for both positive and negative polarities high voltage step pulses with rise time of 100 ns, while being observed with both electronic and optical diagnostic equipment. Based on measurements of injected charges into leader channels, they derived a generalized model which explained the major features that was observed [28]. Their model used the reduced background field ($x = E_0/E_{cr,0}$) and the protrusion length L as the relevant parameters [28]. Their model described the main features of pre-breakdown corona activity, the main features of leader channel development, arrested leader decay and dependence of first electron for both polarities [28].

Seeger et al continued with this model and improved it to take into account the applied background field, gas pressure, protrusion length and voltage polarity [7]. The model could correctly predicted the (one dimensional) behavior of leader inception, propagation and breakdowns. This allowed it to predict the fields when breakdowns would occur in SF_6 [7].

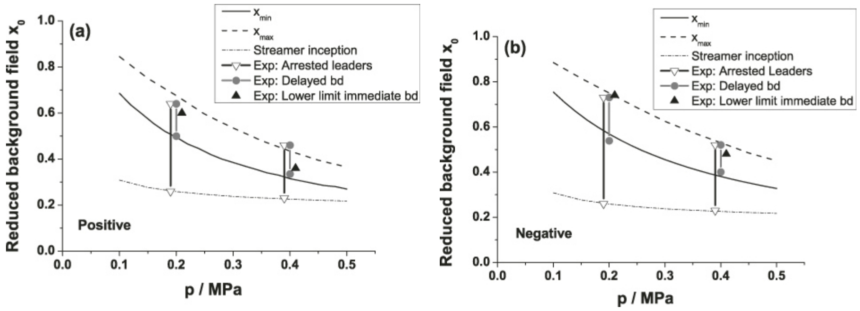

(a) Positive leader predictions and results. **(b)** Negative leader predictions and results.

Figure 2.8: Figures from Seeger et al. showing the ranges of different leader discharge types and predictions for both polarities. x_{min} and x_{max} given by the model from Seeger et al compared with observed discharge behavior from experiments [7].

Figure 2.8 shows the predictions made by the model compared with their experimental results by Seeger et al [7].

Bujotzek and Seeger investigated the parameter dependencies in SF_6. The dependencies investigated were first electron, streamer inception, streamer to leader transition, stepped leader propagation and to spark transition [6]. They investigated five electrode configurations: low surface roughness, technical equivalent surface roughness, high technical equivalent surface roughness, single protrusion and a single oblong particle. These were all simplified to a single idealized microprotrusion with height L and tip radius of curvature R. Giving L/R ratios of the surfaces (in same order) of 1, 2, 2, 4 and 10. Bujotzek and Seeger stated that for first electron generation at positive polarity, the electron had to be generated in the enhanced region of the gas volume in front of the electrode (protrusion). While at negative polarity the electron must be provided at the surface of the field enhanced electrode. Based on previously published models, they presented an extensive and systematic comparison of parameter dependencies from calculations and experimental work. Their results were summarized, Figure 2.9, showing the combined breakdown mechanism as functions of the reduced background fields and pressure for both AC and lightning impulse voltages. The leading breakdown mechanism at a given pressure was shaded with yellow.

Bujotzek and Seeger discussed that for the investigated pressure range, streamer inception

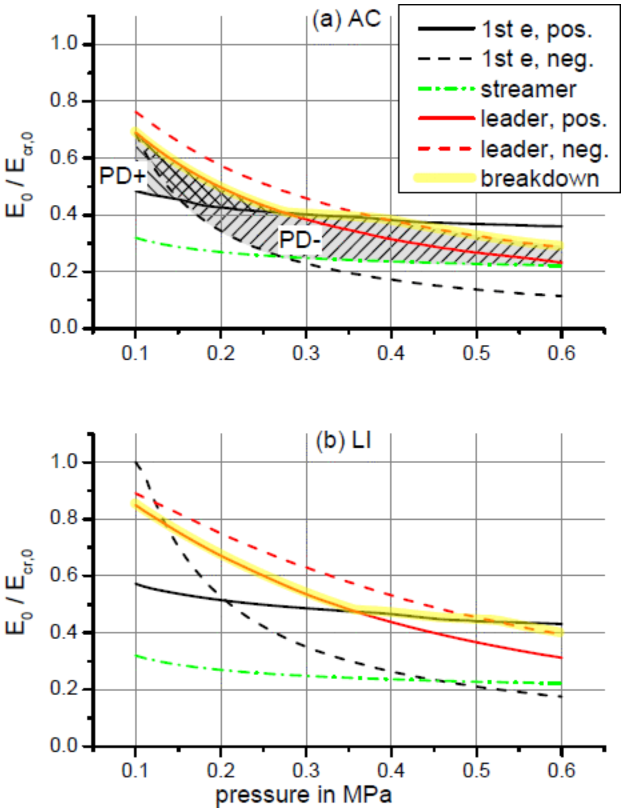

Figure 2.9: The pressure dependent reduced background field required for first electron, streamer and leader breakdown for a 1 mm protrusion with L/R = 4 for a) AC voltage and b) lightning impulse voltage [6].

was not decisive for breakdown. However, streamer inception determined the onset for partial discharges for particles and protrusions. They also discussed the importance of first electron at higher pressures, especially with positive polarity [6].

2.2 CO2

One of the earlier investigations into breakdowns in CO_2 was performed by Young [29] in 1950. He investigated the behaviour of breakdowns in CO_2 from low pressures to liquid state. Paschen's similarity law was verified for low pressures, but with a deviation at high pressures and short gap distances. Young determined the Townsend's first coefficient in CO_2 and field emission constants through measurements of pre-breakdown currents [29].

Brand and Kopainsky investigated the breakdown field strength of unitary attaching gases and mixes of attaching and non-attaching gases. One of the attaching gases they investigated was CO_2. Brand and Kopainsky created a breakdown model which could quite well predict the critical field strength of gases and gas mixtures, within admissible error [30]. The value used by Brand and Kopainsky as the experimental critical field was 15 kV in a plate - plate geometry at the pressure of $p = 0.66$ atm and $pd = 4.6$ atm·mm [30], which translates into a pressure reduced critical field of $E = 21.5$ kV/cm·bar.

Shiiki et al investigated the dielectric performance of CO_2 in comparison with N_2. To see which one was a better alternative for replacing SF_6 to reduce global warming potential [31]. They tested both gases with standard lightning impulse voltage in a co-axial cylindrical setup with inner and outer radii of 6 and 15 cm, respectively, at a pressure of 1.1 MPa. Their results, presented in Figure 2.10, showed that there was a polarity difference between the two gases, which required further investigation [31]. Their results showed that negative polarity of CO_2 preformed 35 $\%$ better than positive polarity of N_2, which were the polarity with lowest breakdown voltage for each gas respectively. Indicating that CO_2 had a better potential for replacing SF_6 as an insulation medium [31].

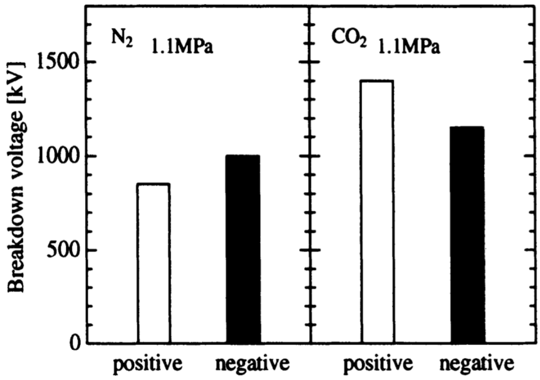

Figure 2.10: Comparison of breakdown voltages in CO_2 and N_2 [31]

The breakdown voltages of Shiiki et al's results in CO_2 at 1.1 MPa pressure reached 70 $\%$ of that of SF_6 at 0.5 MPa [31].

Uchii et al presented an investigation into the arc-quenching behavior of CO_2 when used as the insulation medium in a gas circuit breaker with the ratings of 72.5 kV and 31.5 kA. The circuit breaker was designed based on fundamental research and had a gas pressure of 0.8 MPa [32]. Uchii et al found that the circuit breaker behaved satisfactory to all their operational tests. Their life cycle analysis of the CO_2 circuit breaker showed that it would have a global warming impact which was reduced by 45 $\%$, when compared to the latest SF_6 breakers [32].

Juhre and Kynast investigated how CO_2, N_2 and a 80 $\%$ N_2/20 $\%$ CO_2 mixture performed in GIS applications in comparison with SF_6 [33]. They used a GIS system where they could test the gases from 0.6 MPa to 1.8 MPa with coaxial cylindrical electrode setup. Figure 2.11 show their results for the withstand electric field strengths, showing that CO_2 and the mixture performed better than pure N_2. However, neither could perform as well as SF_6 at 0.4 MPa, a typical pressure in a GIS system with SF_6 [33].

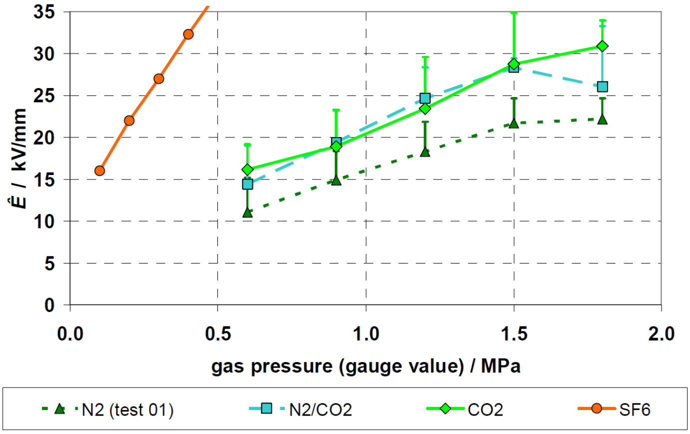

Figure 2.11: Comparison of LI impulse withstand electric field strengths [33]

Meijer et al performed a comparison of the breakdown strength of the gases CO_2, N_2 and SF_6. Their experiments were with two smooth Rogowski shaped electrodes with gas pressures of 7, 9 and 11 bar absolute [34]. They tested the setup for AC, lightning impulse and switching impulse voltages. Their average breakdown values are presented in Table 2.1.

Table 2.1: Pressure reduced breakdown values for the different gases [34].

Gas	Intrinsic Breakdown [kV/mm·bar]	Experimental Breakdown [kV/mm·bar]
N_2	3.29	2.0 ± 0.3
CO_2	3.01	2.2 ± 0.1
SF_6	8.90	7.9 ± 0.5

They recommend CO_2 as the better insulation gas due to less scatter, even though the results for N_2 and CO_2 were similar. They also concluded that the pressure reduced electric field strength was nearly constant, which indicated a nearly linear increase in the breakdown strength with increased pressure in that pressure range [34].

Okabe et al investigated the fundamentals of breakdowns in CO_2 with actual application conditions [35]. They tested CO_2 in a coaxial setup where they investigated pressure dependence, area effect, surface roughness and particle contamination. Their results showed that negative lightning impulse voltage had lower breakdown electric fields compared with positive polarity. When pressure dependence was tested, the breakdown voltage increased linearly for negative polarity. While positive polarity tended to saturate when the pressure reached values of 2.0 MPa [35]. Their investigations into surface roughness showed that smoothing the surface finish to a roughness of 5μm from 25μm (unclear which parameter they were talking about, R_a, R_z etc.) increased drastically the AC inception electric field for partial discharges. Figure 2.12 show the results obtained by Okabe et al in CO_2 compared with SF_6 when they tested with a foreign particle inside the vessel with a diameter

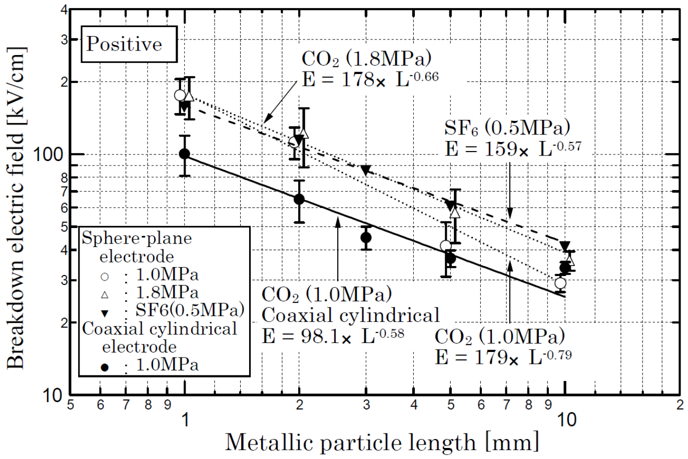

Figure 2.12: Comparison by Okabe et al of metallic particle length versus the breakdown electric field strength in CO_2 at 1.0 and 1.8 MPa and SF_6 at 0.5 MPa for sphere-plane and coaxial cylindrical setup [35].

of 0.25 mm and lengths from 1 to 10 mm. The results showed that the breakdown electric field in CO_2 declined in much the same way as the breakdown electric field did in SF_6 [35].

The effect of electrode surface roughness on CO_2 and N_2 was investigated by Hikita et al [36]. Their setup was a quasi uniform sphere-plate electrode where the sphere electrode was sandblasted to four different degrees of surface finish [36]. The electrode setup was stressed with both AC and lightning impulse voltage with gap distance of 10 and 20 mm at 0.6 MPa pressure. Figure 2.13a show the results obtained by Hikita et al with AC voltage applied to a 10 mm gap in CO_2, where all breakdowns occurred at negative polarity. The results showed no significant change of the breakdown voltage with increasing surface roughness (given as R_z). The symbols used by Hikita et al give the average result, while the error bars give the measured maximum and minimum values.

Figure 2.13b show the results by Hikita et al with applied lightning impulse voltages. For all tested surfaces, positive breakdown voltage was higher than for negative polarity. The results for negative polarity decreased for increasing surface roughness. While positive polarity decreased for all but the roughest surface where the breakdown voltage increased from the second roughest surface. From their results, Hikita et al determined the impulse ratio for positive and negative polarity at 0.6 MPa pressure in CO_2 given in Table 2.2 [36].

Table 2.2: Impulse ratio for CO_2 at 0.6 MPa. BDE = Breakdown electric field [36].

Pos. imp / ac BDE	Neg. imp / ac BDE
1.42	1.24

Ka et al investigated the characteristics of breakdowns in CO_2 when applied lightning impulse and AC voltages. Their setup was a quasi-uniform (a type of coaxial cylindrical

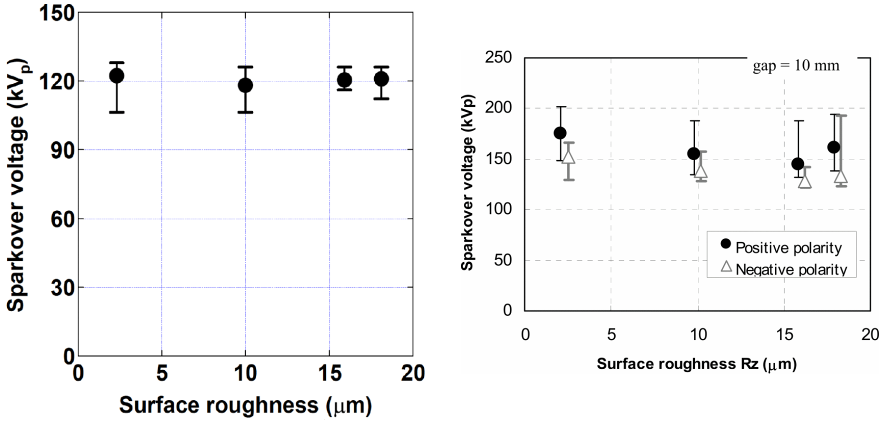

(a) Sparkover voltage in CO_2 when applied lightning AV voltage.

(b) Sparkover voltage in CO_2 when applied lightning impulse voltage.

Figure 2.13: Results from Hikita et al [36].

electrodes) electric field setup at 0.55 MPa pressure. They looked at the area effect, polarity effect and the impulse ratio between lightning impulse and AC breakdown voltages [37]. The setup used by Ka et al, allowed for the number of identical electrodes to be increased, their tests consisted of 1, 4 and 12 identical electrodes, allowing them to test the area effect. Figure 2.14 show Weibull plots of their results for positive and negative lightning impulse. Their results showed that positive lightning impulse breakdown voltages were higher than negative polarity. Their results also showed a decrease in the breakdown voltage with increasing number of electrodes for both polarities. Another discovery made by Ka et al was that positive polarity had bigger dispersion of the results than for negative polarity, especially with a large effective area [37].

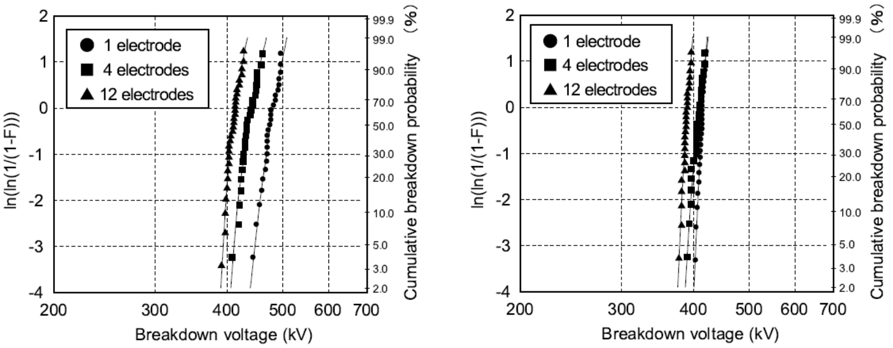

(a) Positive polarity

(b) Negative polarity

Figure 2.14: Results from Ka et al with multiple electrode setup showing Weibull plots of lightning impulse breakdown voltage in CO_2 at 0.55 MPa [37].

Yoshida et al investigated the motion of free particles in gas insulated systems with AC voltages. They measured the voltage-time sparkover characteristics and lift-off electric field strengths for the gases N_2, CO_2 and dry air (80 % N_2 and 20 % O_2). The tests were at 0.55 MPa pressure in an actual coaxial cylindrical GIS bus [38]. The particles placed inside the vessel were aluminum wire pieces with lengths of 3 mm and radius 0.2 mm. They found a ratio between the particle breakdown voltage and the clean breakdown voltage of 0.55 ($V_{particle}/V_{clean}$), indicating a quite significant reduction of the insulation properties for CO_2 due to particles [38]. Yoshida et al continued in a similar setup with investigations with fixed particles on spacers and on the conductors. Their results showed that partial discharges were more likely to be influenced by the type of gas when attached to the conductor than when attached to the spacers. Their results also showed that the partial discharge inception voltages were much lower than the breakdown voltages in the natural gases, CO_2, N_2 and dry air when compared SF_6. The comparison of the results with a particle attached to the spacer in the different gases is shown in Figure 2.15 [39].

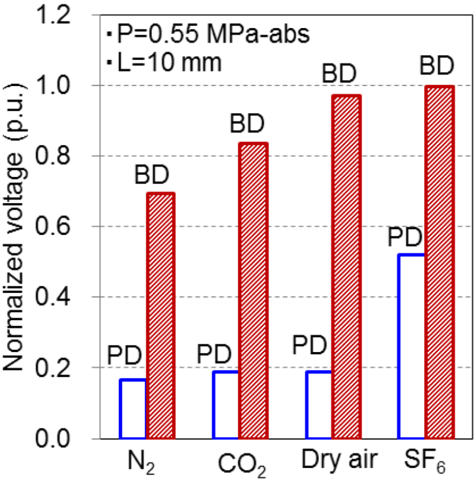

Figure 2.15: Results from Yoshida et al showing partial discharge inveption voltage (PD) and the 50 % breakdown voltage (BD) normalized to the breakdown voltage in SF_6 initiated by 10 mm metallic particles attached on spacer surfaces in different gases at 0.55 MPa pressure.[39]

Seeger et al investigated streamer parameters and breakdowns in CO_2 with two different setups to get a better understanding of the insulation properties of CO_2 [40]. One setup was a plate-plate uniform field with needle protrusions at the lengths of 1.5, 2.5 and 4.5 mm. The other setup was a non-uniform point-to-plane geometry. The experiments were performed in a gas insulated pressure vessel in the pressure range 0.05 - 0.5 MPa. They investigated statistical time lag, streamer inception, breakdown fields and streamer propagation lengths, velocity and radius. Using a photomultiplier Seeger et al were able to investigate the behavior of streamers between inception and breakdown, so-called arrested streamers. They discovered that there was a pronounced polarity difference where the negative streamer stability field, or streamer crossing field, was at a value of roughly half the critical field of 10-12 V/(m·Pa). While at positive polarity, the streamer stability field coincided with the critical field in the around 21.5 V/(m·Pa) at pressures above 2 bar. This was shown in their results, see Figure 2.16. Seeger et al found within the uncertainties no dependence on needle or gap length as shown by their results in Figure 2.17 [40].

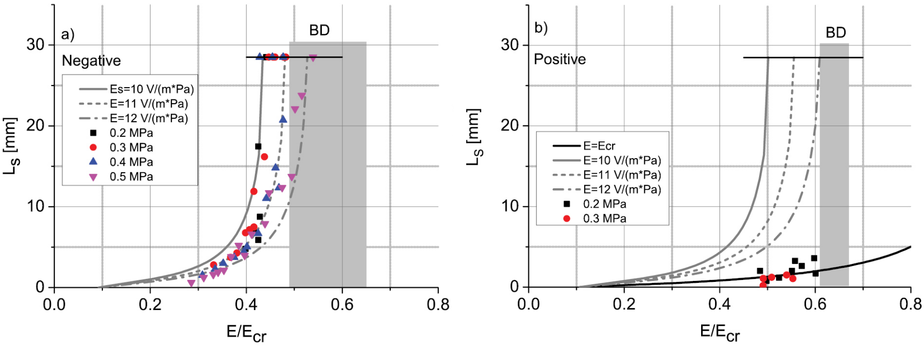

Figure 2.16: Streamer length vs the reduced background field E/E$_{cr}$ at (a) negative and (b) positive polarity of a 1.5 mm needle in a 30 mm gap. The critical field used by Seeger et al was 21.5 V/(m·Pa)[40].

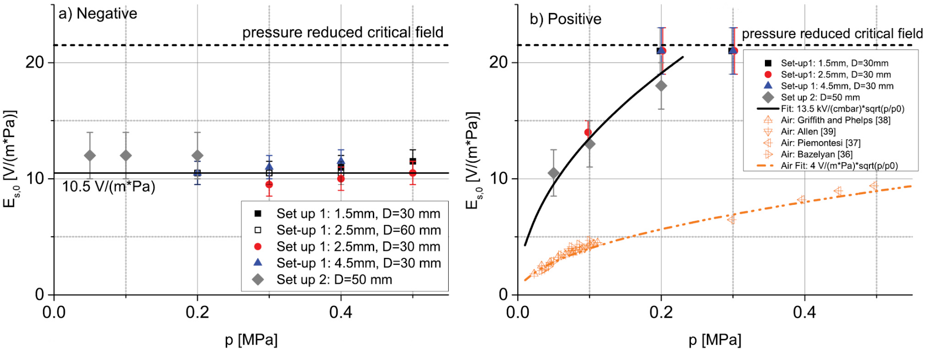

Figure 2.17: Average pressure reduced streamer stability fields in the uniform with protrusion (set-up 1) and the non uniform point-to-plane (set-up 2) versus pressure for negative (a) and positive (b) polarity. For negative polarity the pressure-reduced field strength line at 10.5 V/(m·Pa) is shown as an eye guide. In b) the the dash-dotted line show the result for dry air [40].

For their investigation of the breakdown fields in the point-to-plane field, Seeger et al found at all pressures with negative polarity that the breakdowns agreed well with the pressure reduced streamer stability field of 11 ± 2 V(m·Pa). Their explanation was that, after sufficient voltage application time streamer crossing was followed by streamer to spark transition which resulted in a breakdown. For positive polarity, they found that streamers could lead to breakdowns at low pressures of 0.1 MPa and below. At pressures above 0.1 MPa they discovered breakdowns at fields lower than the positive streamer stability field, indicating that streamers could not be decisive at these pressures. Instead leader inception and leader propagation was decisive for breakdowns at pressures above 0.1 MPa with positive polarity in CO_2. This was shown with Figure 2.18, showing the result from the point-to-plane set-up (set-up 2) [40].

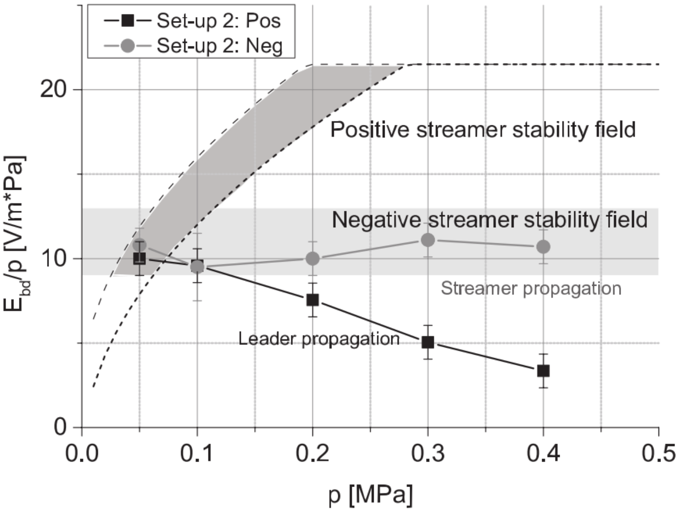

Figure 2.18: Reults from Seeger et al showing the average pressure-reduced breakdown fields for the point-to-plane setup (setup 2) with the measured ranges for pressure reduced streamer stability fields for both positive and negative polarity as shaded areas[40].

Seeger et al performed an investigation into the breakdown fields in synthetic air, CO_2, CO_2/O_2 and CF_4 in the pressure range 0.5 to 10.0 MPa [10]. They tested in a high pressure vessel with concentric cylindrical electrodes with a 5 mm gap which was applied a switching impulse voltage.

Their results for CO_2, Figure 2.19, were lower than what was found by Cohen in similar tests. Their results seemed to saturate when reaching higher pressures. To achieve a realistic field simulation of the microstructure, the approximation of a conical shape with a cylindrical protrusion on top, Figure 2.20, was used in the electric field simulations for the streamer inception calculations. Their results from streamer inception calculations found that they reached a saturation around 250 kV/cm when the height of the cylindrical protrusion was 10 μm with a length over radius ratio of l/r = 100 [10].

Seeger et al discussed that their results were influenced by the surface roughness, which caused a scatter in the results. They also measured surface roughness and performed three-dimensional surface scans, which showed that the breakdowns created craters surrounded by circular ridges. The ridges were not necessarily symmetrical or surrounding the entire crater. They discussed further that the natural surface roughness structures, the artificial roughness structures created by breakdowns and dust *competed* to initiate breakdowns in their setup [10]. They concluded that for technical setups that for CO_2 and the other tested gases reached a *saturation* at pressures above roughly 2 MPa with technical surfaces. They explained this with the critical length of the streamer inception calculations at these pressures became shorter than 10 μm, which was shorter than the length of surface structures and dust [10].

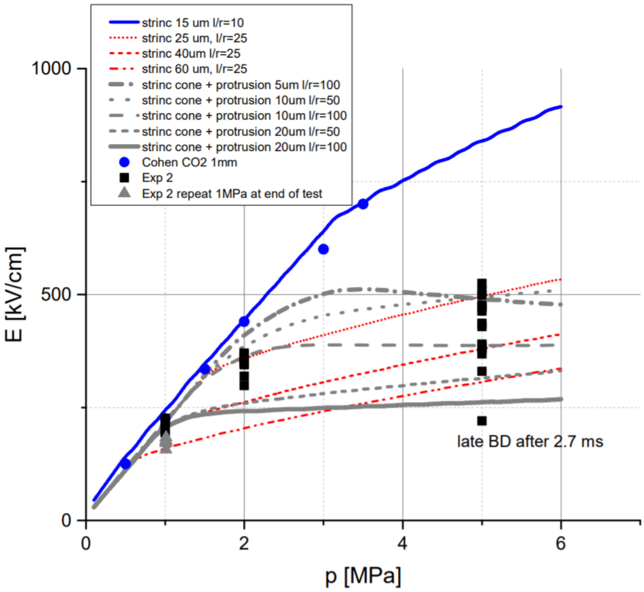

Figure 2.19: Breakdown field strength values from experiments at different pressures as black points plotted along with streamer inception calculations obtained by Seeger et al. Additional results from Cohen [41] were added as blue points for comparison [10].

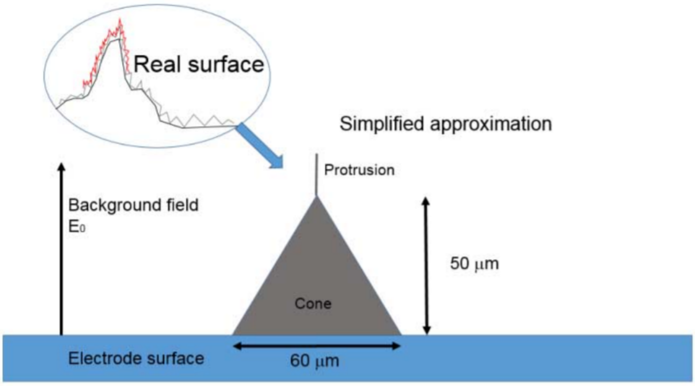

Figure 2.20: Surface structure simplification used by Seeger et al for electric field strength simulations and streamer inception calculations [10].

2.3 Enlargement Law

As previously mentioned, authors like Nitta et al performed a thorough investigation into the area effect [16]. Crichton et al looked at multiple particles in SF_6 [21] and Ka et al used multiple electrodes to increase the effective area [37]. All investigated the enlargement law (area law/effect). Other authors have performed investigations as well into the enlargement law and some of their work will be presented in the following.

The results obtained from Nitta et al's investigation into the area effect in SF_6 showed a similar reduction for both the smooth and the rough electrodes as the area was increased. Shown for the minimum breakdown voltage, defined as the 0.5 % probability of breakdown, in Figure 2.21. Their results showed a difference between 0.5 % breakdown strength with the rough and fine finish surfaces. Their results converged asymptotically towards the zero breakdown field with increasing area, regardless of the surface finish [16].

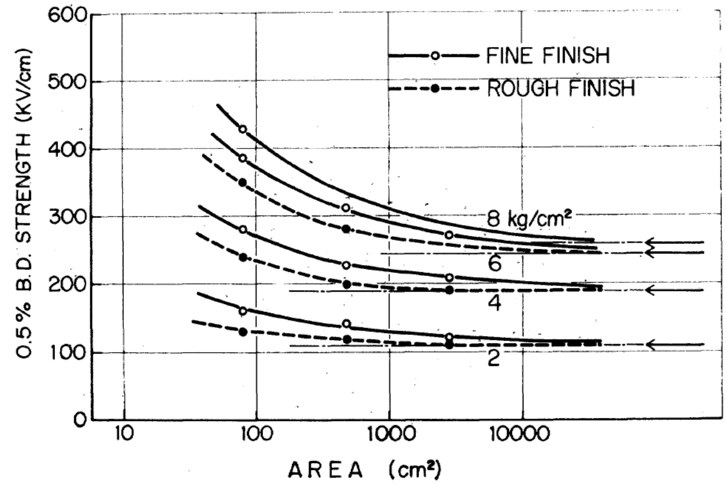

Figure 2.21: Results from Nitta et al showing the minimum breakdown strength as a function of surface area [16].

Dunz et al investigated the theoretical statistical properties of breakdowns with surfaces with multiple protrusions in SF_6 [42]. They modeled the surface protrusions as rods with hemispherical caps, as Berger, and argued that by determining the probability of breakdown for a singular rod, one could use the area law to predict the influence from multiple identical needles. Figure 2.22 show the surface model used by Dunz et al, including the parameters they used to describe the protrusions [42]. Dunz et al used the protrusion parameter, defined as the height, *h*, divided by the radius of the tip, *r*, (*h/r*). Another parameter they used was the shielding parameter, given as *a/2r*, where *a* was the distance form center to center of each protrusion. The parameter *x* in Figure 2.22 represent the direction of the *x* co-ordinate in the setup.

Dunz et al used a method to calculate the field enhancement of the protrusion vertex where the enhancement were only depended on the protrusion parameter (h/r) and the shielding parameter (a/2r). Their electric field strength calculations were used to compare with first electron production, streamer and leader inception criteria to determine when breakdown would occur. Different values of the shielding parameter was used to calculate the breakdown criteria for 100 μm protrusions and a h/r of 10 at different pressures as shown in

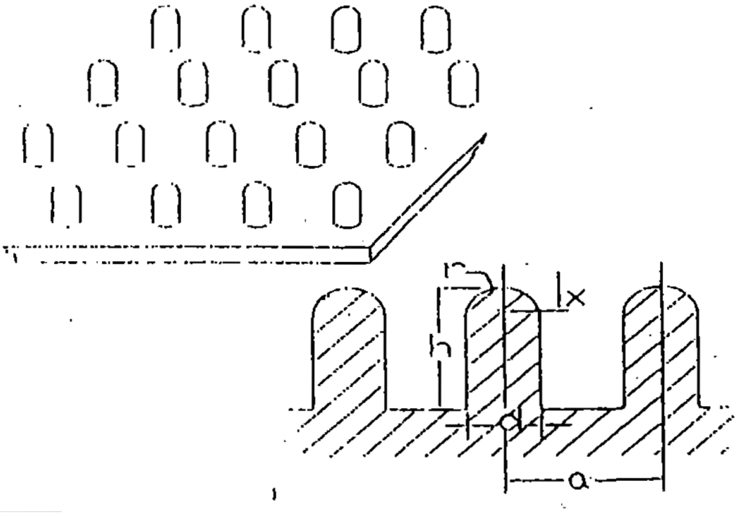

Figure 2.22: Multiple surface protrusion model used by Dunz et al [42].

Figure 2.23.

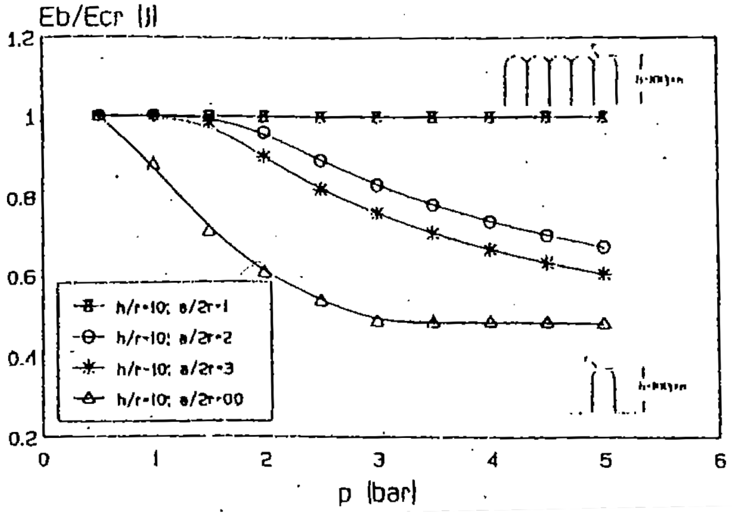

Figure 2.23: Computed breakdown field E_b given in relation to the critical field E_{cr} = 89 kV/(cm·bar) [42].

When the shielding parameter was a/2r = 1, their calculations showed that it was efficiently a reduction of the effective protrusion height. When the protrusion shape was reduced from *h/r* = 10 to *h/r* = 1, the shielding effect was reduced. They used their electric field calculations to estimate the breakdown probability according to the modified volume time law given in Equation 2.1. In Equation 2.1 dn_e/dt is the volume production rate of electrons from negative ion detachment, η and α are the attachment and detachment[1] coefficient of the gas and V_{Cr} is the critical volume dependent on the time t according to the applied voltage shape. The calculated probabilities were then applied the area law to estimate the probability for *N* statistically independent protrusions.

$$p = 1 - \exp\left\{ \int_t \int_{V_{Cr}(t)} \frac{dn_e}{dt}\left(1 - \frac{\eta}{\alpha}\right) dV dt \right\} \tag{2.1}$$

Figure 2.24 show Dunz et al's results for the breakdown probability for *h/r* = 1 and *h/r* = 10, where the latter was more pointy than the former. Their calculations showed a minor change in the breakdown probability.

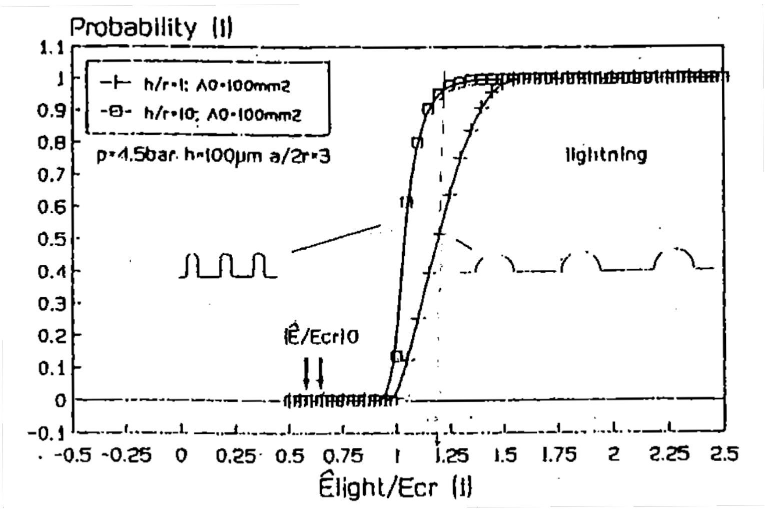

Figure 2.24: Computed breakdown probability for two different shapes of protrusions h/r = 1 and h/r = 10. With lighting impulse voltage, h = 100 μm protrusion with shielding parameter a/2r = 3 for SF_6 at 4.5 Bar pressure [42].

Their results given in Figure 2.25 showed that the effect of varying the shielding parameter resulted in very small changes to the breakdown probability.

Dunz et al found from their calculations that a significant change of the breakdown probability was seen when changing the protrusion height from 10 to 100 μm, see the shift to the left in Figure 2.26.

Dunz et al concluded from their results that reasonable predictions could be made without very detailed knowledge of the surface structure, but did not compare this to experimental work [42].

Hama and Okabe [43] summarized the work by Honda et al [44], Nitta et al [16], Menju et al [45], Juhre and Kynast [33] and Hama et al [46]. They discussed the area effect

---

[1] They write that α, possible that they mean ionization coefficient.

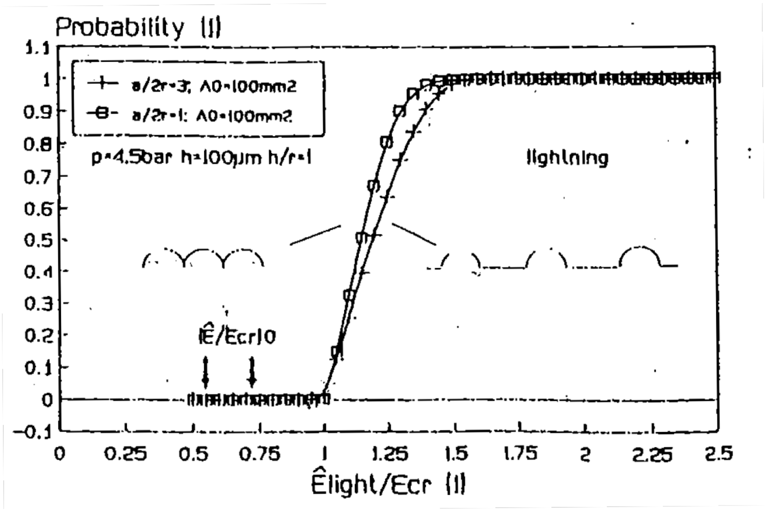

Figure 2.25: Computed breakdown probability for two different shielding parameters a/2r = 1 and a/2r = 3. With lighting impulse voltage, h = 100 μm, h/r = 1 μm and shielding parameter a/2r = 3 for SF_6 at 4.5 Bar pressure [42].

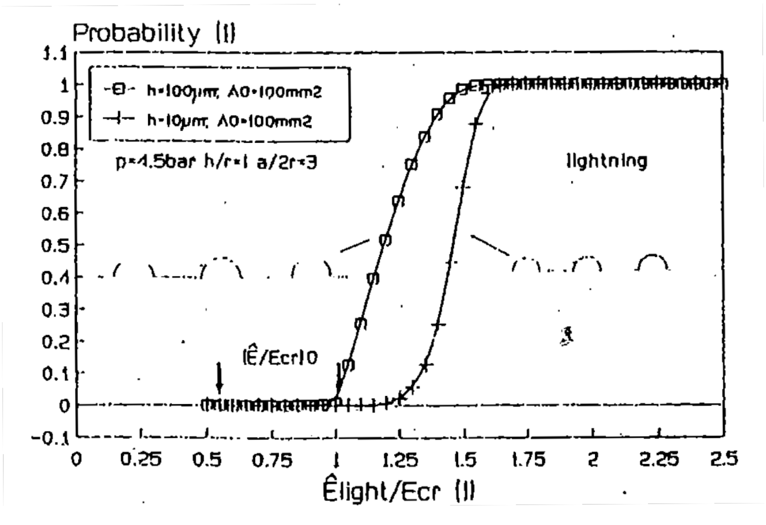

Figure 2.26: Computed breakdown probability for two different protrusion depths h = 10 μm and h = 100 μm. With lighting impulse voltage, h/r = 1 μm and a/2r = 3 for SF_6 at 4.5 Bar pressure [42].

in their publication about the factors dominating the dielectric performance of real size gas insulated subsystems with SF_6 and potential replacement gases. The summary of results was shown as the breakdown field strength over the theoretical electric breakdown strength, see Figure 2.27, where the effective area $S_{90\,\%}$ was the area where the electric field strength was above 90 % of the maximum electric field strength of the electrode for the different authors.

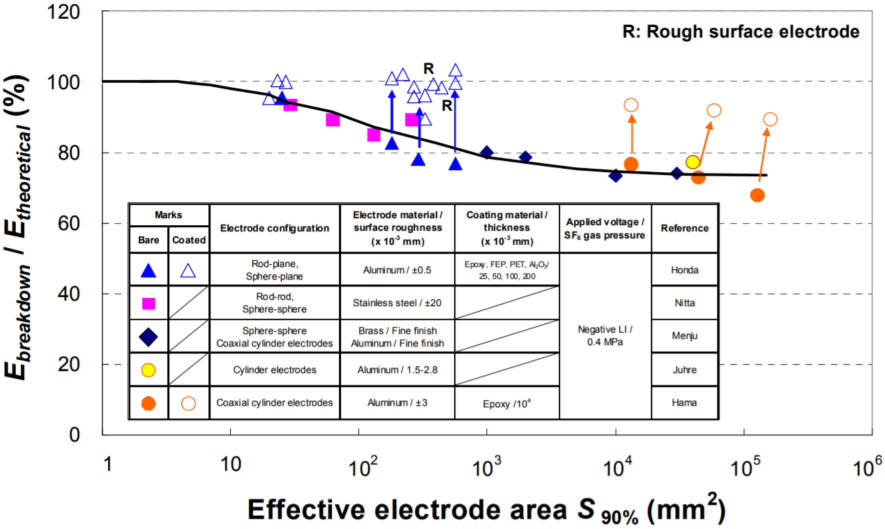

Marks		Electrode configuration	Electrode material / surface roughness (x 10^{-3} mm)	Coating material / thickness (x 10^{-3} mm)	Applied voltage / SF_6 gas pressure	Reference
Bare	Coated					
▲	△	Rod-plane, Sphere-plane	Aluminum / ±0.5	Epoxy, FEP, PET, Al_2O_3/ 25, 50, 100, 200	Negative LI / 0.4 MPa	Honda
■		Rod-rod, Sphere-sphere	Stainless steel / ±20			Nitta
◆		Sphere-sphere Coaxial cylinder electrodes	Brass / Fine finish Aluminum / Fine finish			Menju
●		Cylinder electrodes	Aluminum / 1.5-2.8			Juhre
●	○	Coaxial cylinder electrodes	Aluminum / ±3	Epoxy /10^4		Hama

Figure 2.27: Negative lightning impulse voltage at 0.4 MPa pressure in SF_6 [43].

The results showed that increasing the area of the electrodes, the breakdown voltage dropped down to a somewhat constant level at an effective surface of 10^5 mm^2, which was smaller than the area of an actual gas insulated system. The results showed in Figure 2.27 also include results for dielectric coatings, indicated with open symbols. The results showed that coatings had a potential of reducing the impact of the area effect by increasing the breakdown electric field strength [43].

2.4 Concluding the Literature Review

The following sections will bring up the main observations from each topic and mention observations for further investigation.

2.4.1 SF_6 and Surface Roughness

A lot of research has been performed in SF_6, more than what is possible to reproduce in a literature study. However, the previous work investigated showed that SF_6 was quite sensitive to surface roughness, protrusions and particles.

There have been several models for approximation of surface roughness, from Pedersen's and Berger's single protrusion models to the multiple ridges from McAlister and Li and Qui. In the more recent studies, e.g. Bujotzek and Seeger, the model used by Berger which was used and the length/radius ratio [6]. No work indicate that one is more *correct* than the other.

Previous work show that for actual surface roughness, negative polarity has a lower breakdown field strength than positive polarity and was the critical polarity due to a lack of first electrons for positive polarity [6].

For protrusions and particles, previous work showed that the leader mechanism were the decisive breakdown mechanism in SF_6. Indicating that the breakdown fields of positive polarity would be lower than negative polarity. However, for positive polarity the first electron dependence could also be a decisive mechanism, see Figure 2.9.

2.4.2 CO_2

The previous work studied in this literature review have found CO_2 to be a potential replacement with a lower greenhouse effect than SF_6. It does, however, not perform at the levels of SF_6 at 0.4 MPa pressure at 1.8 MPa pressure.

Breakdown with lightning impulse voltages were lower for negative polarity than for positive polarity in CO_2. CO_2 also showed similar behaviour and reduction in the breakdown fields due to particles as in SF_6.

There was a polarity difference for streamer crossing stability field in CO_2, where negative streamer crossing fields were found to be lower than positive polarity. At negative polarity, it is believed to be streamer to spark transition to be the dominating breakdown mechanism for breakdowns. For positive polarity above 0.1 MPa, breakdowns could be explained by the leader mechanism.Due to breakdowns occurring at electric field strengths lower than the positive streamer crossing stability field. For both polarities streamer inception was the determining criterion for the onset of partial discharges [40].

2.4.3 Enlargement Law

Previous work showed that increasing surface area decreased the breakdown strength for both polarities. The effect seemed to saturate after a certain area regardless of the surface finish.

In the work by Dunz et al, it was seen that the spacing of rough protrusions had a small impact compared to the height of the protrusions and that the shape (*h/r*) had some impact on the breakdown probability. Where a larger *h/r* ratio had lower breakdown fields.

2.4.4 Observation for Future Investigation

- Not much work has been performed with protrusions shorter than 2 mm. The only work found with protrusions shorter than 0.5 mm was that of Bortnik et al.
- The breakdown mechanisms involved with small protrusions shorter are not fully understood yet.
- The enlargement effect has been previously investigated, but no work has been found by the author where predictions have been made with the enlargement law based on experimental results.
- No work has been found to investigate how well the involved processes in breakdowns scale with the enlargement law, or if they scale at all.
- Some work has been done with multiple particles, but no work has been found by the author with multiple protrusion in an array setup similar to the theoretical work done by Dunz et al.

Chapter 3

Theory

3.1 Surface Roughness

No surface is ideally smooth, every surface has some sort of structure of *valleys* and *peaks*. The surface structure are created by the tools when removing material, material behavior etc. [47]. There are several methods of measuring and presenting the surface roughness. One common way is to present it as a surface profile, which presents it as a surface in two dimensional profile scan. This is done by tracing the height value along a horizontal direction. To better illustrate the variation of the surface it is quite common to apply a different scale to the horizontal and the vertical axes, making the surface look sharper than it is in reality. An example of a surface profile and this distortion is illustrated in Figure 3.1 [47].

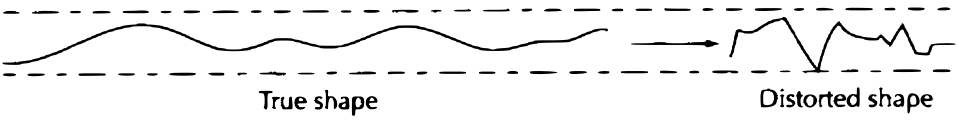

Figure 3.1: Comparison of real surface shape and distortion due to different scaling of height and width. Taken from [47]

This distortion is also common when producing surface scans and producing three dimensional images of surfaces. The parameters in this theory section will be described for two-dimensional surface profiles for simplicity, but the principles are the same for three-dimensional surface scans.

3.1.1 Surface Parameters

The most common and universally recognized surface parameter is the arithmetic average deviation of the mean line, R_a. From a profile scan, the mean line is determined as the average of all the surface values and is usually set as the zero value of the surface, see Figure 3.2 (i). Then the absolute value would be found of all the surface values, equivalent of mirroring the valleys above the mean line as shown in Figure 3.2 (ii). The arithmetic average deviation of the surface mean line, R_a, is then found from calculating the average of the values. The mean line and R_a is indicated in Figure 3.2 (iii). Mathematically, this is represented with Equation 3.1, where L is the sampling length, and $z(x)$ is the height value at the point x along the sampling length L [47].

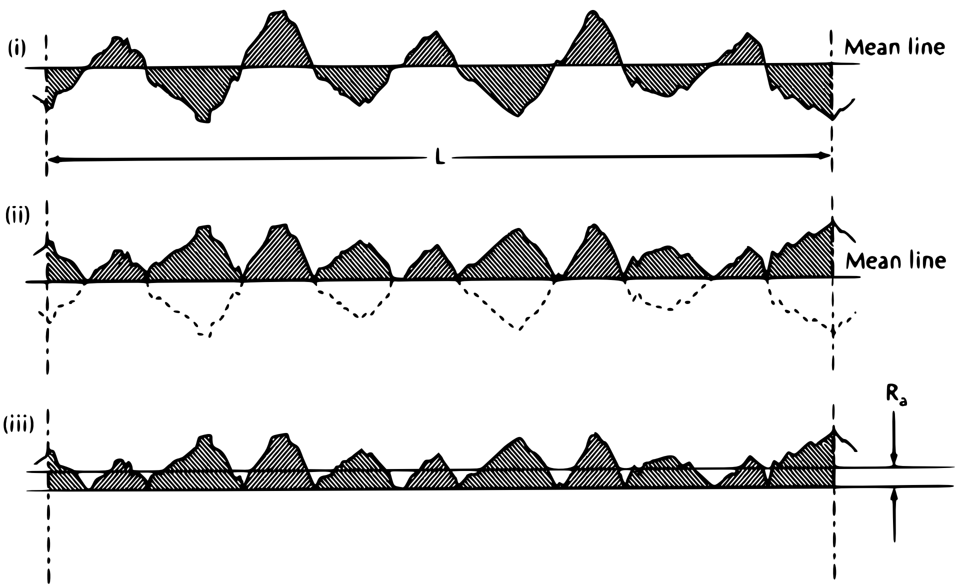

Figure 3.2: Illustration of how to determine the arithmetic average deviation of the mean line from a surface profile scan. Taken from [47].

$$R_a = \frac{1}{L}\int_0^L |z(x)| \tag{3.1}$$

Another parameter used to describe the shape of a surface is the ISO ten point height parameter, $R_{z,\,ISO}$, from ISO 4287/1-1984 [47]. $R_{z,\,ISO}$ is determined from distance between the average of the five highest peaks and average of the five deepest valleys. This is illustrated in Figure 3.3 and $R_{z,\,ISO}$ is found mathematically from Equation 3.2 [47].

$$R_{z,\,ISO} = \frac{(Z_{p1}+Z_{p2}+Z_{p3}+Z_{p4}+Z_{p5})-(Z_{v1}+Z_{v2}+Z_{v3}+Z_{v4}+Z_{v5})}{5} \tag{3.2}$$

The parameters R_p and R_v represent the highest peak and the deepest valley on a surface [47], respectively. Additionally to the parameters mentioned in this section there are several others used to describe surfaces that will not be described here.

3.2 Electric Field

When working in the field of high voltage engineering, it is a simple principle that the engineer aims to achieve when designing equipment and installations. The principle states that the electric stress, given by the electric field strength, E, applied to the installation

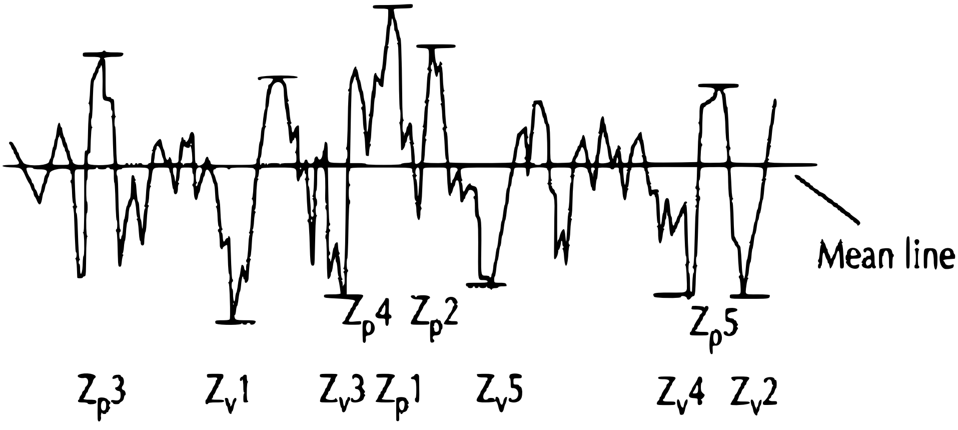

Figure 3.3: Illustration of how to determine the $R_{z,\,ISO}$.Taken from [47].

must be lower than the withstand strength or electric strength, E_d, of the insulation, as illustrated with Equation 3.3. E_d is the highest electric field strength that can be applied without causing failure.

$$\text{Field strength: } E << E_d \text{ :Electric strength} \tag{3.3}$$

This principle is easy to formulate in theory, but difficult to achieve in reality [48]. It should be noted that one should always distinguish between the strength of the electric field and the electric strength of a material. The electric field distribution between two charges is determined by solving the negative gradient of the electric potential field, φ, according to Equation 3.4.

$$\mathrm{E}(x, y, z) = -\nabla\varphi(x, y, z) \tag{3.4}$$

Where φ is determined from *Poisson's equation*, Equation 3.5.

$$\nabla^2\varphi(x, y, z) = -\frac{\rho}{\epsilon} \tag{3.5}$$

Where ρ is the charge density and ϵ is the permittivity of the material in between the two charges. For the derivation of these equations, see e.g. [48]. The electric field distribution have one extreme case known as *uniform electric field distribution*[1]. For uniform field distributions, the electric field strength is constant between the two charges, see Equation 3.6 where V is the applied voltage and d is the gap distance between the two charges. Perfectly uniform electric field distributions exist only between two infinite parallel plates [48].

$$\mathbf{E}(x, y, z) = V/d = E_0 \tag{3.6}$$

---

[1] Also known as *homogeneous electric field distribution*

If the electric field strength varies with the position in the field, the field distribution is known to be *non-uniform*[2] [48]. In reality no perfectly uniform field exist, but field distributions that are close to uniform are known to be *quasi-uniform*. These are often approximated as uniform field distributions according to Equation 3.6 [48].

3.2.1 Electric Field From Rough Surfaces

As explained in Section 3.1 no surface is ideally smooth. They have several small peaks which would each have a field enhancement, a local non-uniform increase of the electric field strength compared to the macroscopic uniform background field strength. The maximum field strength at the surface of a sphere, follows the relationship given in Equation 3.7, where V is the applied voltage and R is the radius of the sphere [48]. When the radius of the sphere goes towards zero, the electric field strength at the surface of the sphere goes to infinity.

$$\lim_{R \to 0} E_{max} = \lim_{R \to 0} \frac{V}{R} = \infty \tag{3.7}$$

The maximum field strength of a rough surface peak can be approximated as a sphere, or having a spherical tip. With modern technology finite element method (FEM) software, e.g. COMSOL, can be used to calculate the electric field distribution from more complex surface structures. In uniform or quasi-unifrom fields, surface protrusions and rough surfaces has a *field enhancement* given according to Equation 3.8, where E_{max} is the maximum field strength at the protrusion and $E_{background}$ is the uniform average background field strength [48].

$$Field\ Enhancement = \frac{E_{max}}{E_{background}} \tag{3.8}$$

In electric insulation, it is the weakest point of the insulation which is critical. Which is why smooth surfaces with single protrusions are considered as rough surfaces [48].

3.2.2 Shielding Effect

Protrusions have field enhancements in uniform background fields. The field enhancement is influenced by neighbouring protrusions, given that they are close enough. When increasing the number of protrusions from one to *n* protrusions, the initial protrusion must *cut* away some of its flux and send it to the *n* new protrusions. When the number of nearby protrusions increases $n \to \infty$ the field strength of the initial protrusion, now surrounded with other protrusions, goes towards the macroscopic background field. The reduction in the maximum field strength due to nearby protrusions is known as the *shielding effect* [49].

---

[2] or *inhomogeneous*

3.3 Breakdown Mechanisms in Gases

At low electric field strengths, gases are very good insulating materials since they have low losses, low conductivity and are nearly frequency independent dielectrics with relative permittivity close to one, $\epsilon_r \approx 1$. When the electric field strength becomes sufficiently high, discharges occur which will be explained in the following sections [48].

3.3.1 Partial Discharges

Gas discharges are divided into *partial discharges*, which causes (small) voltage drops, and discharges that crosses the insulation gap and causes the voltage to drop to zero, known as *breakdowns*.

When a voltage is applied over two electrodes insulated with a gas, a small current can be measured between the electrodes. In non-uniform fields when a sufficient high electric field is reached, the volume close to the electrode becomes highly stressed. Within the stressed region discharges are initiated. Due to the non-uniform field they cannot propagate through the entire gap [48]. These discharges emit light and are known as corona discharges. They are initially caused by Townsend mechanism, which will be explained in Section 3.3.2. Corona discharges occur next to sharp tips and edges or conductors with small radius [48]. In some cases they can be observed with the human eye or be detected with highly sensitive photo equipment.

Further increase of the voltage will cause the inception and growth of *streamer* and *leader discharges*, which will be explained in Sections 3.3.4 and 3.3.6, respectively. Increasing the voltage past the inception of these will in the end cause a breakdown of the voltage in form of arc or spark discharge [48].

3.3.2 Townsend Discharges

In the late 1890s and early 1900s J. S. Townsend discovered that electrical breakdowns in gases with low pressure or small electrode gap distances were dependent upon electron and ion swarms [50]. The discharge process has later been named *Townsend Discharges* and explains the process of *electron avalanches*.

When a free electron exists in the gas and in an electric field, the electron will start to accelerate towards the anode, known as *electron drift* [48]. While the electron moves from the cathode towards the anode, it will collide with atoms and molecules. Initially, the kinetic energy of the electron will be so low that the collisions will be elastic, which conserves most of the kinetic energy. While moving through the gap, the electron will accumulate kinetic energy until an *ionizing collision* happens. These collisions can cause excitation of the molecules or they can release additional electrons from the molecules. The freed electron can then accelerate in the electric field and collide with new molecules that release even more electrons and causes an exponential growth of the number of free electrons in the gas. This is known as an *electron avalanche* and the simplified process is illustrated in Figure 3.4

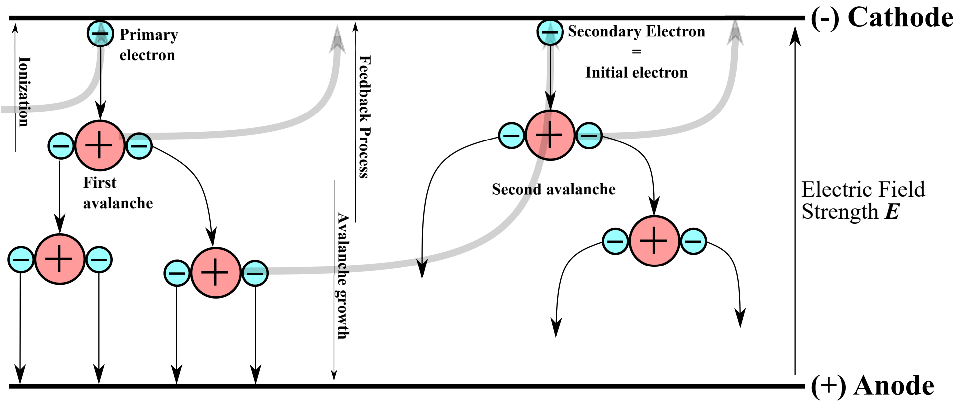

Figure 3.4: Simplified illustration of the generation of avalanches and the ion feedback process. Adapted from [48].

The mechanism described by Townsend included two coefficients, namely *Townsend's first*, α and *second ionization coefficients*, γ. α is defined as the number of free electrons generated through ionization collisions by a single electron per unit length [48].

γ represents the number of secondary electrons generated by each positive charge in the gas. It includes the different processes of ionic impacts on the surface (γ_I), the photoelectric effect (γ_P), impacts from neutral atoms on the cathode (γ_N), release of electrons from field emmision (γ_F), photo emission in the volume (γ_V) and the ion emission from the anode (γ_A) [48]. Thus, the Townsend's second ionization coefficient is given as

$$\gamma = \gamma_I + \gamma_P + \gamma_N + \gamma_A + \gamma_F + \gamma_V \tag{3.9}$$

Townsend presented then what has later been known as *Townsend's ignition criteria*, which is presented in Equation 3.10.

$$\gamma \left(e^{\alpha d} - 1 \right) = 1 \tag{3.10}$$

Where d is the electrode gap length. The criteria is interpreted that breakdown follows when the left side of Equation 3.10 equals 1 [48]. For the full derivation see literature, e.g. [48].

3.3.3 Attachment and Detachment

If the field strength is not sufficient in gases that have high *electron affinity*[3], i.e. the electron attaching gas Sulphur Hexaflouride (SF_6), free electrons will attach to the gas

---

[3] Commonly used expression for this in literature is Electronegativity. However, according to discussions in recent years and described by Küchler [48] electronegativity does not the describe the relevant physical quantity and it is electron affinity that should be used. The reasoning and explanation of the difference can be found in [48].

molecules as they move through the gas and collide with gas molecules [48]. This process is accounted for by the *attachment coefficient* η. η describes how many free electrons that are attached by the gas per unit length.

It is the difference between the free electrons generated, given by the ionization coefficient α, and the electrons which are attached to gas molecules, given by η, that dictates if there will be a growth of free electrons. This is known as the *effective ionization coefficient* α_{eff}, see Equation 3.11.

$$\alpha_{eff} = \alpha - \eta \tag{3.11}$$

Both α and η are dependent on the pressure and the electric field strength and Equation 3.11 can be represented as Equation 3.12 [48].

$$\frac{\alpha_{eff}}{p} = \frac{\alpha}{p} - \frac{\eta}{p} = f\left(\frac{E}{p}\right) \tag{3.12}$$

Electron Detachment

An additional process involved in creating free electrons is *electron detachment* [51], where electrons are released from molecules. There are several different detachment mechanisms, with the main four being: (1) auto-detachment, (2) field-induced detachment, (3) collision detachment and (4) photo-detachment [51]. As (1) and (2) are unlikely to be involved in the discharges in electrical equipment [51], only (3) and (4) will be explained in the following.

The collision detachment mechanism (3) is represented by equation 3.13. Where B is a neutral molecule which through collision with the negative ion A^- can detach an electron from A^- [51]. However, this mechanism have some restrictions. Namely that the ion has to be able to accumulate enough energy to detach an electron in a collision, which might require fields higher than the critical electric field strength of the gas [51].

$$A^- + B \rightarrow A + B + e \tag{3.13}$$

Photo-detachment (4) of a negative ion occurs when a photon with energy, $h\nu$, above the electron affinity of A^- hits A^- and detach an electron from the negative ion A^-, see Equation 3.14, [51]. This mechanism is unlikely to occur as a discharge initiation mechanism, unless an intense light source is used to irradiate the gas. This mechanism may play a role in sustaining the discharge once a discharge emits light [51].

$$h\nu + A^- \rightarrow A + e \tag{3.14}$$

3.3.4 Streamer Discharges

Even though Townsend Discharges could well explain the behavior of breakdowns in gases with low pressures or short gap distances, it did not consider the effects of space charges or photoionization. It was also observed that the formative time lag for the spark formation was much shorter than what the Townsend mechanism could explain [52].

3.3.4.1 Streamer Inception

Raether and Meek discovered independently of each other that when the number of electrons in an electron avalanche reached numbers in the order of $10^6 - 10^8$ space charges would significantly influence the electric field environment in the avalanche [53; 54]. In the avalanche, the mobile electrons will form an approximately spherical *avalanche head* with a negative charge, which increases in diameter through diffusion processes [48]. The less mobile ions will remain in the *avalanche tail* and create a region with positive charge, as shown to the left in Figure 3.5.

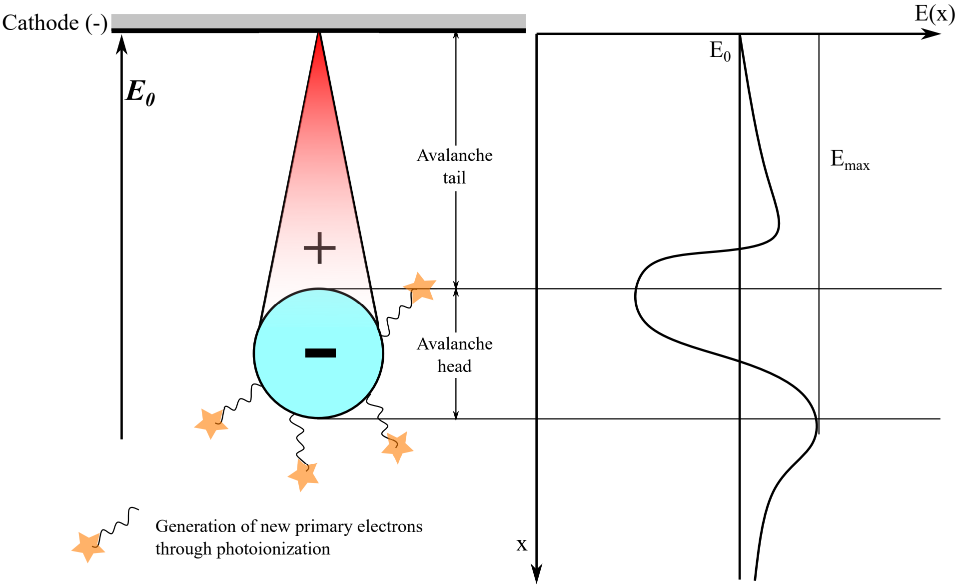

Figure 3.5: Distortion of the background electric field by space charges. Adapted from [48].

Due to the concentration of electrons in the avalanche head, a field enhancement $E(x) = E_{max}$ is caused by the space charges compared to the background field E_0, as shown to the right in Figure 3.5. This field enhancement at the head of the avalanche causes the number of ionizing collisions and photon-emitting recombinations to increase [48]. The emitted photons causes photoionization when they hit molecules in the area close to the avalanche head and generates free electrons which starts new avalanches. The superposition of all the avalanches quickly create a conducitve channel, which is known as a streamer. This is known as the *streamer mechanism* and is illustrated in Figure 3.6 [48]. The photoionization occurs quickly and allows the streamer to cross the gap within the propagation time of a single avalanche [48]. A more physical description of the physics behind the streamer mechanism and how the conductive channel is formed will be explained in Sections 3.3.4.2

and 3.3.5.

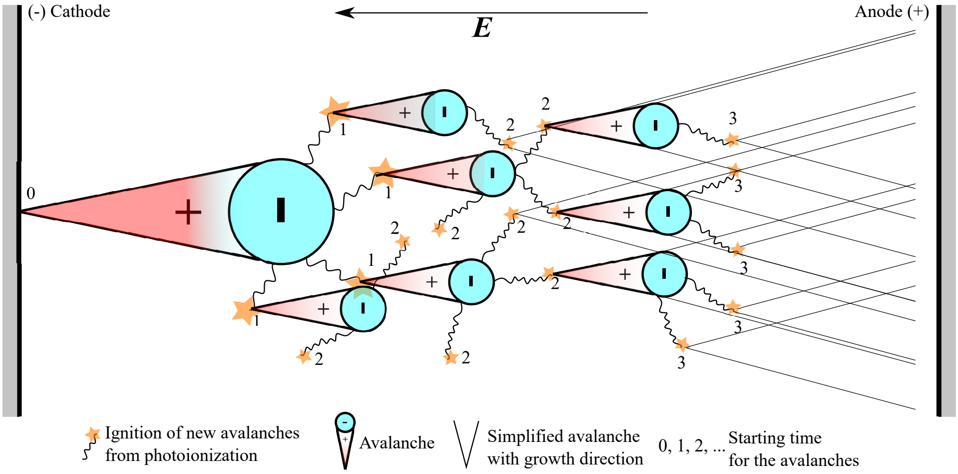

Figure 3.6: Simplified physical streamer model. Adapted from [48].

For a breakdowns to occur, it is a precondition that there are generated more electrons from ionization collisions than the attachment of electrons, as explained in Section 3.3.3. This means that α_{eff} from Equation 3.12 has to be greater than zero ($\alpha_{eff} > 0$). Additionally, the number of electrons must reach the *critical value* N_{crit} [48]

$$N_{crit} = 10^6 \ldots 10^8 \tag{3.15}$$

Raether's ignition condition for the streamer mechanism is [53; 48]

$$e^{\int_0^d \alpha_{eff}\,\mathrm{d}x} \geq N_{crit} \tag{3.16}$$

or more commonly represented

$$\int_0^d \alpha_{eff}\,dx \geq \ln(N_{crit}) = K \tag{3.17}$$

Where d is the gap length and K is a constant depending on the insulation gas. This is also known as the streamer inception criterion. For non-uniform fields Equation 3.17 is not to be solved for the entire gap, it is only solved for the region where $\alpha_{eff} > 0$. If the number of electrons reaches the critical number, the space charge in the avalanche will be enough for a self-sustained growth into the region where the electric field is low and $\alpha_{eff} < 0$ [48].

3.3.4.2 Streamer Mechanism

Streamers are divided into *positive* and *negative* streamers, depending on the involved mechanism.

Positive Streamers

Positive streamers or *cathode directed streamers*, move from the anode towards the cathode, see Figure 3.7. When an electron avalanche moves from the cathode towards the anode, a low mobile positive space charge is accumulated at the head of the avalanche (A). When the avalanche reaches the anode, the electrons are absorbed into the electrode leaving behind a cloud with net positive space charge (B). Close to the avalanche head, recombination of positive ions and electrons causes many high energy photons that will generate new primary electrons and avalanches in the region around the positive space charge. If the number of positive ions is large enough, the field strength becomes comparable with the background field strength. The secondary avalanches will then be attracted towards the positive charge cloud (C). When the secondary avalanches reaches the cloud, the electrons are neutralized by the positive charge and creates a streamer channel and a new positive net charge is left behind a little bit closer to the cathode. This process repeats itself until the positive space charge cloud (or head) moves from the anode to the cathode (D) [55]. The positive streamer can propagate in electric field strengths which are much lower than the required field necessary to have $\alpha_{eff} > 0$. Due to the ionization occurring in electric field created by the space charges the streamer head [55].

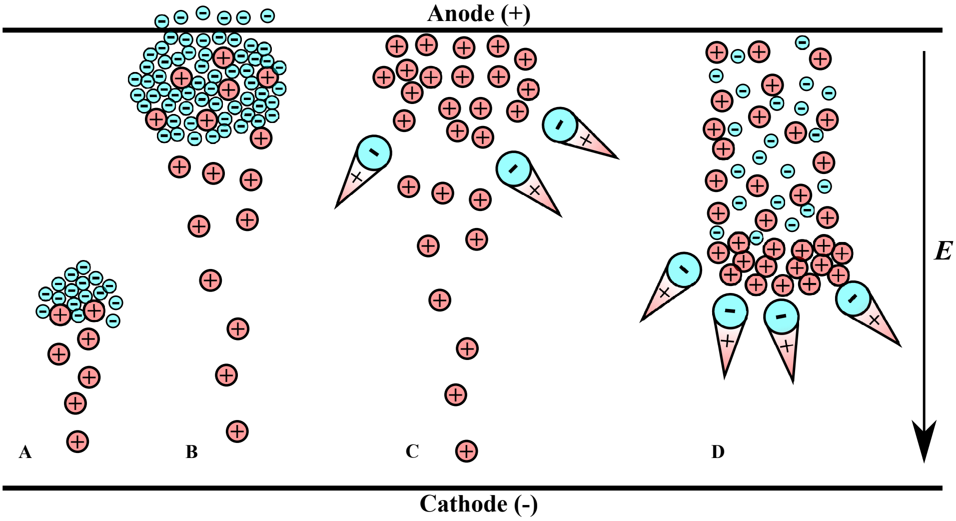

Figure 3.7: Schematic illustration of the formation of a positive streamer. Adapted from [55].

Negative Streamers

The formation of a negative streamer or *anode directed streamer* is illustrated in Figure 3.8. When the avalanche reaches the critical number of electrons. The electrons will move into the gap towards the anode while leaving behind the more immobile positive ions. The positive ions will move towards the cathode (A). When the positive space charge cloud reaches the cathode, electrons will be released from the cathode due to field emission caused by the field enhancement of the positive space charge cloud and from ionic impacts on the cathode surface. The released electrons will neutralize the positive space charge cloud and create a weakly conducting channel that connects the negative avalanche head to the cathode (B). The high electric field strength of the avalanche head will cause the streamer channel to propagate into the gap, while the positive space charges left behind is neutralized with electrons supplied from the cathode (C) [55].

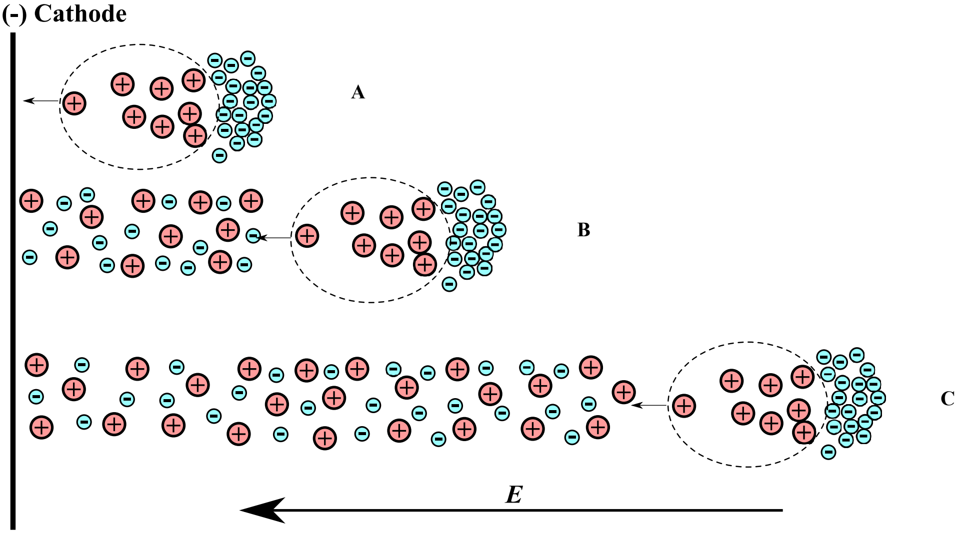

Figure 3.8: Schematic illustration of a negative streamer. Adapted from [55].

3.3.5 Streamer to Spark Transition

Even if the electric field is strong enough to initiate a streamer or streamers to cross the gap, it is not so that it will directly lead to breakdown of the voltage. This is because the streamer is a so called *cold discharge*, which means that the temperature in the streamer channel is close to the ambient temperature. Additionally, the conductivity of the streamer channel is rather small [55]. For an electric breakdown to occur in the electrode gap, the streamer channel must be converted into a highly conductive channel. This occurs in a process called *streamer to spark transition* [55].

The streamer to spark transition is as follows [56; 57; 58; 59]. A propagating streamer will create an ionized track that will cross the gap if the electric field is strong enough, i.e. the background electric field, $E_{bg} = V/d$, is above the streamer stability, field E_{st} [59]. When the streamer and the ionized track crosses the gap it will cause a cathode fall region at the cathode, which is a sharp drop of the voltage in the ionized channel at the cathode [55]. The next stage of the streamer discharge development is the propagation of an electric potential wave [59]. After several tens of nanoseconds the axial distribution of the electric field becomes nearly uniform. After this it is the background field E_{bg} which governs the following plasma development. If the background field is noticeably lower than the critical field, E_c, where the ionization and attachment coefficients of the gas are equal, then the mean net ionization rate will be negative ($\alpha_{eff} < 0$). This will lead to a decrease of the conductivity of the channel and of the current in the channel over time [59]. However, there are several processes in the plasma that tend to decelerate the decay and are able to change the sign of the net ionization rate, α_{eff}, to positive. Resulting in increased conductivity and current, which eventually leads to breakdown. Two major processes are a thermal and a kinetic mechanism [59].

In the thermal mechanism, the electrons and ions move through the electric field. As they move they generate ohmic heat along their trail, where a smaller fraction (approximately 15 %) is released immediately. The remainder is stored in vibrational states in the molecules and released as heat over time causing the gas temperature to increase in the channel [60]. A temperature increase in the channel gives, according to the ideal gas law ($p = NkT$, p = pressure, k = the Boltzman constant and T = temperature) an increase of the pressure in the channel [58]. In order to bring the pressure back to the normal *background* pressure, the neutral molecules within the channel begins to move radially outwards from the channel axis leading to a decrease of the neutral gas density *N* near the axis. Which is balanced by an increase near the edges of the discharge channel [58]. The decrease of the neutral density, *N*, increases the reduced electric field, *E/N*, which causes an increase of the effective ionization coefficient α_{eff}, due to its dependence on *E/N* [59]. This causes increased ionization in the discharge core and an increase in the electron density [58].

The kinetic mechanism considers the accumulation of active particles, consisting of radicals and excited molecules. The active particles change the balance between the generation and loss of electrons. The processes that impacts this balance are: direct ionization, the sum of the rates of ionization of excited molecules and radicals by electron impact, associative ionization, detachment, attachment and electron-ion recombination in the gas [61]. These processes cause the gas to heat up until the temperature is high enough (about 5000 K in dry air) for thermal ionization to take over and drive the ionization [61].

For both mechanisms, the ionization occurs until a highly conductive plasma is created between the electrodes and a spark which is characterized by an intense light emission forms [48]. The time from streamer crossing to breakdown decrease quickly with increasing applied voltage, which is equivalent with increasing reduced field, *E/N*, see Figure 3.9. For transition times in the nanoseconds range it is the kinetic mechanism that is the dominant process. While at lower field strengths, where the transition time increases, both the kinetic mechanism and the channel expansion due to the thermal mechanism are important for driving the spark transition [59].

3.3.6 Streamer to Leader Transition

Breakdowns can be observed at electric field strengths where streamer inception has occurred, but the field is not strong enough for the streamers to propagate across the gap. Each individual streamer does not have the required energy to heat the gas and make it conductive. The process causing breakdowns is known as the *streamer to leader transition* or *leader breakdown mechanism* [55]. The leader breakdown mechanism starts with

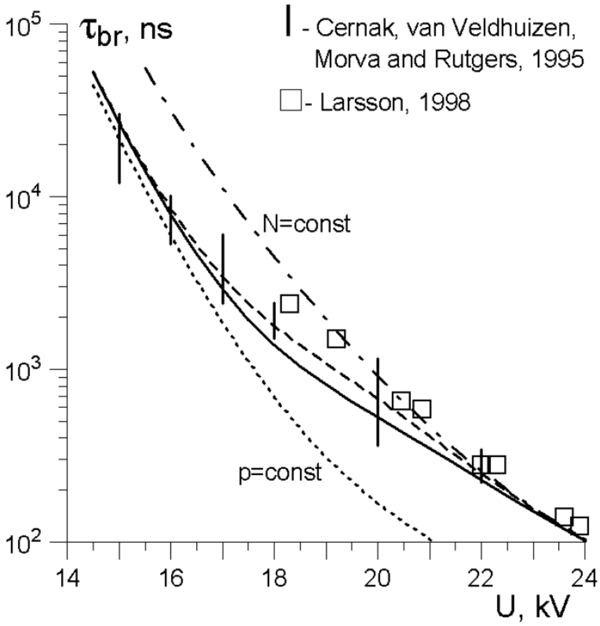

Figure 3.9: The time, τ_{br} for streamer to spark transition plotted against the applied voltage. Lines show simulations with different constant parameters. Taken from [59] showing results from Cernak et al [62] and Larsson [63] as symbols.

the initiation of a first corona. Within the first corona several streamers are formed. The streamers propagate into the gap until the requirement for propagation no longer is fulfilled [64; 65; 66]. As the streamers die down, there is a pattern of positive and negative ion channels left behind [66]. In these remnants of corona, there are two major processes that occur. These are known as the *stem mechanism* and the *precursor mechanism* [64; 65; 66].

The stem mechanism (right in Figure 3.10) is when all the streamers feed their current into the stem and causing the region to heat up and increase the conductivity [55; 66]. If enough streamers feed their current, the thermal expansion of the stem will make the critical field drop below a certain value, initiating ionization and creating a conductive channel which becomes a section of the leader [66].

The precursor mechanism (left in Figure 3.10) is related to the ion drift of the remnants of the streamer corona. The ions drift apart creating space charge filaments which locally enhance the electric field enough to restart ionization. The currents caused by the ionization leads to a field distortion and eventually creates a conducting channel which propagates towards the electrode creating a section of the leader [66].

The stem mechanism is initiated at the electrode and propagate towards the edge of the corona. The precursor mechanism is initiated in between the edge of the corona and the electrode and propagates towards the electrode. The result from both mechanisms is *leader inception*, which is a conductive channel that is created bridging the electrode and the

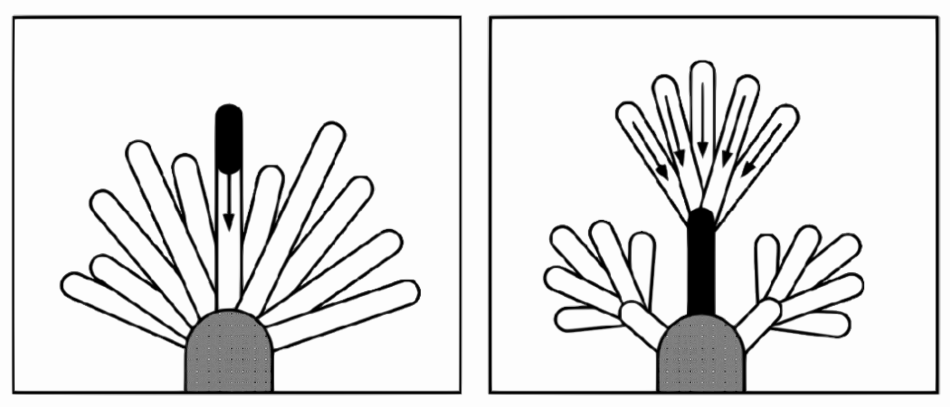

Figure 3.10: Schematics of the precursor mechanism to the left and the stem mechanism to the right. The charge injection from the streamers into the stem is indicated by arrows. Taken from [7].

corona extension. The conductive channel behaves as an extension of the electrode and creates a field enhancement which causes a new corona. The current from the streamers in the new corona feed current to either the stem or precursor filament causing the channel to expand through ohmic heating [66]. It is likely a combination of both the stem and precursor mechanism when a step of the leader is created [7].

The formation of the leader propagates through the gap with each new leader section functioning as an extension of the electrode for inception of the next corona. This allows the leader to propagate through gaps and electric field regions where streamer are unable to propagate [66]. The ability for the leader to propagate through the gap is determined by the electric field strength around head of the leader channel and the field in the streamer zone in front of the leader. The step-wise propagation of the leader occurs until the corona region or streamer reaches the opposite electrode or until the the conditions for the stem or precursor mechanisms no longer are met [66]. When the corona region or a streamer reaches the opposite electrode, the leader reaches the *final jump* and is characterized by an increase of the channel's luminosity and the voltage breaks down [55].

3.3.7 Breakdown Overview

A simplified flowchart of the breakdown process from the first electron is given in Figure 3.11. When a first electron is initiated and the electric field is of sufficient strength to fulfill the streamer inception criterion, streamers occur (Figure 3.11-1). If the electric field is large enough for streamers to cross the gap (Figure 3.11-2) and is large enough streamer to spark transition will occur (Figure 3.11-3) resulting in a breakdown. leaders can form in the streamer channel if the electric field is strong enough to cause crossing streamers, but not large enough to cause streamer to spark transition (Figure 3.11-4) or the process dies out after streamer crossing (not shown). If the field is not large enough to cause streamer crossing, breakdowns can occur from leader inception (Figure 3.11-5) and leader breakdowns when the leader crosses the gap (Figure 3.11-7). Streamer or leader that crosses only parts of the gap but dies out before causing breakdowns are known as *arrested streamers* and *arrested leaders* (Figure3.11-6 and -8, respectively).

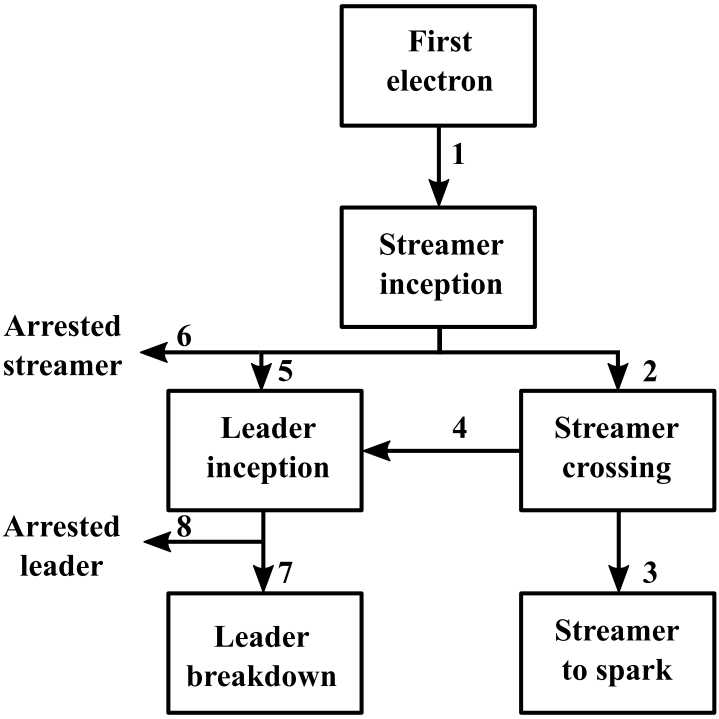

Figure 3.11: Schematic flowchart of breakdowns in gas at high pressures. Adapted and simplified from [13].

For most of gases the negative breakdown voltage is higher than the positive breakdown voltage [48]. However, recent investigations of CO_2 indicate that this relationship is not always true [40] as commonly stated in literature [48; 50]. This will be explained further in Section 3.4.2.

3.3.8 Stochastic Behavior of Breakdowns

When stressing an electrode gap with an impulse voltage, the breakdown of the gap does not always occur at the same voltage due to the stochastic behavior of the breakdown process. If an electrode gap is stressed with a constant voltage for infinite amount of time, there will be a certain voltage limit V_0 which separates certain breakdown above V_0 and no breakdowns below V_0. After a voltage is applied above V_0. a breakdown will happen when there is a free electron that is capable of generating an electron avalanche [55]. The time it takes from the voltage is applied above V_0 at $t = t_0$ until an electron occurs in the gap is known as the *statistical time lag* t_s. The time it takes for a conductive channel to be created in the gap is known as the *formative time lag* t_f. When a conductive channel has been created, the time for the voltage to collapse is the *time of voltage collapse* t_c. Compared to the statistical and formative time lags, the time of voltage collapse is very small and can normally be neglected. The total time to breakdown is then represented by

$$t_T = t_0 + t_s + t_f + t_c \tag{3.18}$$

where t_0 is the time from the impulse is turned on until it reaches the voltage limit V_0.

Impulse voltages have a short rise time to their peak before they relatively slowly decline, which makes the breakdown voltages scatter more compared to slowly rising DC voltages [48; 55]. The reason is that the impulse voltage (1) has to rise above the voltage limit V_0 and (2) it has to remain above V_0 long enough for a discharge to be completed. Due to the stochastic nature of the first electron generation and the stochastic processes of the breakdown mechanisms, the breakdown voltage and times will be different for each application of voltage impulses. One can apply the same impulse with the same peak above the limit V_0 and in one case have a breakdown of the voltage and in another a breakdown will not occur due to the lack of a first electron before the the impulse drops below V_0. To deal with this, breakdown voltages are determined by the *percent breakdown voltage*. Typically the *50 % breakdown voltage* V_{BD-50} is used and it represent the voltage that causes breakdown 50% of the times it is applied [55]. Another commonly used value is the *statistical withstand voltage* [12] and is the highest voltage that does not cause a breakdown [55]. Another Common value used for the withstand voltage for design purposes is the 2% breakdown voltage V_{BD-2} [13].

3.4 Gas as an Insulation Material

In high voltage engineering several different insulation materials with very different properties are used. Examples are gases, inorganic solids, polymers, liquids and fibrous materials [48]. In this theory section, only gases used in high voltage insulation will be considered.

For insulation purposes, gases are ideal as an embedding media due to their ability to uniformly fill all available cavities [48]. There are several requirements tto be an insulation gas [50]:

- The gas should have high dielectric strength.
- The gas should have a working range over the temperature span $-30°$ to $+60°$C. In other words, it should not liquefy at low temperatures.
- The gas and its decomposition products created from partial discharges or breakdowns should not react chemically with other materials.
- The gas and its decomposition products should not be flammable or toxic.
- The gas should preferably be inert and have a high density.

One of the most common gas mixtures that operates as electrical insulation is atmospheric air [48; 50]. There are several advantages with atmospheric air, one is that it is naturally occurring and does not require any special processing or treatment [48]. As the transmission voltages increases, the limitations of the dielectric strength of atmospheric air combined with the nonuniform fields in the equipment used in atmospheric air requires very large gaps. The increase in size is not only aesthetically displeasing, but also requires a huge economic cost in the required material and land [50]. One way to reduce cost and size is to use gas insulated systems (GIS), where the property of increasing insulation strength with increasing pressure for gases is exploited. Since the dielectric strength of air is not very strong, even at higher pressure other dielectric gases was sought after. The most suitable gas and most used gas since the 1960s in GIS due to its electron-affine properties is sulphurhexafluoride, SF_6 [48; 50]. The properties of SF_6 as an insulation gas will be explained more in detail in Section 3.4.1.

In recent years, the awareness and expansion of global energy infrastructure, the usage of gas insulated systems has increased drastically. The global warming potential of SF_6 is 23 900 times larger compared to CO_2 on a 100 year horizon [8]. Combined with increased usage have caused the interest in alternative insulation gases to increase in recent years [48]. One alternative gas to SF_6 which has many favorable properties is CO_2 and the properties of CO_2 will be explained in Section 3.4.2 [48].

Other potential gases that show promise with high dielectric performance are complicated molecules e.g. fluoronitriles (Heptafluoro-iso-butyronitrile) [67], iso-C4 perfluoronitrile or the C5 perfluoroketone of the perflouroketone family [15]. Even though these gases show good promise when pure, they have a very high boiling points and require to be mixed with a buffer gas, e.g. CO_2, to be able to operate in the required range of temperatures [15]. The mixture of 3.7 % Fluoronitriles and 96.3 % investigated by Nechmi et al in [67], reached 72 % of the performance of SF_6 at 5.5 bar absolute. The mixtures presented at the CIGRE workshop [15] and by Nechmi et al also have a significantly lower global warming potential compared to that of SF_6.

3.4.1 Sulfur Hexafluoride (SF_6)

SF_6 was first produced in 1900 by the scientists Moissan and Lebeau. Since 1950 it has been increasingly used in high voltage applications due to its high dielectric strength, especially under higher pressures [50]. The SF_6 molecule has a rigid symmetrical structure where six fluorine atoms are arranged uniformly like an octahedron on a central sulphur atom [50]. The rigid structure combined with the small binding distance and high binding energy between the atoms causes the SF_6 molecule to be very stable at atmospheric conditions [48; 50; 13]. Characteristics of the SF_6 include [48; 50; 13];

- A relatively low condensation temperature of $-63°C$ at 1 bar pressure, which allows it to be used at low ambient pressures. However, at higher pressures SF_6 the condensation temperature increases to $-30°C$ at 5 bar pressure. In these situations SF_6 can be mixed with other gases, like N_2 to reduce the condensation temperature.
- As previously mentioned, the SF_6 molecule is very stable and it is not toxic.

- The SF_6 components are very reactive, so they immediately re-combine to inert SF_6 molecules, when electric breakdowns that deteriorate the gas occur and breaks it down into its components

- SF_6 has a high electron affinity which makes free electrons attach to the molecules.

The theoretical intrinsic strength of SF_6 is given as $E/P = 89\,\mathrm{kV/cm \cdot bar}$. Which means that theoretically no breakdown should occur below this pressure reduced electric field [13; 50].

As SF_6 is a gas with high electron affinity, the effective ionization coefficient represented by Equation 3.12 can be described by a linear postulated solution with empirically determined constants [48]

$$\frac{\alpha_{eff}}{p} = k_i \left(\left(\frac{E}{p} \right) - \left(\frac{E}{p} \right)_0 \right) \tag{3.19}$$

where $k_i = 27.7$ /kV and $(E/p)_0 = 88.4$ kV/cm · bar (or $(E/p)_0 = 89$ kV/cm · bar [13]) at a temperature of $T = 293$ K [48].

SF_6 is a very large gas molecule, which gives it a very small mean free path. Combined with SF6's high electron affinity gives it a high dielectric strength due to its ability to *catch* free electrons. The distance for electrons to accumulate energy is short. Thus, the electrons get attached to SF_6 before they manage to create ionizing collisions [68]. However, this short mean free distance makes SF_6 sensitive to strong non-uniform fields, making the distance that α_{eff}, which also has a very steep rise, has to be greater than zero very short. When the field is strong enough to cause ionizing collisions, the electrons have short distances to travel to ionize new SF_6 molecules and create avalanches [68]. Making the critical length necessary for fulfilling the streamer inception criterion, and subsequently the leader inception criteria, very short. Which is the reason why SF_6 is sensitive to surface roughness and protrusions, especially at higher pressures [13; 50; 48].

3.4.2 Carbon Dioxide (CO_2)

The insulation properties of CO_2 was investigated in the 1970's and 1980's as a cheaper alternative to SF_6 that could behave just as well in gas insulated systems (GIS). Another reason for investigating CO_2 was to expand the physical understanding of the breakdown mechanisms in CO_2, other gases and their mixtures [69]. In recent years, due to the classification of SF_6 as a climate gas [8], more effort has been put into researching alternative gases, where CO_2 has been shown to be a promising alternative that fulfills the criteria that is required of an insulation gas.

CO_2 is an inert, non flammable electron attaching gas [70]. Which makes it an option not only for gas insulated lines, but also for breaking currents in gas circuit breakers [71]. CO_2 has a low toxicity and a boiling point at -78.5 °C at atmospheric pressure, which is lower than that of SF_6. Which makes it a viable option for use at the low temperatures [15]. However, the dielectric performance of CO_2 is around 32-37 $\%$ that of SF_6, which requires it to be used at higher pressures to reach equivalent insulation properties of SF_6. The critical field in CO_2 is calculated to be approximately 21.5 kV/(cm·bar) at room temperature [72] and measured to be approximately 21.25 kV/(cm·bar) [73].

3.4.2.1 Breakdowns in CO2

It has been found that the electric field strength required in a uniform field with a single protrusion for streamer crossing is higher for positive than for negative streamers [40]. With positive polarity of the protrusion (positive streamers), the expected breakdown cause is leader breakdowns. Since a crossing streamer does not mean that there will be a breakdown, a higher electric field strength is required for the streamer to spark transition. This is illustrated in the red area of Figure 3.12a. The positive leader criteria is expected to be lower than the positive streamer crossing field strength, which is illustrated by the solid line. However, due to the uncertainties of the first electron generation, the electric field strength required will be higher than just the electric field strength needed for leader breakdown given a first electron. For negative polarity, the streamer crossing and streamer to spark is lower than that of the negative leader breakdown for smaller protrusion lengths [40], which means that for short protrusions streamer crossing and streamer to spark transition will be the determining breakdown mechanism. This is illustrated in Figure 3.12b.

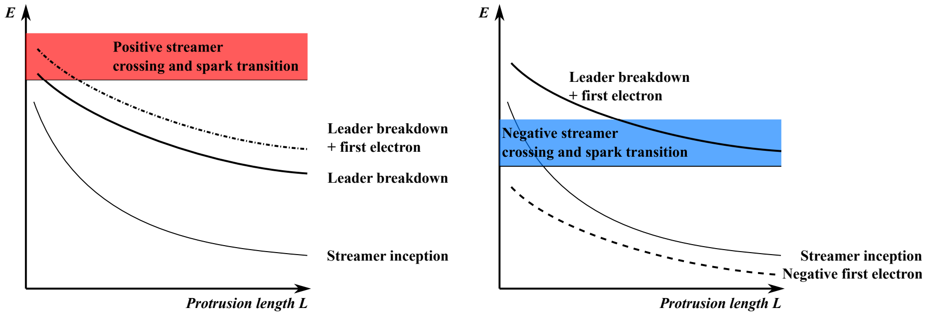

(a) Positive polarity

(b) Negative polarity

Figure 3.12: Principal illustration of the breakdown mechanism in CO_2 with a uniform background field and a single protrusion plotted as functions of electric field and protrusion length.

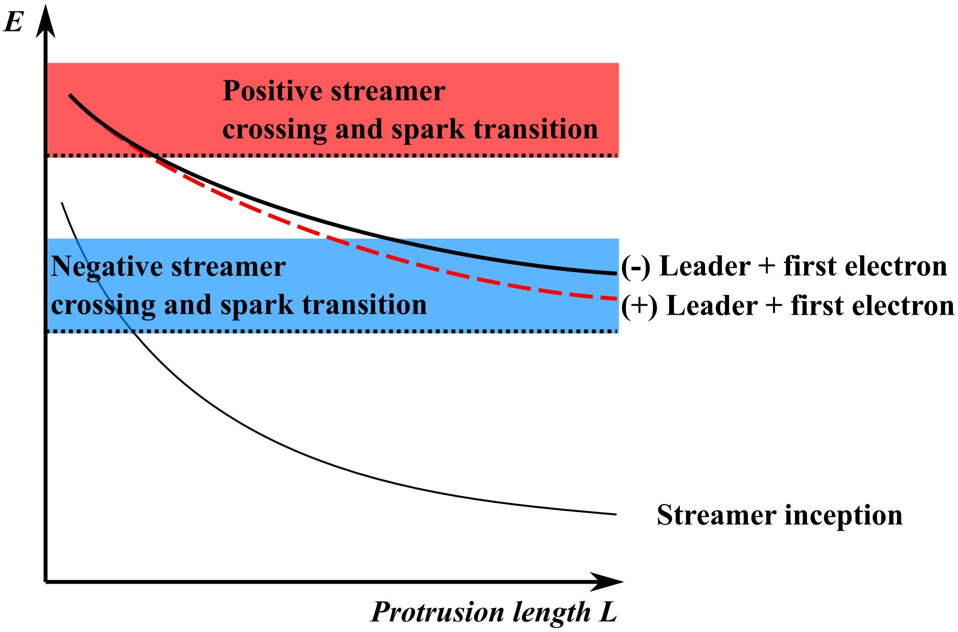

Figure 3.13: Principal illustration of the breakdown mechanism for both polarities in CO_2 with a uniform background field and a single protrusion plotted as functions of electric field and protrusion length.

3.5 Probabilities and Statistics

Initially some definitions of probability theory and statistics will be given. Mostly the basics and the mathematical proofs will be skipped, more detailed explanations can be found in the literature, e.g. [74], [12] and [75].

3.5.1 Basic Concepts

The world is full of random events, if something with a stochastic nature, the outcome will vary each time it is repeated. Consider flipping a coin as an *experiment*, or *trial*. Each result of an experiment is a subset of the *sample space*, all possible outcomes, and are called *events*. These random events are assigned a *probability* p, which is a number between 0 and 1 that indicates how likely something is to happen [74]. If an experiment is repeated n times, n is known as the *sample size* [74]. If the event A occurs m times in the n trials. The *relative frequency* $h_n(A)$ is then found from Equation 3.20 [12].

$$h_n(A) = \frac{m}{n} \tag{3.20}$$

The more times the trial is repeated, the relative frequency will oscillate and converge against a fixed value which it will reach as its limiting value if it is repeated $n \to \infty$ times

[12].

$$\lim_{n \to \infty} h_n(A) = p(A) \tag{3.21}$$

$p(A)$ is referred to as the *statistical probability* for the random event A [12]. It is not possible to repeat an experiment infinite amount of times, so the probability is estimated based on the relative frequency $h_n(A)$. It follows that the larger the sample size the closer the estimated statistical probability $p(A)$ is to the real probability $P(A)$[12; 74].

3.5.2 Distribution Functions

The *distribution function*, also known as the *cumulative distribution function*, of the variate X contains all the probabilistic information about X. The *distribution function* F is defined by [74; 12]:

$$F(a) = P(X \leq a) \qquad \text{for} - \infty < a < \infty \tag{3.22}$$

Where a is a numerical value. The distribution function at the point a is the probability that the variate X has a value lower than or equal to a [12]. For continuous variates, the distribution function can be represented as

$$F(a) = P(x < a) = \int_{-\infty}^{a} f(x)\,dx \tag{3.23}$$

where $f(x)$ is the *probability density function* which is in relationship to the distribution function as

$$f(x) = \frac{d}{dx}F(x) \tag{3.24}$$

Further explanations of distribution functions can be found in e.g. [12; 74].

3.5.3 Normal Distribution

When a large number of independent and randomly distributed variates are summed, and each variate contributes only with an insignificant amount to the sum, they produce a normally distributed variate. Which has several applications to random phenomena [12]. The normal distribution has the following density function:

$$f(x,\, \mu,\, \sigma^2) = \frac{1}{\sqrt{2\pi\sigma^2}} e^{-(x-\mu)^2/2\sigma^2} \tag{3.25}$$

and distribution function:

$$F(x,\, \mu,\, \sigma^2) = \frac{1}{\sqrt{2\pi\sigma^2}} \int_{-\infty}^{a} e^{-(x-\mu)^2/2\sigma^2}\,dx \tag{3.26}$$

where μ is the median of the distribution and σ^2 is the variance of the distribution.

3.5.4 Weibull Distribution

In 1951 Waloddi Weibull proposed a simple distribution function with a wide application, it covered the statistical behavior of several natural phenomenon like the size distribution of fly ash, fatigue life of a type (St-37) of steel and the fiber strength of Indian cotton [76].

Weibull stated that any distribution function may be written in the form

$$F(x) = 1 - e^{-\phi(x)} \tag{3.27}$$

The criteria Weibull set for the function $\phi(x)$ was that it had to be:

- positive
- non-decreasing
- Vanish at a value x_u, which not necessarily would be equal to zero.

The simplest function to satisfy this, according to Weibull[76][4], is

$$\phi(x) = \left(\frac{x - x_u}{x_0}\right)^m \tag{3.28}$$

Giving the distribution function

$$F(x) = 1 - e^{-\left(\frac{x - x_u}{x_0}\right)^m} \tag{3.29}$$

Equation 3.29 has later been named the Weibull distribution. More specifically Equation 3.29 is called the *three parameter Weibull distribution*, due to its' three unknown parameters, x_u, x_0 and m [12]. The Weibull distribution is an example of an extreme-value distribution, meaning that it either has a minimum or maximum (extreme) value[12]. The Weibull distribution is limited in a downward direction, which means it has a value where there are no probability for the event to happen, and unlimited in an upward direction. Often the lower limit is set to zero ($x_u = 0$). For instance measuring the time to failure for an arbitrary number of electrical test subjects, one can assume that no one fails before the voltage is turned on when the measuring starts. This produces what is known as the *Two-Parameter Weibull Distribution* shown in Equation 3.30[12].

$$F(x) = 1 - e^{-\left(\frac{x}{x_0}\right)^m} \tag{3.30}$$

Another special-case of the Three Parameter Weibull distribution is when $x_u = 0$ and $m = 1$, then the Weibull distribution turns into the exponential function [12]

---

[4] Weibull actually has a misprint in his original paper, where he wrote $\frac{(x-x_u)^m}{x_o}$. This was discovered by T. C. Tsu and it was clarified in the discussion the following year that the functions presented in Equations 3.28 and 3.29 are the correct ones.

$$F(x) = 1 - e^{-\lambda x} \tag{3.31}$$

Where $\lambda = 1/x_0$.

The expected mean value of the Weibull distribution and its variance can be found from Equations 3.32 and 3.33, respectively [12].

$$Ex = x_u + x_0 \Gamma \left(\frac{1}{m} + 1 \right) \tag{3.32}$$

$$Var\, x = x_0^2 \left(\Gamma \left(\frac{2}{m} + 1 \right) - \Gamma^2 \left(\frac{1}{m} + 1 \right) \right) \tag{3.33}$$

Where Γ is the gamma function given as [77]

$$\Gamma(z) = \int_0^\infty t^{z-1} e^{-t} \, dt \tag{3.34}$$

Where z is a real number greater than zero. The gamma function can be written for integers as [77]:

$$\Gamma(n+1) = 1 \cdot 2 \cdot ...(n-1)n = n! \tag{3.35}$$

for $n = 0, 1, 2, 3....$

3.5.5 Quantiles

From a technical/industrial point of view, it is not necessarily the median or mean value of a distribution which is of interest [74]. Consider a chemical reactor that has an inflow of chemicals and an outflow, where the chemicals stay in the vessel according to an arbitrary distribution with a mean time of 4(T) minutes. However, there is a minimum time, for which the chemicals must stay in the vessel to participate in the chemical reaction. The interest is to have it so at least $90\,\%$ of the chemicals stay in the vessel for the minimum time. The interest is then to find a number q with the property that $P(T > q) = 0.9$ or equivalently $P(T \leq q) = 0.1$. The number q is called the 0.1th quantile or the 10th percentile of the distribution [74]. According to [74] quantiles are defined as: ”For a continuous variate X, p is a number between 0 and 1, the pth *quantile* (or $100 \cdot p$th *percentile*) of the distribution of X is the smallest number q_p such that

$$F(q_p) = P(X \leq q_p) = p \tag{3.36}$$

”

The median is the 50th percentile for all distributions [74].

3.5.6 Confidence Intervals

When calculating the mean of a data set with an underlying distribution the calculated mean is a *point estimate* of the distribution mean. That is if the mean was to be represented by a single number [74]. If one were to take a different data set based on the same underlying distribution, the estimated mean would be different. However, both estimates for the actual mean would be close to the actual mean of the underlying distribution (given a sufficient data set). A *confidence interval* gives an interval with a certain $\gamma - \%$ probability that the true mean lies in between the values. If one constructs the 95 $\%$ confidence interval of the mean, then 95 $\%$ of the times, the mean would lie within that interval. This also means that in 5 $\%$ of the times, the mean will lie outside the interval [74]. As one can find confidence intervals for point estimates, it is also common to give confidence intervals or *confidence bands* when results are given as distributions. Which presents with a certain, e.g. 95 $\%$, confidence that the distribution lies between two bands [12].

3.5.7 Enlargement Law

Considering two identical and independent electrode setups that have breakdown probabilities for a given voltage as $p_1 = p_2 = p$. If either one fails, the system fails. The probability for one failure is then given as Equation 3.37

$$P(At\,least\,One\,Failure) = 1 - P(No\,failures) \tag{3.37}$$

The probability that neither fails can then be found to be

$$P(No\,failure)_2 = (1 - p_1)(1 - p_2) = (1 - p)^2 \tag{3.38}$$

The probability of failure in Equation 3.37 becomes then for the two electrode setups

$$P(At\,least\,One\,Failure)_2 = 1 - (1 - p)^2 \tag{3.39}$$

Adding until there are n identical and independent electrode setups the probability for no failures would be given as

$$P(No\,failure)_n = (1 - p_1)(1 - p_2)...(1 - p_n) = (1 - p)^n \tag{3.40}$$

Assuming identical probabilities Equation 3.37 becomes

$$P(At\,least\,One\,Failure)_n = 1 - (1 - p)^n \tag{3.41}$$

This is known as the enlargement law [12]. The enlargement law is illustrated for three different probabilities (0.01, 0.05. 0.10) With $0 \leq n \leq 500$ in Figure 3.14.

For the complete distribution functions $F_1(x)$ and $F_n(x)$ the relationship becomes similarly

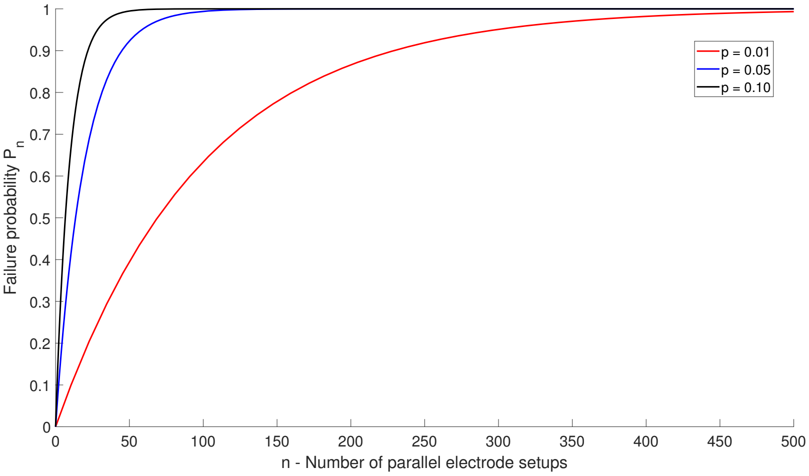

Figure 3.14: Enlargement law illustrated for three different probabilities.

$$F(x)_n = 1 - (1 - F(x))^n \tag{3.42}$$

Where it is assumed that $F_1(x) = F_2(x) = ... = F_n(x)$. For the two parameter Weibull distribution presented in Equation this becomes

$$F(x)_n = 1 - (1 - F(x))^n = 1 - (1 - (1 - e^{(\frac{x}{\alpha})^\beta}))^n$$

$$F(x)_n = 1 - e^{n(\frac{x}{\alpha})^\beta} \tag{3.43}$$

The effect of increasing the number of identical setups on the cumulative distribution function is illustrated with a two parameter Weibull distribution in Figure 3.15.

The more identical setups that are added, the steeper and pushed to the left the final distribution becomes. When the number of identical setups goes towards infinity, distributions that has a zero probability point, like the Weibull, will converge towards a step distribution at the zero point location.

The enlargement law is also applicable to other expansions than just adding identical parts, but it can be used to see the effect of increasing area of electrodes, volume of insulation and time of applied voltage

- Area:

$$n = \frac{A_n}{A_1} \tag{3.44}$$

- Volume

$$n = \frac{V_n}{V_1} \tag{3.45}$$

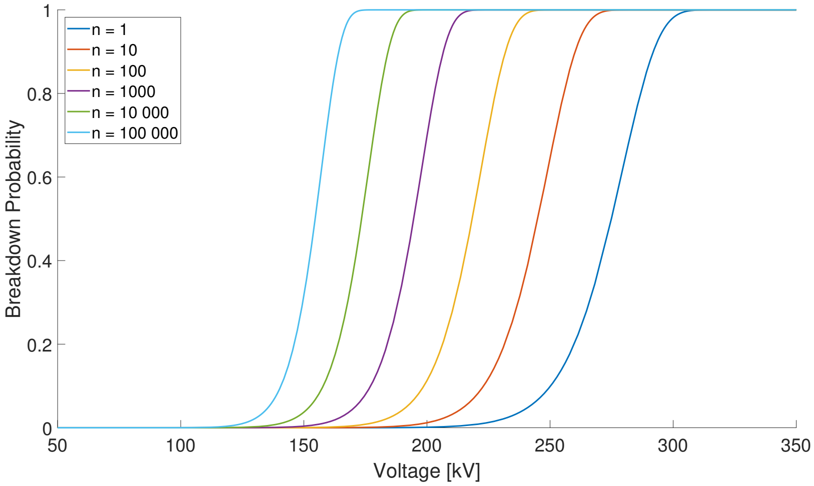

Figure 3.15: Enlargement law illustrated for a two parameter Weibull Distribution with $\alpha = 280$ and $\beta = 20$.

- Time:

$$n = \frac{T_n}{T_1} \tag{3.46}$$

When faced with more realistic situations where one rarely have identical elements, instead the elements have different probabilities and probability distributions. For n elements with different probabilities, the probability for no failures becomes

$$P(No\,failure)_n = (1 - p_1)(1 - p_2)...(1 - p_i) \qquad i = 1, \dots, n$$

$$P(No\,failure)_n = \prod_{i=1}^{n}(1 - p_i) \tag{3.47}$$

This then gives the probability for failure

$$P(One\,failure)_n = 1 - \prod_{i=1}^{n}(1 - p_i) \tag{3.48}$$

In similar fashion as Equation 3.42 was found, the cumulative distribution function then becomes

$$F(x)_n = 1 - \prod_{i=1}^{n}(1 - F_i(x)) \tag{3.49}$$

3.5.8 Survival Analysis

In statistics, survival analysis is an area that investigates the expected time for one or more events to occur. For example, in medicine it is used to analyze the amount of patients that will survive after being infected with a disease after a certain time [78]. Survival analysis has several names depending on the field of research. In engineering it is called reliability theory, and is used to study the lifetime of a particular item or component [78]. Survival analysis studies the probability distributions of the event times and how the rate of event, for instance component failure, depends on certain risk factors. Survival analysis of situations with binary outcomes, e.g. survive or die, the survival probability distribution is the complementary probability distribution of the hazard probability distribution. I.e. if the probability of surviving at time t is given as $S(t)$, then the hazard function $h(t)$, which gives the probability of dying at time t, can be found to be $h(t) = 1 - S(t)$.

3.5.8.1 Censored Data

When measuring the time it takes for an event to occur, one has a starting point and an end point at which the event occurs. The time to event is set as the time difference between these two points in time [78]. It is common to set the starting time at 0. Example, when a component is installed. Or a common zero time when all the individuals starts at the same time, e.g. when testing the effect of a sedative on several individuals at the same time [78]. When collecting data in survival analysis, one can face the possibilities of having incomplete data. This is a *censored observation*. E.g. if investigating the time to death for patients with a disease, then it could happen that one or more patients would still be alive at the end of the period. For these patients one would know that they were alive at that time, but that they would die at some point after the study. These kind of data are known as *right censored data*. *Left censored data* is when the actual event occurs before the investigation starts. For example, when investigating the tumor size of patients, it is not possible to detect the tumor when it is below a certain size and knowing when it started to exist is unknown [78].

To summarize:

- Right censoring is when an event should occur at a value *higher* than the censoring value.
- Left censoring is when an event should occur at a value *lower* than the censoring value.

While exact data is when one knows the exact time the event occurs. Another type of missing data in survival analysis is called truncation. Truncation is similar to censoring, but has a selection bias in the sample, something censored data does not [78]. Truncation will not be explained more here, but can be read more about in the literature, for instance [78].

Chapter 4

Experimental Setup and Test Procedures

The experiments were performed at ABB Corporate Research Center in Baden-Dättwil. In the following chapter the experimental setup and test method will be described in detail.

4.1 Test and Measuring Circuit

The experiments were performed in a pre-existing pressure vessel which could hold pressures up to 6 bar absolute. Figure 4.1 show the schematic overview of the test circuit inside the pressure vessel. The circuit was divided into compartments which all were filled with SF_6 at varying pressure for insulation. The test chamber was filled with either CO_2 or SF_6, depending on what the test of interest. The test chamber contained the test objects, the needle electrode and the surface setups, which will be explained in separate sections. The high voltage impulses were generated by a Van de Graaff generator, which will be explained in Section 4.1.1. The Van de Graaff generator charges capacitors which are switched on the test object through damping resistors, as shown in Figure 4.1.

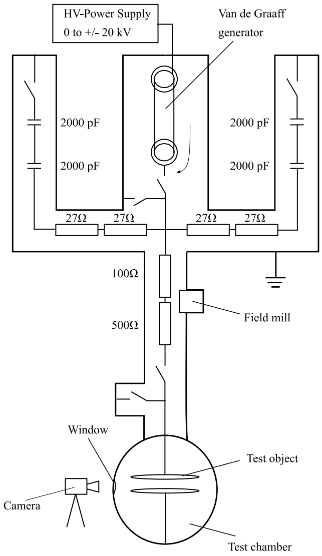

Figure 4.1: Schematic of the test circuit used. Full size schematic is shown in Figure A.1.

4.1.1 Van de Graaff Generator

The Van de Graaff generator that was used, was based on the design by Van de Graaff [79] with some modifications. The original design, illustrated in Figure 4.2a, of a Van de Graaf generator utilizes a belt of an insulating material which rotates over two rollers from a high voltage terminal to ground. This occurs inside an insulating column. When the band rotates a negative charge is created on the lower roller, due to the material (rubber), and through induction the outside of the belt holds a positive charge. A brush at the top of the belt, moves the positive charge of the belt to the outside of the spherical electrode know as the *collector*, while the brush at the bottom moves the negative charges to ground. At any given time the potential of the terminal is $V = Q/C$, where Q is the charge stored and C is the capacitance between the terminal and ground [80]. The modified Van de Graaff used for these experiments, illustrated in Figure 4.2b. The main difference was that the modified version had knives placed millimeters away from the rubber band instead of brushes. The upper knife, corresponding to the lower brush in Figure 4.2a, was given high voltage of either negative or positive polarity. This allowed negative or positive charge to be *sprayed* onto the belt, where it was moved to the collector and *scraped* off due to charge imbalance. The terminal of the Van de Graaff generator was then connected to a capacitor.

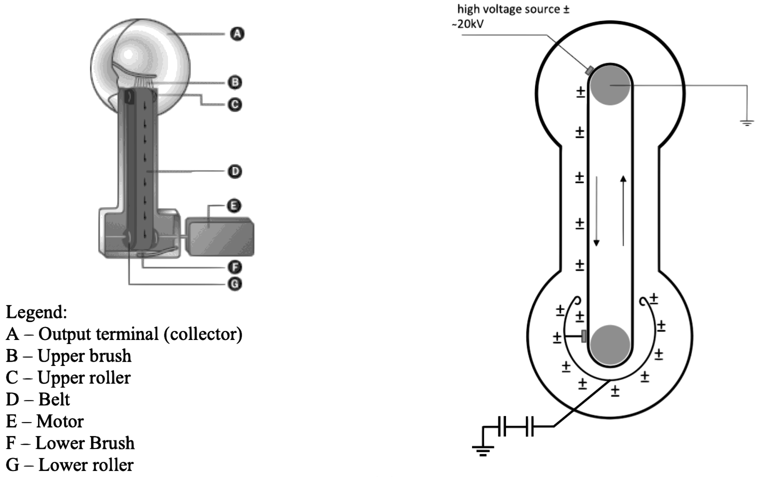

(a) Schematics of a traditional Van de Graaff generator [80].

(b) Schematic of the modified Van de Graaff generator that was used. Up side down in comparison to the original concept in Figure 4.2a

Figure 4.2

4.1.2 Electrode Gap

The voltage generated by the Van de Graaf generator was applied to the smooth plate electrode, while the needle electrode or the rough surface was connected to ground. The gap was initially set at 1.5 cm, but was later changed to 1.0 cm due to voltage limitations of the Van de Graaf generator.

4.2 Needle Electrode

The needle electrode, Figure 4.3, was designed as a steel plate electrode with a diameter of 20 cm. The edges of the electrode was curved with a radius of 2 cm. In the center of the electrode there was 400 identical holes placed in a 20 × 20 grid, see Figure 4.4. Each hole had a diameter of 1.1 mm with center to center spacing of two adjacent holes was 2 mm. Figure 4.5 show a close up image of 100 needles placed in the needle electrode. Inside the electrode was a motor, Section 4.2.1, which was connected to a magnet with a matching grid of the electrode to place the needles.

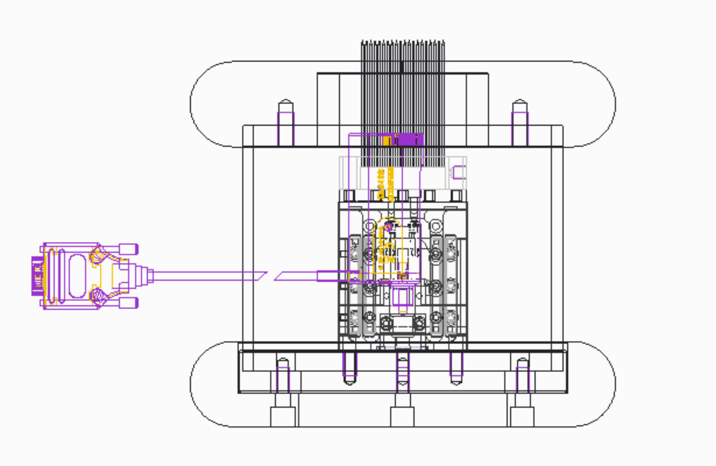

Figure 4.3: Schematic drawing of the needle electrode.

4.2.1 Motor

The motor used inside the electrode was a ZFS13B compact stepper motor actuator with 13 mm travel produced by Thorlabs Inc. with a homing[1] accuracy of less than 5 μm. The motor was controlled from outside the pressure vessel by a KST101 stepper motor controller also produced by Thorlabs Inc. The combination between the motor and the controller had a theoretical travel distance per step of 0.46 nm [81].

4.2.2 The Needles

The needles were made out of steel, 6 cm long, with a diameter of 1 mm and a conical tip of height 1.6 - 1.7 mm with a spherical tip that had a radius of 30 μm. The needles were

---

[1] Zero position of the motor.

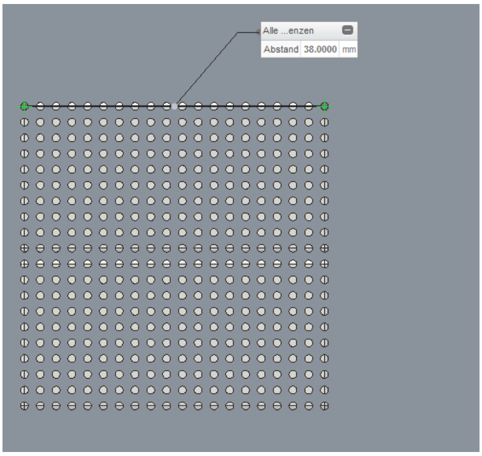

Figure 4.4: Top view of the design of the holes of the needle electrode.

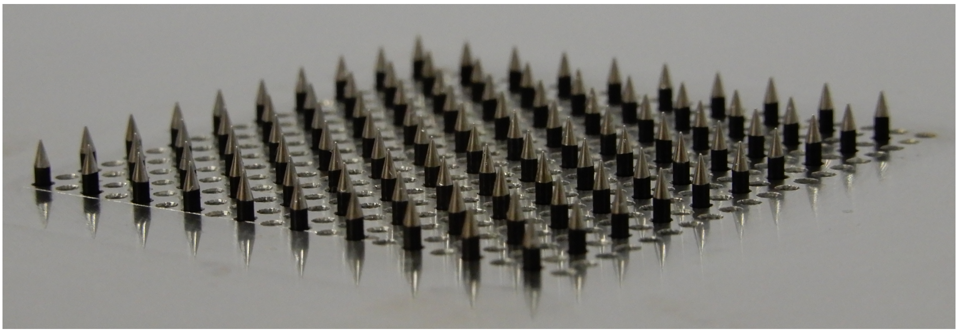

Figure 4.5: Close up of 100 needles in the electrode.

custom ordered from Ogura jewel industry co. ltd in Tokyo, Japan. Due to erosion of the needles, they were replaced each time the electrodes was removed from the vessel.

4.3 Determining Needle Lengths

4.3.1 Determining Needle Length With Single Needle

The length of a single needle was determined with the controller and live view of the camera. Initially, the motor was moved to its' zero position (homing), then it was moved with slow speed until it became barely visible. The needle was then retracted until it just barely disappeared, and this was noted as the zero position of the needle. The wanted needle length was moved to the wanted needle length from this position. The accuracy of this method will be discussed in Section 6.12.2 and for this is in the range of 10-20 μm.

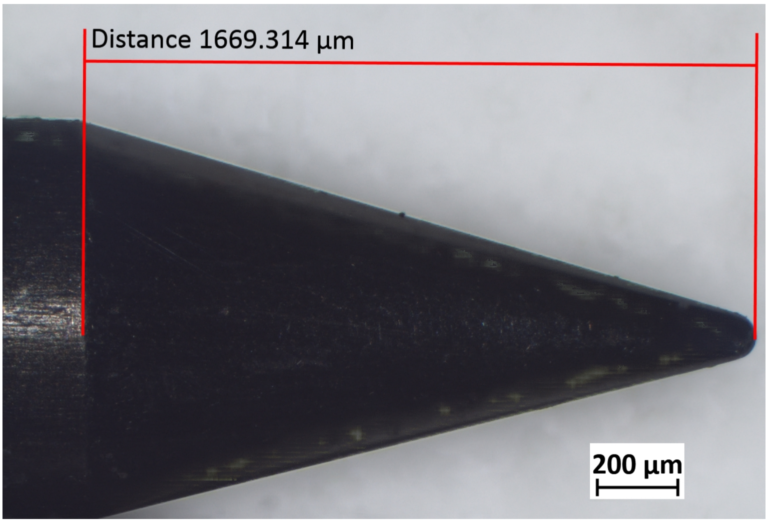

Figure 4.6: Close up picture of a needle

4.3.2 Determining Needle Length With Multiple Needles

When multiple needles were used it was observed that the needles were not of equal length. A method to set an average zero point was implemented. The electrode gap was watched through the window with the camera. The needles was moved until the first needle was visible which the distance of the stepper motor was noted. Then the needles was moved until the last needle was visible. The average of the first and last needle was then used as the estimated zero position of the needles. From this position the wanted length was added to the zero position and the needles was moved to this length.

To get an idea of how close this method was to the actual average. With 20 needles, the zero position of each needle was measured and the actual average and the estimated average was then calculated. The actual average zero position of the needles was found to be at 3.8113 mm and the estimated average zero position using the distance of the first and last visible needle was at 3.8193 mm. Figure 4.7 show the difference of each needle in the 20 needle setup from the estimated average zero position.

Due to the needles being of different length, there was an additional uncertainty to the needle lengths compared to the single needles. This will be discussed in Section 6.12.2, but the uncertainty of the multiple needles were in the range +/- 0.1 mm.

4.4 Test Voltages

The voltages applied by the Van de Graaff generator were closer to fast rising step voltage impulses, compared to a lightning impulse voltages. Figure 4.8 shows the conceptual difference, where the DC pulse stays at a constant voltage, and does not decrease which

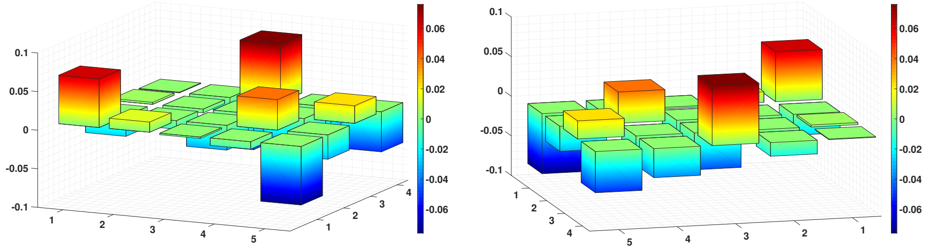

(a) Front **(b)** Behind

Figure 4.7: 3-D box plots of the difference of the needles from the estimated average zero position.

the standard lightning impulse does. The results were evaluated as equivalent to lightning impulse voltages, by only considering the breakdowns occurring between the voltage pulse reached peak voltage at approximately 0.2-0.25 μs and 10 μs. After 10 μs breakdowns were considered holds, with the assumption that they would not cause breakdowns if standard 1.2/50 μs lightning impulse were applied. Based on private communication, ABB has seen good agreement between this method and applied IEC standard lightning impulse voltage wave shapes. The *late breakdowns*, after 10 μs were recorded so they could be evaluated for DC breakdown levels.

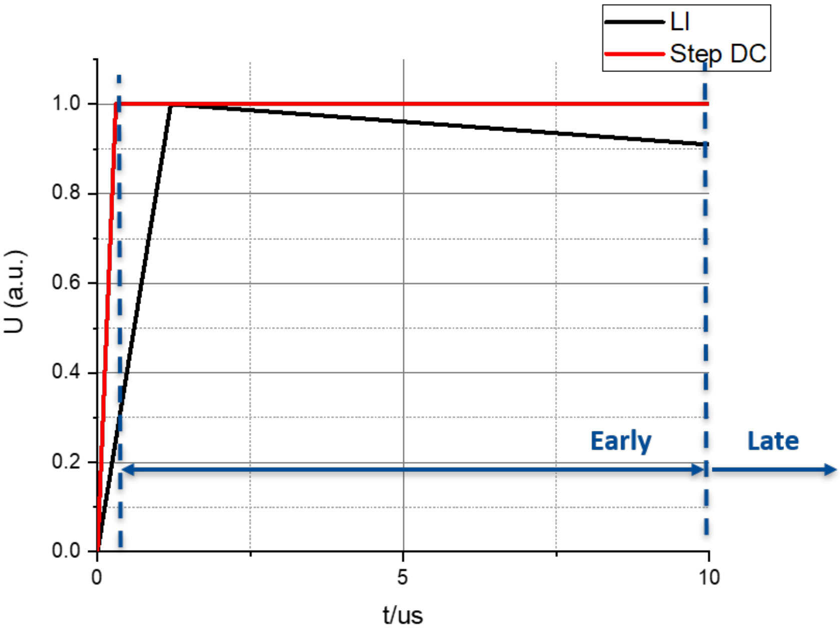

Figure 4.8: Conceptual illustration of the applied test voltage.

Figure 4.9 shows examples of an applied voltages divided by the peak voltage for a single, 20 and 100 needles. As can be seen there was a slight reduction after the peak of the voltage shape for the single needle. This was due to the bandwidth of the measuring system and possible due to partial discharges in the gap.

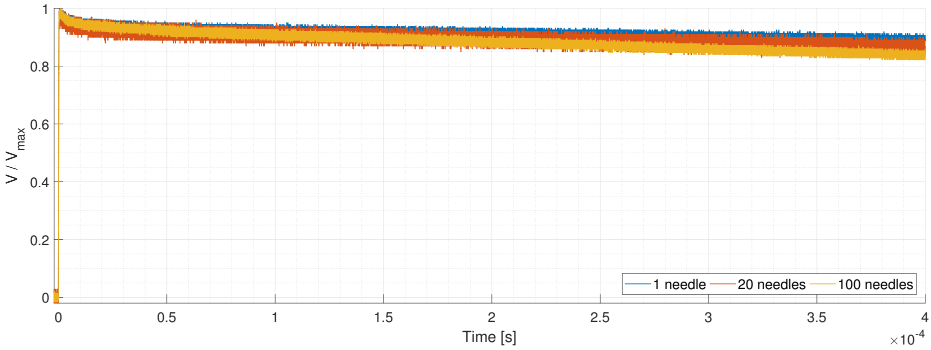

Figure 4.9: Example of scope readings of applied voltage pulse from the Van de Graaff generator with 1, 20 and 100 needles. Presented as applied voltage divided by max voltage for comparison.

One main reason to only evaluate early breakdowns was seen, Figure 4.8, when multiple protrusions were used. The applied voltage would drop down due to partial discharges. Considering all breakdowns for single needle and multiple needles would not give equivalent grounds for comparison. As the single needle would be applied a much more constant DC voltage compared to the multiple protrusions. The voltages applied to the 20 and 100 needles had a decrease due to partial discharges. The decrease continued until the extinction voltage was reached. Figure 4.8 only show the first 400 μs, the difference between the single voltage impulse and the 20 and 100 continued to increase after this time frame. However, for the first 10 μs, there was no different behavior of the applied voltages of the single needle or the multiple needles.

4.5 Voltage Application

The applied voltages were determined with an automate software, picking voltages at random. The mean value and a voltage range was set and the software applied random voltages within the $mean\,value - range$ and $mean\,value + range$ to the test objects. The voltages were applied for a maximum of 30 seconds[2]. After the procedure of saving the information of a breakdown or hold, which took 2-3 seconds from the event was determined. A 10-12 seconds break before charging of the Van de Graaff generator started, which usually lasted for 15-20 seconds. Giving the gap a pause of approximately 30 seconds between each applied voltage impulse. This short pause was countered with the application of a bias voltage of 20 kV for 2 seconds to suck away potential ions in the electrode gap.

---

[2] This was for most tests reduced to 15 seconds.

To get a good estimate of the mean value, close to the actual $50 - \%$ breakdown voltage, either the up and down method with 4-5 breakdowns or theoretical predictions from previous experimental results were used. In some experiments a larger voltage range was applied to determine the breakdown region where a new mean value would be estimated within the region with a smaller voltage range.

4.6 Diagnostics

4.6.1 Oscilloscope and Voltage Divider

The applied voltage was measured through a voltage divider with a LeCroy WavePro 960 Digital Oscilloscope with a bandwidth of 2 GHz and a maximum sample rate of 16 GS/s.

There was no schematics of the voltage divider, so the ratio between the applied voltage and measured voltage over the voltage divider was determined empirically to be 2.91.

4.6.2 Camera and Photographs

To document whether or not a breakdown occurred at the needle(s) a Nikon D9000 with a Sigma 105mm F2.8 EX DG Macro lens from Sigma was used. The camera was automated by the same software controlling the voltage to take a picture for each voltage application. The shutter speed was set to last longer than the applied voltage of 15-30 seconds. The ISO of the camera was set to the camera minimum of 100.

If a breakdown occurred and it was not at the needle(s), the result was discarded from evaluation. Thus, all tests where a majority of the breakdowns occurred at the needle were *sorted* to only include holds and needle breakdowns. If a test series had too many breakdowns that were not at the needle(s), the series was analyzed *unsorted*.

4.7 Experimental Limitations

The experimental work in this thesis were limited to a maximum absolute pressure of 6 bar. The other limitation was the maximum charging voltage of the Van de Graaff generator, which could not reach higher voltages than roughly 400 kV. This limited the gap size that could be used in SF_6.

4.8 Streamer inception calculations in CO_2 and SF_6

For streamer inception calculations, the electric field values were simulated in COMSOL multiphysics, shown in Figure 4.10. In the model, the needle and hole was created as an axi-symetric model, where the radius of the needle was 0.5 mm, radius of the needle tip was 30 μm, radius of the hole was set to 0.55 mm. The edge of the hole was added a small curvature as the holes did not have a perfect sharp corner. The curvature was kept small to keep things as close to the *worst case* scenario. The model shown in Figure 4.10 was simulated with the mesh manually set finer than the preset extremely fine for the different relevant needle lengths in the range 0.05 to 2 mm. For comparison, the needle was simulated without the hole to see if there was an impact of the hole and its edge. Figure 4.11 show the maximum field strength on the needle was for the simulations with holes compared without holes. One can see that the hole has an impact of the maximum field strength at the needle lengths below 0.3-0.2 mm. Figure 4.12 compares the electric field strength along the axi-symmetry line of the COMSOL model. Figure 4.12a show that there is a significant difference due to the hole with a needle of 0.05 mm. While at the needle length of 0.5 mm there is barely any difference of the field along the symmetry line as shown in Figure 4.12b. The increase of the field strength before the peak was due to the maximum field strength of the needle was slightly to the right of the axi-symmtery line in the COMOSOL simulation, which was also why the maximum field shown in Figure 4.11 was higher than the one shown in Figure 4.12. Due to the impact of the holes, the electric field simulations with holes were used for calculations of the streamer inception criterion.

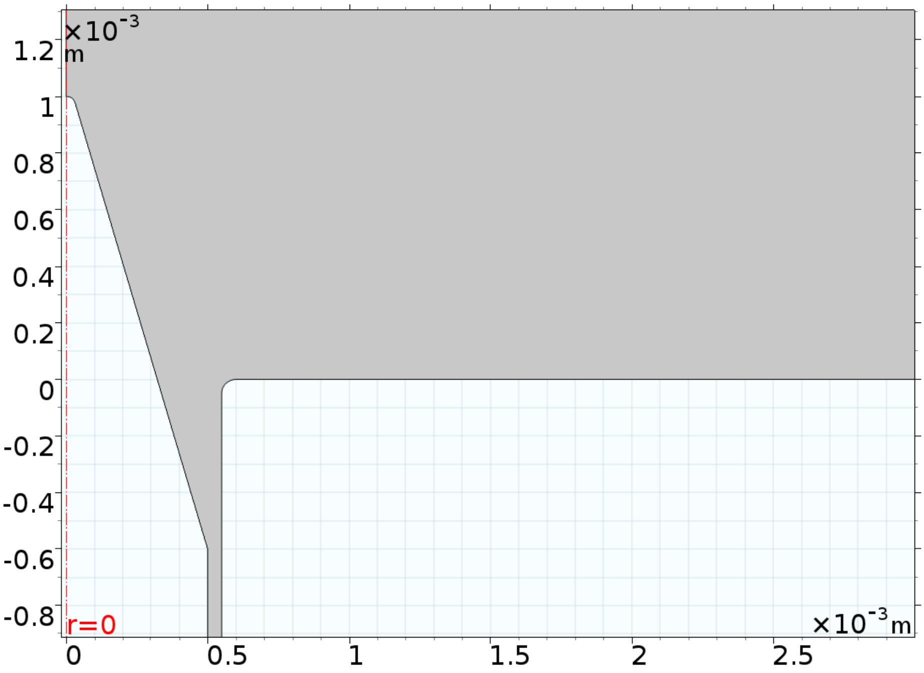

Figure 4.10: Single needle model with hole used in the COMSOL simulations. Showing needle length at 1 mm.

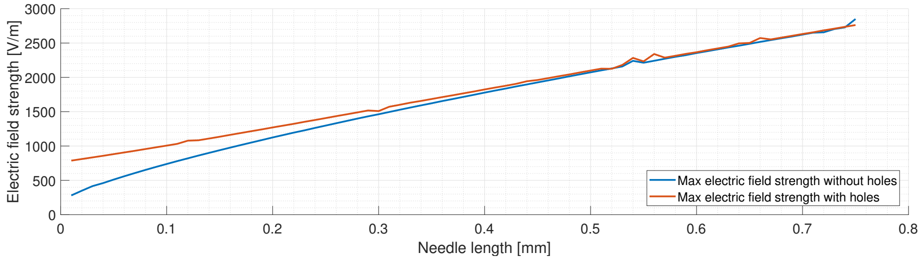

Figure 4.11: Comparison of the maximum field of the simulated needle with hole, with the case of needle without hole. The *unevenness* of the curves are due to the mesh being too large, even while set manually lower than the preset *extremely fine* in COMSOL.

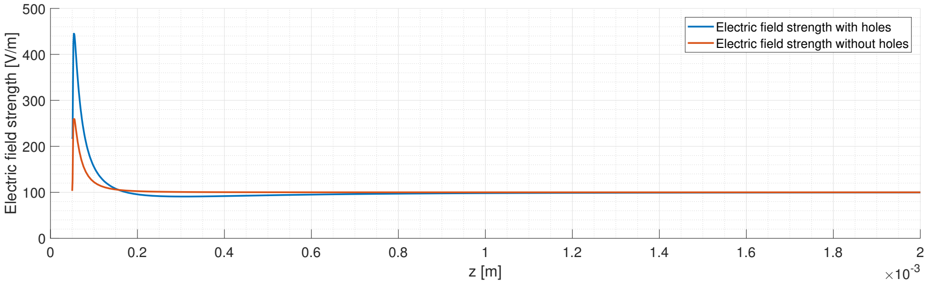

(a) 0.05 mm needle

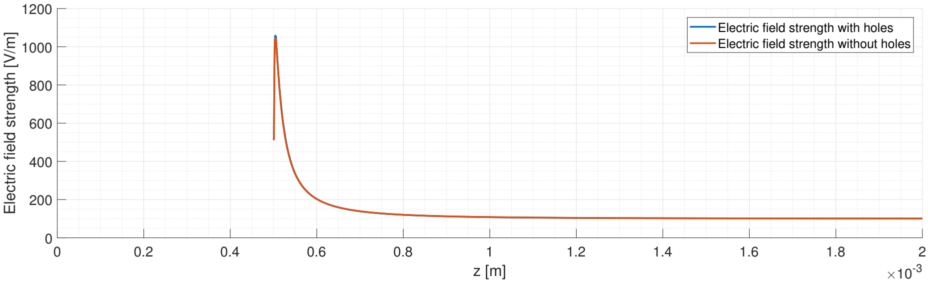

(b) 0.5 mm needle

Figure 4.12: Electric field along the axi-symmetry line.

4.8.1 Streamer Inception Calculations in CO_2

Calculation of the theoretical streamer inception criterion in Equation 3.17 were performed with the constant $K = 10$. The effective ionization coefficient was found in CO_2 from the function given in Equation 4.1.

$$\alpha_{eff} = 2.4e^{-22} \cdot e^{-\frac{370}{E/N}} \cdot \left(\frac{E}{N}\right)^{0.7} \tag{4.1}$$

In Equation 4.1, $E/N \gtrapprox 88$ Td[3] is the reduced electric field. Equation 4.1 is a fitted curve to Phelps' compilation of electron cross sections for CO_2 [82; 40].

4.8.2 Streamer Inception Calculations in SF_6

Calculating the theoretical streamer inception criterion given in Equation 3.17 in SF_6, α_{eff} was determined from Equation 3.19. With the constant in Equation 3.17 $K = 10.5$.

4.9 Rough Surface Electrodes

To have two different areas for testing two plugs and a Rogowski electrode were designed. The two plugs were designed with a so-called bi-radial curvature according to the schematic drawing in Figure 4.13 The length of the plugs were 1 cm.

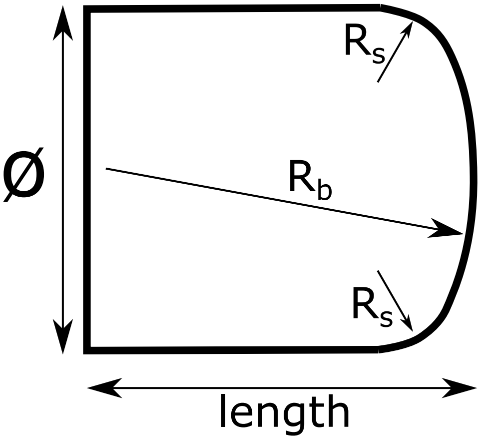

Figure 4.13: Schematic design of the bi-radial plugs. The designed plugs had $\varnothing = 1.9$ cm, $R_s = 0.5$ cm, $R_b = 2$ cm and a length of 1 cm

The Rogowski shape was created to have a quasi-uniform field without field enhancement at the edges [83]. The design was made according to Equation 4.2 [4] with a radius r of 6 cm. The shape is plotted in Figure 4.14.

$$z(r) = \frac{0.02}{\pi} \cdot \left(\frac{\pi}{2} + e^{(r-0.05)\cdot \frac{\pi}{0.02}} \right) \tag{4.2}$$

The electrodes were made out of stainless steel and were sandblasted with *SABLUX EKF 0014 Edelkorund Weiss* grains of the size 1190 to 1600 μm with a pressure of 7.5 bar to

---

[3] Td is the unit Townsend and is $1 \text{ Td} = 10^{-21}$ V m^2 [82]

[4] The r-0.05 is to shift the 0 position of the curve to the center of the electrode.

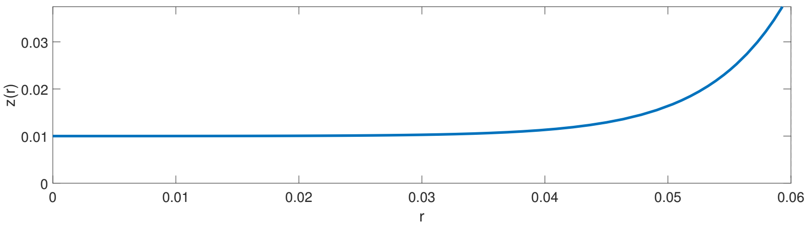

Figure 4.14: The axi-symmetric profile shape of the Rogowski electrode

generate rough surfaces. The plugs are shown in Figure 4.15, showing Plug A to the left after use where one can easily see the breakdown marks.

Figure 4.15: The actual plugs used, Plug A to the left after use and Plug B before use to the right.

4.9.1 Surface Measurements

To determine the surface parameters of the Rogowski and the plugs, they were scanned with a non-contacting 3D profilometer system called Hyperion Compact from OPM with a resolution of 20 nm [84].

The obtained values for the plugs and the Rogowski electrode are presented in Table 4.1 and the isometric plots of the scans of the plugs A and B are presented in Figure 4.16. There was a variation of the R_a, but the $R_{z,\text{ ISO}}$ gives an indication of the relationship of the largest peaks and the deepest vallys of the surface. Since R_z was fairly consistent of the three measured surfaces, the surface roughness were assumed to be approximately similar.

Table 4.1: Surface parameters from surface scans.

Parameter	R_a [μm]	R_z[μm]
Rogowski	7.33	65.8
Plug A	4.16	61.5
Plug B	5.06	65.1

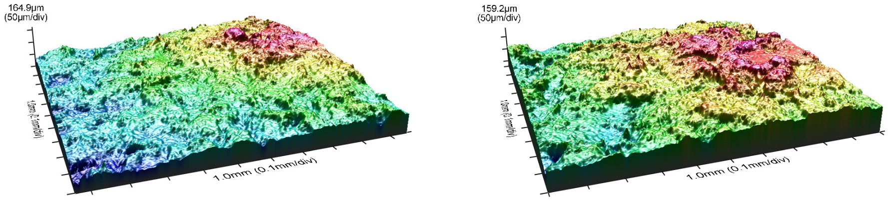

(a) Plug A

(b) Plug B

Figure 4.16: 1x1 mm isometric plots of the surface scans, unadjusted for curvature.

4.9.2 Determining the Effective Area

The effective area of the electrodes were determined by first determining the distance from the center of the electrode to the outermost breakdown after the tests. Then the area was found by surface integrating for the plugs and the Rogowski. The active area of the Rogowski was found to be 64.465 cm^2. The area of the plugs were approximately identical, thus they were given the same active area of 2.383 cm^2.

4.9.3 Field Calculations of the Plugs

The plug electrodes were simulated in COMSOL without surface roughness to determine the electric field strength of the surface along the electrode. From the electric field strength of the surface the field enhancement was found. Figure 4.18, shows the resulting field calculation of the axi-symetric plug geometry.

After the tests, the simulation was used to calculate the weighted average field enhancement of the plugs. Using the maximum distance of a breakdown from the symmetry axis, r = 0.85 cm. The weighted average field enhancement was 1.4018, which the plug results were multiplied with before evaluation of the 50 % average breakdown field.

The error of the simulation, *the maximum value* - *the weighted average* was included in the error bars of the plug results through error propagation:

$$\epsilon = \sqrt{\left(\frac{\sigma}{U_{50}}\right)^2 + \left(\frac{Max\,field\,strength - Weighted\,average\,field\,strength}{Weighted\,average\,fieldstrength}\right)^2} \tag{4.3}$$

4.10 Cleaning of the Needle and Smooth Electrodes

Each time the pressure vessel encapsulating the electrodes was opened. The electrodes were removed and cleaned before they were put back into the vessel, the vessel was also

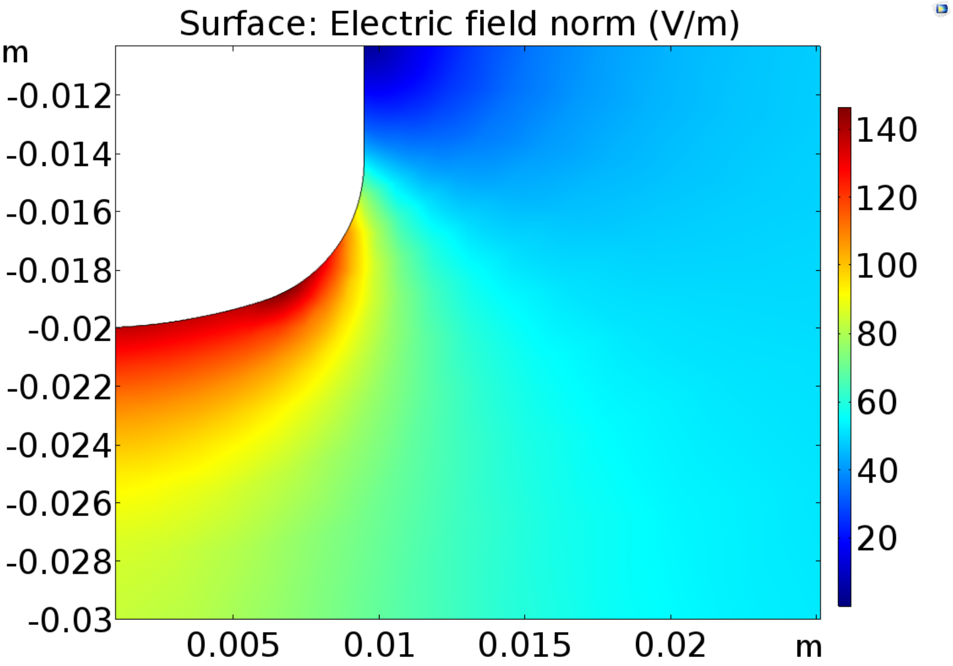

Figure 4.17: Axi-symmetric field enhancement and shape of the plug, when the plug was applied 1 V potential and a gap distance from the tip of the plug to the plate of 1 cm.

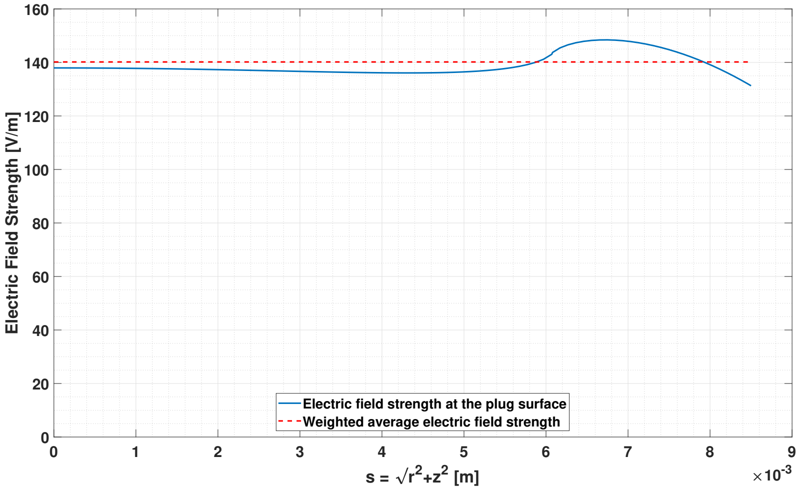

Figure 4.18: Electric field calculations of the surface roughness with the curvature distance $s = \sqrt{r^2 + z^2}$ from the axi-symmetrical line.

cleaned with a vacuum cleaner. This was done to remove the impact of surface conditioning on the plate electrodes and to remove dust from the vessel and the electrodes.

Initially, the (smooth) electrodes were polished with Metarex® polishing cloth. Then the electrodes were cleaned with pure ethanol and Kimberly-Clark™ Professional Kimtech Science™ Kimwipes™ Delicate Task Wipers, 1-Ply wipes. However, it was observed in the photographs that there was a lot of dust on the electrodes. To reduce the amount of dust, the cleaning method was changed. Instead of ethanol, isopropanol was used since it has a lower surface tension than ethanol, which allows it to evaporate faster, making it more difficult for dust to stick to the electrodes outside the vessel. The wipes was changed to special nanofabric cleanroom wipes: Contec Amplitude™ Sigma™ which are designed to not leave fibres behind when used. This change in the post polish cleaning procedure reduced the amount of dust on the electrodes during the experiments.

4.11 Curve Fitting and Confidence Bands

4.11.1 Fitting the Normal Distribution Using Probit

To fit the results with the normal distribution the results of each shot was considered binary where a shot was either a *breakdown* $= 1$ or a *hold* $= 0$. To do this the method known as *Probit* was used [85]. The probit method allows the binary data Y to be transformed into the continuous estimate Y' between 0 and 1. For this thesis, it means that based on the binary results of either a breakdown or hold, the probit gives a probability for a breakdown occurring based on the applied voltage.

$$\Phi^{-1}(\pi) = \beta_1 + \beta_2 x \tag{4.4}$$

Where π represents probabilities, and Φ^{-1} is the link function and is the inverse of the normal cumulative distribution function. This is the function that was fitted in Matlab with the statistics and machine learning toolbox function *glmfit* [86] and evaluated with the function *glmval* [87] within a script created by Scientist Philipp Simka at ABB. The mean of the distribution is found from the fitted variables in Equation 4.4 from $\mu = -\beta_1/\beta_2$ and the standard deviation $\sigma = 1/\beta_2$ [85]. The built-in functions from Matlab also returns the 95 $\%$ confidence bands of the fit.

4.11.2 Determining the Empirical Cumulative Distribution Function From the Turnbull Algorithm

To determine the empirical cumulative distribution function (ECDF) of the experimental results so a distribution function could be fitted. An iterative procedure to estimate the survival function, *S(X)*, of doubly censored data was used. From the survival function the failure function *F(X)* was determined from the relationship $F(x) = 1 - S(x)$. The algorithm is know as *Turnbull's nonparametric estimator* and was proposed by Bruce W. Turnbull in 1974 [88]. The algorithm was initially proposed to determine the distribution of the time for an event to occur when faced with censored data. This algorithm has been implemented and illustrated by Suely R. Giolo [89]. Giolo used the algorithm to estimate life of patients with limited information about the exact time of death. For this thesis, the procedure was adapted to increasing voltages, instead of time, and was based on a Matlab software and script by ABB's Senior Principal Scientist Kai Hencken.

Assuming each experimental shot of voltage impulses as independent situations, the exact voltage that should be applied to cause a breakdown was unknown at any instant. If a voltage was applied and it resulted in a hold, the exact breakdown voltage, the voltage that would have given a breakdown at that moment of time was higher than the applied voltage. If the application of the voltage caused a breakdown, the exact breakdown voltage was lower or equal to the applied voltage.

This allowed the applied voltages that resulted in a hold, non-breakdown, were considered as right censored data. Applied voltages that resulted in breakdowns were then considered as left censored data (as explained in section 3.5.8.1), while the exact voltage that would have given a breakdown remained unknown. The method and algorithm, based on Giolo's version, will be explained in steps below.

Determining Intervals and Creating Alpha

Let $0 = x_0 < x_1 < x_2 < x_j < \cdots < x_m$ be a sorted grid of the unique voltages that include all the observed voltages X_i for $i = 1, ..., n$, where *n* is the number of total recorded voltages and *m* is the number of unique voltages. For the *i*-th observation define a weight α_{ij} to be 1 if the voltage interval $(L_i, U_i]$ contains the voltage X_i, where L_i is the lower limit of the interval and U_i is the upper limit of the interval. α is a matrix with the dimension $[n \times m]$. The weight, α_{ij} indicates that the exact breakdown voltage at the applied voltage X_i could have been at the voltages x_j where $\alpha_{ij} = 1$.

Determining the Weight α_{ij} for Censored Data

For the random test method all data was considered to be censored, since the exact breakdown voltage was considered to be unknown. For left censored (breakdowns) data the lower limit L_i was set to zero as it was assumed that no breakdowns could occur at zero voltage, the upper limit was set to the the recorded voltage. This indicates that the actual breakdown voltage at the voltage X_i was in the interval $(0, X_i]$. Thus, all α_{ij} corresponding to this was set to 1. For right censored values (holds) the exact breakdown voltage was assumed to be higher than the recorded voltage X_i and should lie in the interval (X_i, ∞), which all corresponding α_{ij} was set to 1.

The Turnbull Algorithm

1. Make an initial guess for $S(x_j)$. From either the Kaplan-Meier estimator (see step 5) or simply by taking $1/(n+1)$.
2. Compute the probability p_j of an event happening at the voltage x_j from
$$p_j = S(x_{j-1}) - S(x_j) \qquad j = 1, \dots, m \tag{4.5}$$
3. Estimate the number of events d_j that occurred at x_j from
$$d_j = \sum_{i=1}^{n} \frac{\alpha_{ij} p_j}{\sum_{k=1}^{m} \alpha_{ij} p_k} \qquad j = 1, \dots, m \tag{4.6}$$
4. Compute the estimated number at risk at x_j, Y_j from
$$Y_j = \sum_{k=j}^{m} d_k \qquad j = 1, ..., m \tag{4.7}$$
5. Compute the new estimate for $S(x_j)$ from the values of step 3 and 4 with the product limit estimator (the Kaplan-Meier estimator)
$$S(x_j) = \prod_{i=1}^{m} \left(1 - \frac{d_i}{Y_i}\right) \qquad j = 1, \dots, m \tag{4.8}$$
6. End the algorithm when it reaches a self-consistency where the updated version of S is close to the previous version at a predefined limit
$$max|S(x_j)_{old} - S(x_j)_{new}| < 1 \cdot 10^{-5} \tag{4.9}$$
Otherwise repeat steps 2 through 5 with the new estimates for S_{new} as the new guessed estimate.

The survival function gives the probability of a hold at a given voltage. Since holds and breakdowns can be considered complementary events, the empirical cumulative distribution function can then be determined by $F = 1 - S$. The code for the algorithm will not be given as it is property of ABB.

4.11.3 Fitting Three Parameter Weibull

After the Turnbull algorithm had been calculated for the test, the results were fitted with the three parameter Weibull distribution. The results were fitted in Matlab with the built in *fit* function fitting Equation 3.29 with the Nonlinear-Least-Square-Error (NLSE). NLSE minimizes the square error of a function of m observations to n, where $m > n$, and is used to fit non-linear functions to data [90]. For the results in this thesis, the zero-position parameter of Equation 3.29, x_u, was set to be equal the streamer inception electric field strengths which were calculated as explained in Section 4.8. Due to the assumption that breakdowns cannot occur at electric field strengths lower than the field strengths required for streamer inceptions.

4.11.4 Determining the 95 % - Quantile From Bootstrapping

In statistics Bootstrapping is a method to determine the accuracy of the given results of sample estimates [91; 92]. Given a sample of size *n* of the voltages $X_1, X_2,...,X_n$ with the cumulative distribution function *F(X)*, *F(X)* being the ECDF calculated from the Turnbull-algorithm explained in Section 4.11.2. The idea of the bootstrap method is to create *N* new samples of size *n* by randomly re-sampling with replacement from *F(X)*. Then the statistic of interest is calculated for each new sample. Re-sampling with replacement means that the same value can be selected more than once in the same generated sample.

In this case, *N* new sample experiments were created. Then the wanted distribution function, the three parameter Weibull distribution was fitted, according to Section 4.11.3, to each of the *N* new samples of the experiment. The confidence bands were then found from determining the *2.5* and *97.5* quantiles of the fitted Bootstrap samples. This method is known as the *bootstrap percentile method* [92]. In this thesis, the number of re-samples *N* was set to be equal to 1000. The higher number of re-samples the better [92] and 1000 might be in the lower range of what should be used, but it gave an indication of the precision of the results.

Chapter 5

Results

This section will present the results and give some initial comments, before everything will be discussed more in depth in Chapter 6. The results were obtained and evaluated as lightning impulse voltages as described in Chapter 4. Each result (point in a plot) was obtained with a minimum of 100 shots before sorting of non-needle breakdowns was applied. Each test was evaluated with the Turnbull algorithm (Section 4.11.2) and fitted with the three-parameter Weibull distribution (Section 3.5.4), where the zero point of the distribution was set to the streamer inception value, calculated for each needle length. The streamer inception evaluation was based on simulations of the geometry and needle lengths done in the Finite Element Method software COMSOL Multiphysics, and evaluated according to Equation 3.17.

Most plots will include one or more point labeled "*Dust breakdown*." If this point occurs at 0 mm needle length, this is obtained by retracting all the needles and testing a plate-plate setup. If the point occurs at a needle length greater than 0, the series had very few breakdowns at the actual needle, and the unsorted data set was used to evaluate the 50% breakdown electric field strength, see Section 4.6.2 for the definition of *sorted* and *unsorted* data.

Unless otherwise specified, All the electric field strengths, y-axis of the plots, refers to the uniform (average) background field of the setup determined from Equation 3.6.

The polarity given in the results will always refer to the polarity of the needle(s) or rough surfaces.

5.1 Single Needle SF_6

Figures 5.1 and 5.2 show the results for the E_{50} values plotted versus needle lengths for positive and negative polarity, respectively, of a single needle in SF_6. In the plots the standard deviation, σ, is given as errorbars for each point. The tests for single needle was performed for two gap lengths, 10 mm and 15 mm.

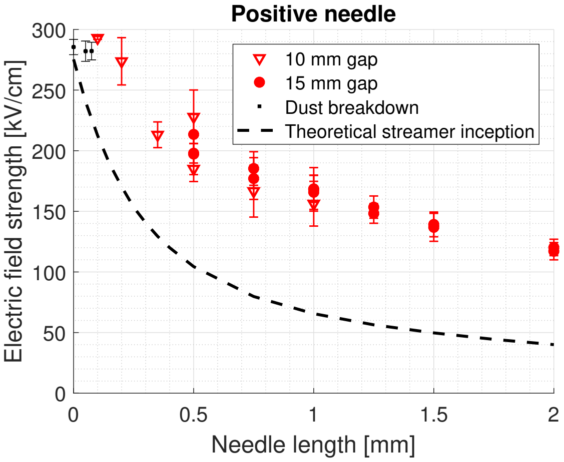

Figure 5.1: Experimental result of the E_{50} for a single positive needle in SF_6. The calculated standard deviation of each resulting distribution is given as error bars of each E_{50} value. The y-axis refers to the uniform (average) background field strength.

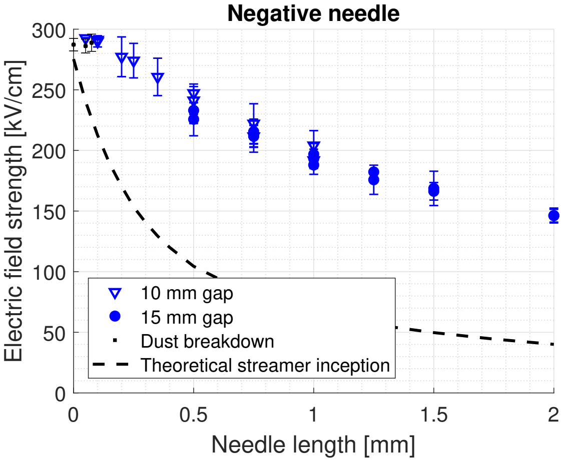

Figure 5.2: Experimental result of the E_{50} for a single positive needle in SF_6. The calculated standard deviation of each resulting distribution is given as error bars of each E_{50} value. The y-axis refers to the uniform (average) background field strength.

The results do not show any systematic change between the 10 and 15 mm gap distance in the 50 % uniform average background breakdown field strength for either polarity. Compared with each other, the E_{50} values for positive polarity of the needle were lower than the ones for negative polarity. The positive polarity had more scatter than negative polarity results. The tests at 0.05 and 0.1 mm for both polarities showed few breakdowns at the needle. The *unsorted* data set showed a E_{50} value similar to that without any needle present. This showed an insensitivity to a single needle protrusion at 0.05 and 0.1 mm compared to the dust.

5.2 20 Needles SF_6

Figures 5.3 and 5.4 show the results for the E_{50} values plotted versus needle lengths for positive and negative polarity, respectively, of 20 needles in SF_6. The needle lengths were determined as explained in Section 4.3.2. This gave an uncertainty on the x-axis for the needles length of +/- 0.1 mm, this was not plotted and will be discussed further in Section 6.12.2. For both polarities, the prediction based on the results from a single needle was also plotted as a dashed line. The prediction was calculated according to the enlargement law for each obtained result, as explained Section 3.5.7. Where there were more than one prediction from the single needle, the average prediction was calculated and used as the prediction point, while the error bars of the prediction line indicates the maximum and minimum prediction at that length. The results from a single needle was plotted for comparison.

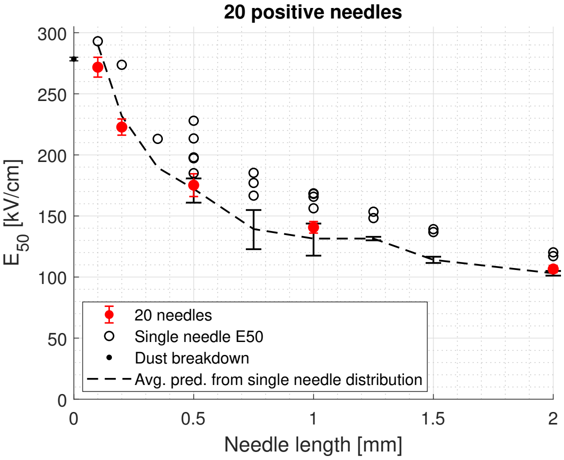

Figure 5.3: Experimental result of the E_{50} for 20 positive needles in SF_6. The calculated standard deviation of each resulting distribution is given as error bars of each E_{50} value.The black dashed line represent the prediction for20 needles based on the single needle distribution. The y-axis refers to the uniform (average) background field strength.

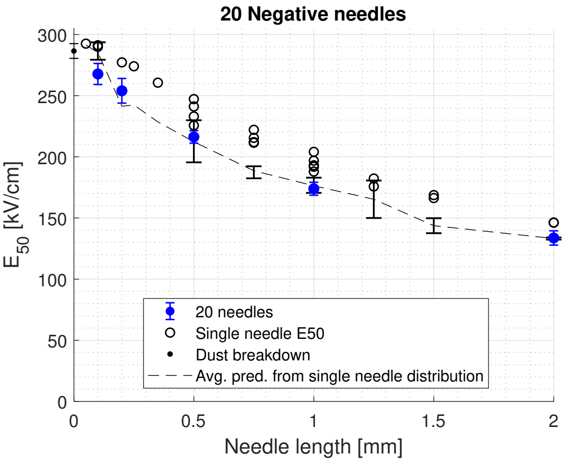

Figure 5.4: Experimental result of the E_{50} for 20 negative needles in SF_6. The calculated standard deviation of each resulting distribution is given as error bars of each E_{50} value.The black dashed line represent the prediction for 20 needles based on the single needle distribution. The y-axis refers to the uniform (average) background field strength.

The results showed a reduction of the E_{50} average background field strength when increasing to 20 needles. The results agreed well with the predictions for both polarities, confirming the enlargement law.

5.3 100 Needles SF_6

Figures 5.5 and 5.6 show the results for the E_{50} values plotted versus needle lengths for positive and negative polarity, respectively, of 100 needles in SF_6. The rest of the plot and the uncertainty were assumed to be the same as for the results with 20 needles, described in Section 5.2. The decision to investigate the effect of needle lengths longer than 1 mm was made after the 100 needle tests were performed. Due to time constraints, tests with 100 needles at lengths longer 1 mm were not performed.

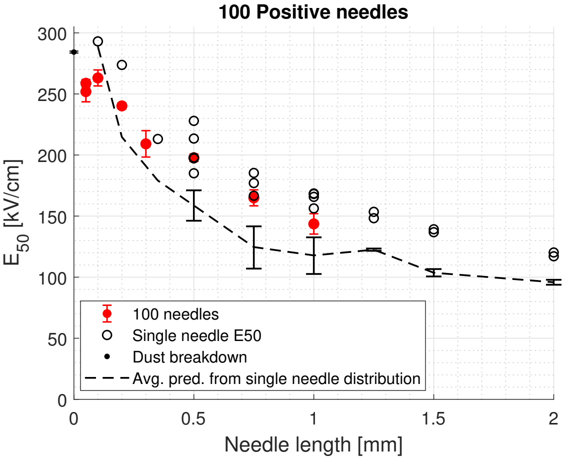

Figure 5.5: Experimental result of the E_{50} for 100 positive needles in SF_6. The calculated standard deviation of each resulting distribution is given as errorbars of each E_{50} value. The black dashed line represent the prediction for 100 needles based on the single needle distribution. The y-axis refers to the uniform (average) background field strength.

The results for 100 needles showed a reduction of the E_{50} average background field for both polarities. When compared with the predictions, there was a discrepancy between the obtained results and the predictions for positive polarity where the predictions were lower than the results. For negative polarity there was good agreement between the predictions and the results for needle lengths of 0.2 mm and above. Below 0.2 mm the predictions were higher than the results.

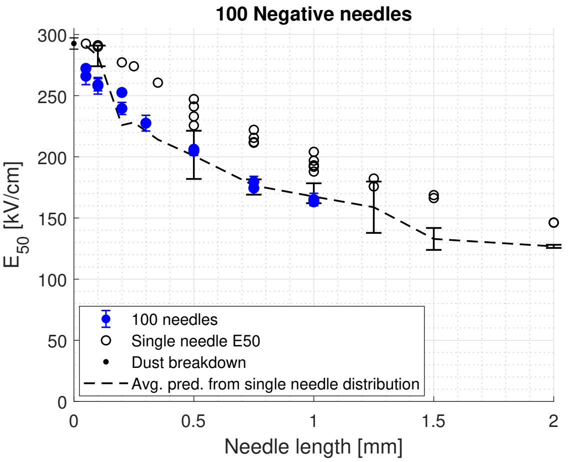

Figure 5.6: Experimental result of the E_{50} for 100 negative needles in SF_6. The calculated standard deviation of each resulting distribution is given as errorbars of each E_{50} value. The black dashed line represent the prediction for 100 needles based on the single needle distribution. The y-axis refers to the uniform (average) background field strength.

5.4 Single Needle CO_2

Figures 5.7 and 5.8 show the results for the E_{50} average background field values plotted versus needle lengths for positive and negative polarity, respectively, of a single needle in CO_2. In the plots the standard deviation, σ, was given as error bars for each result. The plots for the results in CO_2 also include a purple line indicating the streamer crossing field, taken from [40], for positive and negative polarity. For positive polarity the streamer crossing coincided with the critical field at the given pressure of 6 bar absolute, which was plotted as a solid black line in the negative plot (and the remainder plots as well).

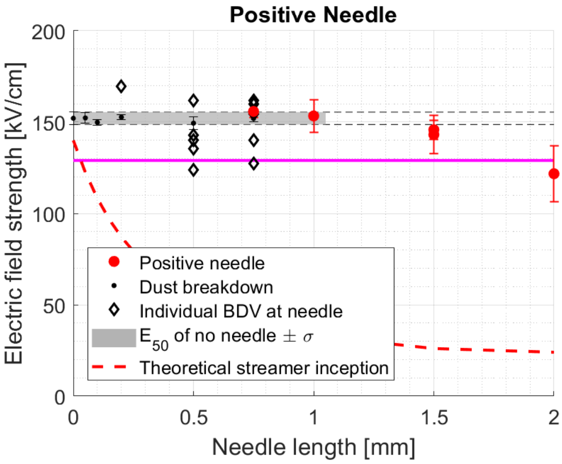

Figure 5.7: Experimental result of the E_{50} for a single positive needle in CO_2. The calculated standard deviation of each resulting distribution is given as error bars of each E_{50} value. The y-axis refers to the uniform (average) background field strength.

The results showed that CO_2 was not very sensitive to single needle protrusions of positive polarity at lengths shorter than 1 mm. At the short needle lengths, <0.5 mm, barely any breakdowns were observed at the needle from the photographs. It was only at needle lengths above 1 mm that the 50% average background breakdown field strength starts to decrease compared to the test without any needle protrusion. the $E_{50} \pm \sigma$ was shaded grey as an eye guide to show the region with no influence. At the needle lengths of 0.05 and 0.1 mm, no breakdown occurred at the needle. Individual breakdowns that happened at the needle for the 0.2, 0.5 and 0.75[1] mm needle lengths were plotted to give an indication of the fields where breakdowns occurred at the needle, showing a scatter around the test without a needle.

---

[1] The 0.75 mm needle length was tested twice where one did not give a sufficient data set, when filtered for needle breakdowns, to fit with a distribution

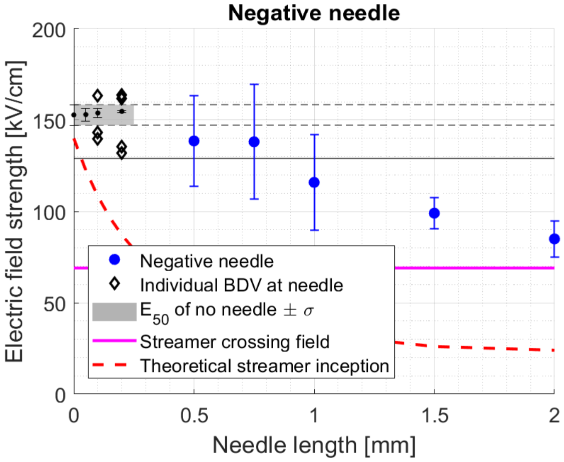

Figure 5.8: Experimental result of the E_{50} for a single negative needle in CO_2. The calculated standard deviation of each resulting distribution is given as error bars of each E_{50} value. The y-axis refers to the uniform (average) background field strength.

For the negative needle, the results showed that CO_2 was not very sensitive at the needle lengths shorter than 0.5 mm. Compared with positive polarity, the impact of the needle happens at a shorter needle lengths, around 0.5 mm (compared with 1 - 1.5 mm for positive polarity). The results also showed that the 50% average background breakdown field was lower for negative polarity than for positive polarity.

5.5 20 Needles CO_2

Figures 5.9 and 5.10 show the results for the E_{50} values plotted versus needle lengths for positive and negative polarity, respectively, of 20 needles in CO_2. The plots includes the prediction based on the enlargement law from the single needle results. The error bars of the prediction line was where more than one result was obtained with a single needle. To test if there was a shielding effect, explained in Section 3.2.2, the 20 needle setup was tested with both 2 mm, the minimum possible spacing between needles with the electrode, and 4 mm spacing (labeled normal space) between needles.

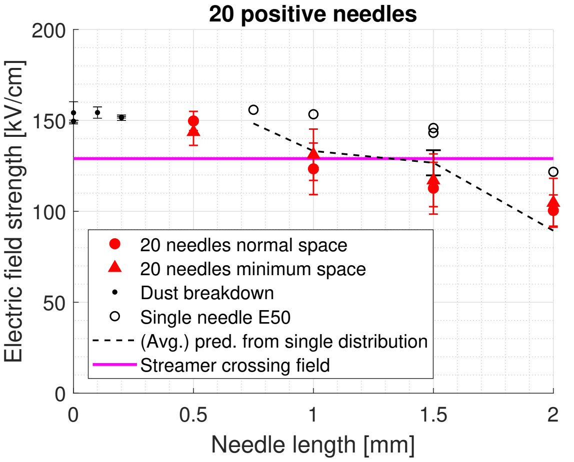

Figure 5.9: Experimental result of the E_{50} for 20 positive needles in CO_2. The calculated standard deviation of each resulting distribution is given as error bars of each E_{50} value. The black dashed line represent the prediction for 20 needles based on the single needle distribution. The y-axis refers to the uniform (average) background field strength.

The results for 20 needles at positive polarity showed a decrease from the results obtained with a single needle in CO_2. The predictions showed good agreement with the obtained results. For 20 needles, breakdowns occurred more frequently at the needles compared to the single needle results. This made it possible to obtain values down to needle lengths of 0.5 mm. The results at 0.5 mm needle lengths, showed a 50% average background breakdown field strength above the critical field. Comparing the results of the two spacings of the needles showed, for all tested needle lengths, results within the standard deviation of the two setups. However, for all needle lengths except 0.5 mm, the results for minimum spacing was slightly higher than the normal spacing of 4 mm.

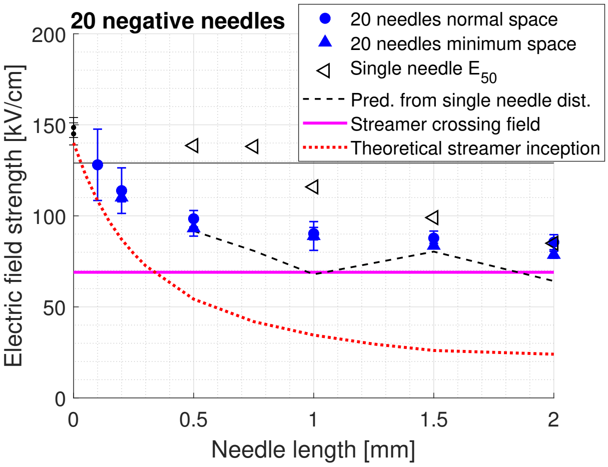

Figure 5.10: Experimental result of the E_{50} for 20 negative needles in CO_2. The calculated standard deviation of each resulting distribution is given as error bars of each E_{50} value. The black dashed line represent the prediction for 20 needles based on the single needle distribution. The y-axis refers to the uniform (average) background field strength.

The results for 20 negative needles showed a more drastic change compared with positive polarity, where the 50% average background breakdown electric field strength quickly drops down to a value of 85 - 90 kV/cm, above the streamer crossing field strength and remained there for increasing needle lengths. This was within reasonable agreement with the prediction. The results showed a higher sensitivity to the needle protrusions at negative polarity where the 50% average background breakdown field strength was reduced at 0.1 mm, which it did not do for positive polarity. Changing the spacing of the needles gave results within the standard deviation of each other. However, in contrast to positive polarity all the results for the minimal spacing was slightly below those for normal spacing.

5.6 100 Needles CO_2

Figures 5.9 and 5.10 show the results for the E_{50} values plotted versus needle lengths for positive and negative polarity, respectively, of 100 needles in CO_2.

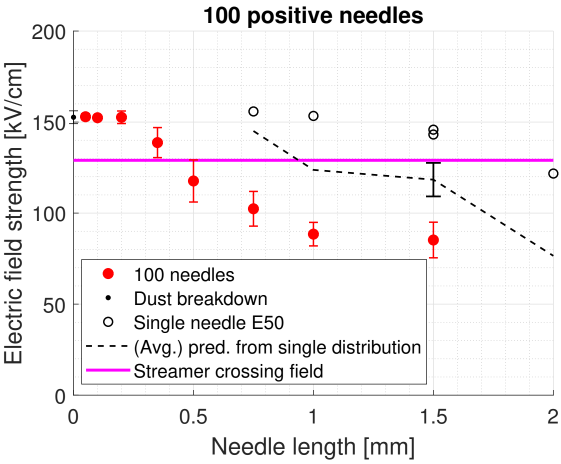

Figure 5.11: Experimental result of the E_{50} for 100 positive needles in CO_2. The calculated standard deviation of each resulting distribution is given as error bars of each E_{50} value. The black dashed line represent the prediction for 100 needles based on the single needle distribution. The y-axis refers to the uniform (average) background field strength.

The results of the 100 needles at positive polarity showed a further reduction of the 50% average background breakdown electric field strength when compared to the 20 needles results. Breakdowns occurred more frequently at the shorter needle lengths. The results showed an insensitivity of the needles until needle lengths between 0.2 and 0.35 mm. When compared to the predictions, there was a discrepancy where the results were significantly lower than the predictions.

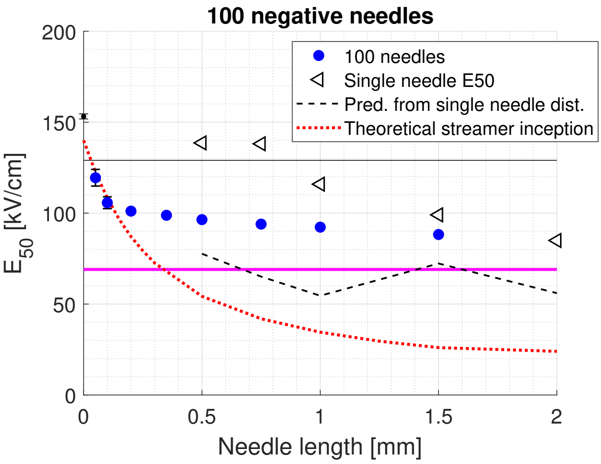

Figure 5.12: Experimental result of the E_{50} for 100 negative needles in CO_2. The calculated standard deviation of each resulting distribution is given as error bars of each E_{50} value. The black dashed line represent the prediction for 100 needles based on the single needle distribution. The y-axis refers to the uniform (average) background field strength.

For the negative 100 needles, a similar trend to what was observed with the 20 needles was seen. The 50% average background breakdown electric field strength were reduced to values around 85-100 kV/cm. Compared to the 20 Needles, the reduction for 100 needles occurred at shorter needle lengths. There was a disagreement between the predictions and the results where the predicted values were lower than the obtained results.

5.7 Rough Surfaces

This section presents the results of the two rough areas tested in SF_6 and CO_2. The effective area was determined by measuring the distance from the axi-symmetry line to the outermost breakdown mark of both the plugs and the Rogowski electrode. The effective area of the plugs was 2.383 cm^2 and 64.465 cm^2 for the Rogowski electrode. This gave an enlargement factor of $n = 27.05$, which was then used for the predictions. The plugs were adjusted for field enhancement, explained in Section 4.9.2. This was done to get comparable results for between the non-uniform field distribution from the plugs and the quasi-uniform field distribution from the Rogowski electrodes. The enhancement factor was found as explained in Section 4.9.3 to be 1.4018. All voltages obtained from the results with the plugs were multiplied with the enhancement factor before evaluating the $50\,\%$ average background breakdown field strength, .

5.7.1 SF_6

Figure 5.13 shows the results for the positive polarity of the plug and the Rogowski electrode. The results showed that there was a reduction from the results for the plug. The reduction was larger than what Was predicted from the enlargement law based on the distribution from the plug. The distributions for both the plug and the Rogowski electrode were used to predict the results in both directions. When predicting from the plug to the Rogowski, the enlargement factor was $n = 27.05$. When predicting from the Rogowski to the plug the enlargement factor was $n = 1/27.05$. The prediction for the area of the plug based on the distribution of the positive Rogowski predicts a slight increase in the 50 % breakdown electric field strength, but it was too pessimistic when compared with the results of the plug.

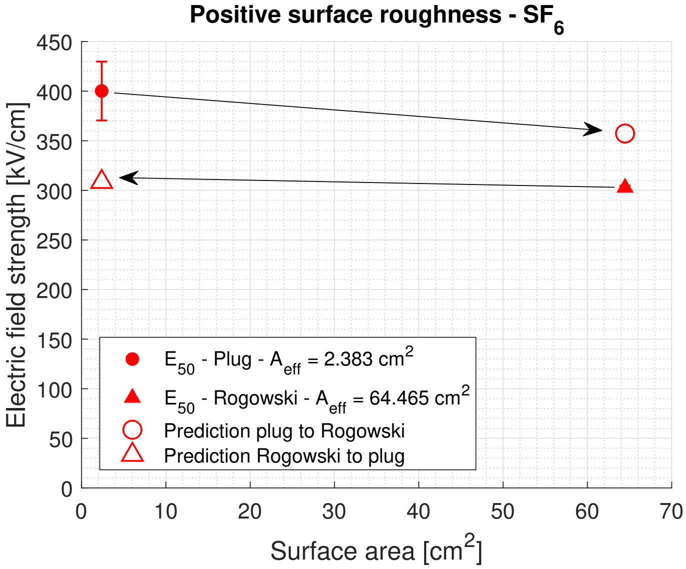

Figure 5.13: Results from rough surfaces at positive polarity in SF_6. Arrows from E_{50} to prediction box indicate direction of applied enlargement law.

With negative polarity in SF_6, Figure 5.14, there was a slight decrease in the 50 % average background breakdown electric field strength. This was in good agreement with the predictions from both the plug to the Rogowski and vice versa.

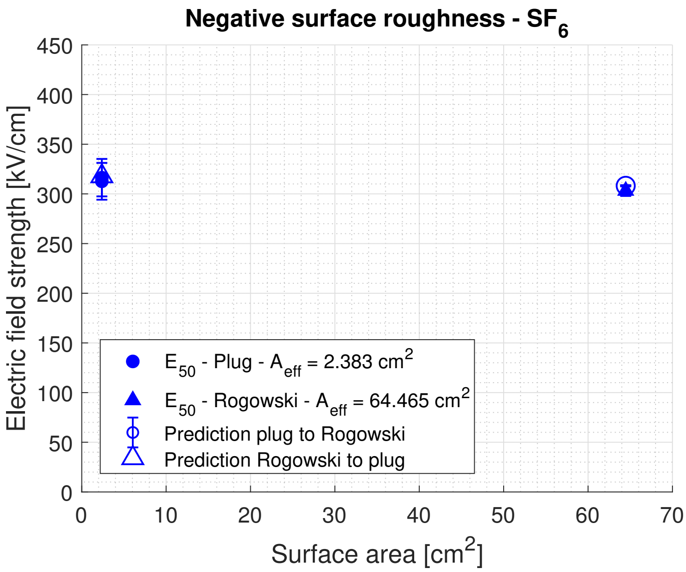

Figure 5.14: Results from rough surfaces at negative polarity in SF_6. Arrows from E_{50} to prediction box indicate direction of applied enlargement law.

5.7.2 CO_2

The results for positive polarity of the rough surfaces in CO_2, Figure 5.15, showed a significant reduction when increasing the effective electrode area. The prediction missed quite significantly with positive polarity in CO_2, similar to positive polarity in SF_6.

The results with negative polarity of the rough surfaces in CO_2, show a smaller degree of reduction than positive polarity. There was a discrepancy between the obtained results and the predictions.

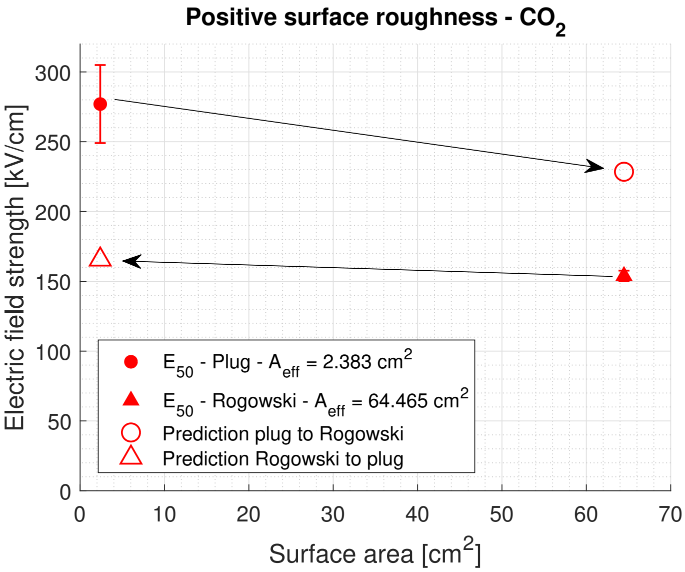

Figure 5.15: Results from rough surfaces at positive polarity in CO_2. Arrows from E_{50} to prediction box indicate direction of applied enlargement law.

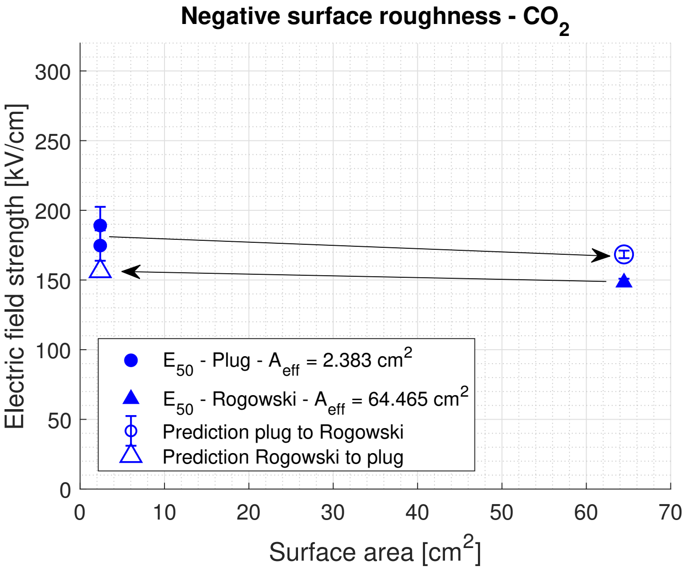

Figure 5.16: Results from rough surfaces at negative polarity in CO_2. Arrows from E_{50} to prediction box indicate direction of applied enlargement law.

Chapter 6

Discussion

6.1 Determining the Empirical Cumulative Distribution Function

In order to fit distribution functions, besides using *probit*, several methods of determining the empirical cumulative distribution function (ECDF) were used. The first method was the method described by Hauschild and Mosch [12]. In that method each breakdown was sorted in ascending order and given the probability of $1/(n+1)$, where n was the total number of breakdowns. Then the ECDF was estimated by cumulative adding the probability of each breakdown. The problem with this method was that it did not consider when the overlapping voltages of breakdowns and holds ended. I.e. the probability could be very close to 100 $\%$, but because the ECDF of this method just continued its increase until the last recorded breakdown voltage, the ECDF was at too low probability. This made the estimated ECDF to be shifted to too high voltages compared with previous work and the method was deemed to be unsuitable for this thesis.

One modification to the method of Hauschild and Mosch was to only consider the breakdowns in the voltage range from the first breakdown to the highest voltage recorded as a hold. The result of this method was plotted as black crosses and labeled ECDF in Figures 6.1 and 6.2 for estimates for 1 mm needle with positive and negative polarity in SF_6, respectively. However, these estimates were still at too high fields compared to previous work and the resulting plots using the probit method to fit binomial data. The downside of this method of estimating the ECDF was that it only regarded the information at the voltages with breakdowns and ignored the information given at voltages with holds. An algorithm was created to calculate the frequency over a number of shots or voltages. This was inspired by the frequency calculations with constant voltage tests from Hauschild and Mosch, where one tests the same voltage x times and calculates the breakdown frequency n/x where n is number of breakdowns. With the random test method the voltages were rarely identical. The breakdown frequency was calculated in steps of either 20 shots or within 10 kV/cm. This limitation was set to get estimates for the ECDF close enough to each other. This was plotted as orange dashed lines in Figures 6.1 and 6.2. The frequency method gave resulting estimates closer to previous work, compared to the previous methods. The downside of this was that it created an uncertainty of where in the field voltage interval the estimate actually was, which was why the line was plotted as the mean was, with the horizontal error bars indicating where the highest and lowest field strength in the evaluated interval was.

Additionally to just the uncertainty of where the points were, it reduced the experimental results for fitting to quite few points, compared with the number of breakdowns. After

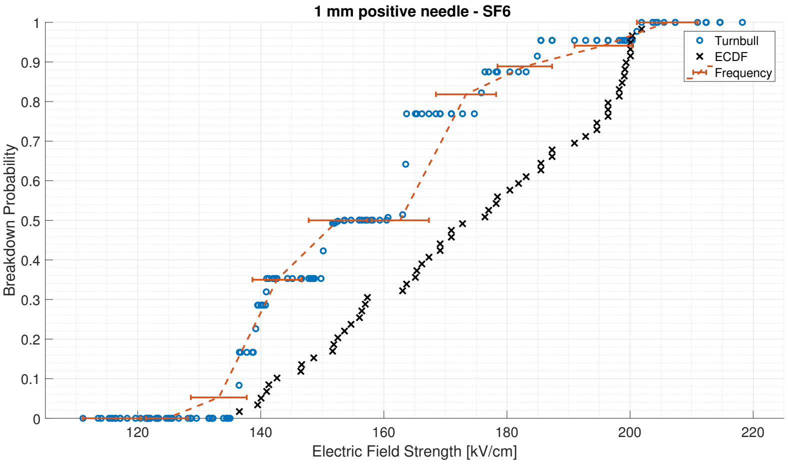

Figure 6.1: Comparison of different methods of estimating the empirical cumulative distribution function for 1 mm positive needle in SF_6. The x-axis refers to the uniform (average) background field strength.

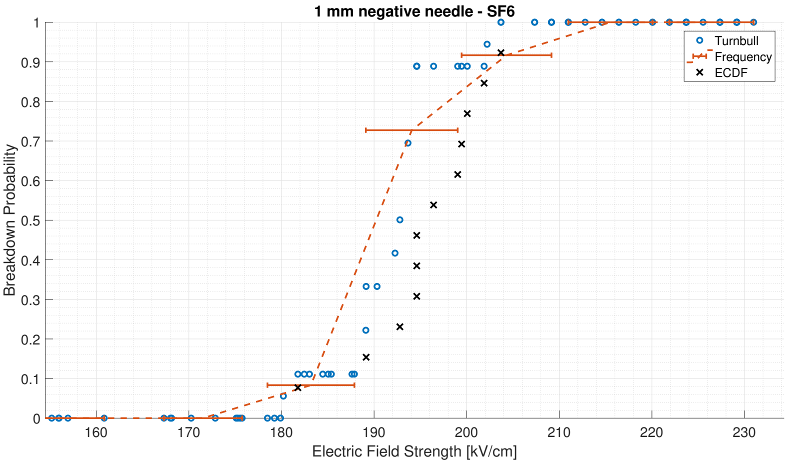

Figure 6.2: Comparison of different methods of estimating the empirical cumulative distribution function for 1 mm negative needle in SF_6. The x-axis refers to the uniform (average) background field strength.

communication with Senior principal scientist Kai Hencken, who suggested that the Turnbull algorithm could be a viable option, presented in Section 4.11.2. This was implemented and plotted as blue circles for the same data and in Figures 6.1 and 6.2. It was observed to be a decent agreement between the frequency plots, the Turnbull algorithm, previous work and with the probit fits (not shown). The benefit for distribution fitting with the

Turnbull algorithm was that there was an estimate of the cumulative probability for each tested voltage, giving more points for distribution fitting.

One behavior of the Turnbull algorithm was that it seemed to create steps in the ECDF estimations. This was the result of a range where there were a lot of holds and the algorithm determined that there were no increase in probability compared to the previous field strength. This was also an indication of the resolution in the *breakdown region*.

Inspired by what was done when the confidence intervals of the fits was determined, Section 4.11.4. The median at each voltage (or electric field strength) was found from the Turnbull results of all the N samples. This was done to investigate the behavior and was compared with the initial Turnbull from the original data set as blue circles and the median (bootstrap) estimated Turnbull results as black crosses, without fits in Figure 6.3 and with fits in Figure 6.3b. The estimates bootstrap Turnbull median estimates were more continuously increasing for each increasing field strength compared with the *step* behavior of the Turnbull of the original data set. Figure 6.3b, shows the red three parameter Weibull curve fitted to the original data set, while the black curve was the three parameter Weibull fitted to the bootstrap median Turnbull estimate. The difference between the two was small. The bootstrap median estimates gave interesting results and its accuracy to predict the ECDF should be investigated further.

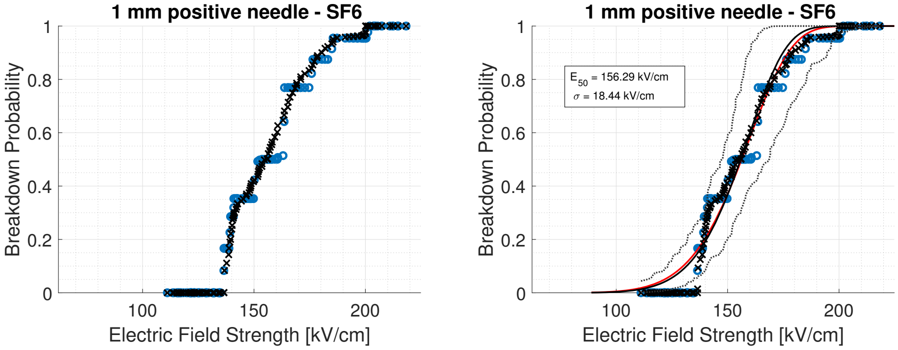

(a) **(b)**

Figure 6.3: Bootstrap Turnbull algortihm median estimates for the empirical cumulative distribution function (black crosses) compared with the Turnbull estimates of only the original results (blue circles) in (a) and (b). Red fitted to the original Turnbull estimates and black to the bootstrap estimates in (b). The x-axis refers to the uniform (average) background field strength.

6.2 Comparison of Distributions

The accuracy of a distribution made from a 100 shots fit in the low probability range was investigated. To do this 500 shots were performed in CO_2 with 100 needles and 1 mm needle length. The shots were set in the low (0-10 %) probability region based on the previously obtained distribution function fitted to 100 shots of the full range. The result of running this through the Turnbull algorithm, with a self-consistency of $1e-6$, was then compared to the three parameter Weibull distribution and Normal distribution fitted with the probit method to 100 shots with full electric field strength range of the probabilities, See Figure 6.4.

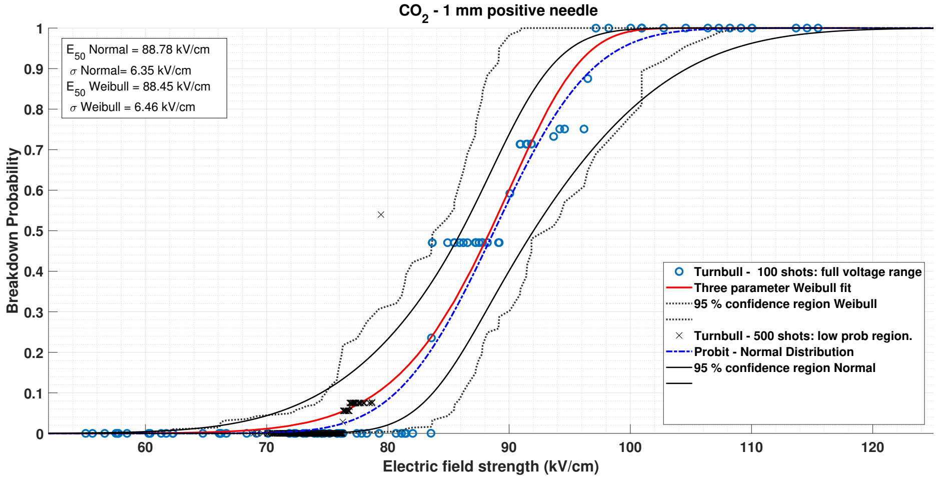

Figure 6.4: Comparison of three parameter Weibull distribution and the normal distribution based on the full test range. Compared with the Turnbull ECDF of 500 shots in the low probability range indicated as black crosses. The x-axis refers to the uniform (average) background field strength.

Both the three parameter Weibull and Normal distributions had similar 50 % breakdown field strengths. The Normal distribution gave higher field strengths at the same probabilities compared to the Weibull. When compared to the Turnbull results of the 500 shots (black x's), the Weibull distribution seemed to fit better than the Normal distribution to the Turnbull estimates at 0.08-0.09 probability. The Turnbull point at around 80 kV/cm and 0.55 probability was neglected for the comparison. It was likely that it ended up at that high probability due to it being at the end of the test range for the 500 shots. If a full range had been tested, it would likely be lower due to more holds at higher electric field strengths. This behavior was seen with the Turnbull algorithm from other tests as well when incomplete test ranges were applied.

Just considering the three parameter Weibull and Normal distribution fits in Figure 6.4, the behavior at low probabilities was of interest for design purposes where one designs after a minimum allowable probability, e.g. 2 %. From the fits in Figure 6.4, it was possible to extract the electric field strength at that probability. In this case the difference between the 2 % values is around 5 kV where the three parameter Weibull distribution was at lower field strengths than the normal distribution for same probability. This was not always the case, and especially when the distributions were closer to the value set as the zero position for the Weibull (streamer inception), in those cases, the Weibull distribution would be steeper and have low probabilities at field strengths higher than the normal distribution. This was considered an upside of the Weibull distribution compared to the normal distribution, which had a probability range that continued until negative infinity.

The confidence bands for the different distributions were shown as well in Figure 6.4. The choice to just evaluate the confidence at the tested field strengths gave *rough* confidence bands. These were evaluated at the 2 % probabilities to give an indication of the certainty of the E_2 estimates. The figure also showed that for most field strengths, the confidence band of the three-parameter Weibull distribution was larger than the ones for the normal distribution. Which was common behavior of confidence bands from the bootstrap percentile method [74].

6.3 Accuracy of Using 100 Shots in Each Experiment

As explained in Section 3.5.1 the presented probabilities were estimates based on a number of shots. To get an exact estimate of the probabilities and the distributions function one needs an infinite number of shots, see Equation 3.21. To see how close the estimates using 100 shots were, one test with 500 shots of the full range in CO_2, without any needles present, was performed. The data set was fitted with the three-parameter Weibull distribution with incremental steps of 1 shot from the 10 first shot until the full 500 shots. The E_{50} and the corresponding standard deviation, σ, were plotted versus the number of shots used for estimation in Figure 6.5. The final values of E_{50} = 153.13 kV/cm and for σ = 1.39 kV/cm were plotted as dashed red lines for comparison. Around 65 number of shots, the E_{50} reaches very close the final value and from there on it oscillated around the final value, see Figure 6.5a. The results for the standard deviation, σ, in Figure 6.5b showed that the standard deviation had a relatively big spike before a drop to a quite low value in the early number of shots. The standard deviation did not start oscillating around the final value until after approximately 360 shots.

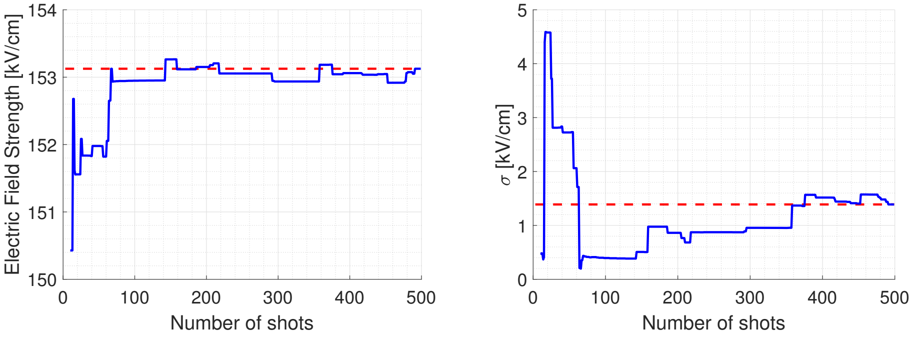

(a) E_{50} **(b)** σ

Figure 6.5: The y-axis of the plots are cut to better show the oscillation, an uncut version of Figure 6.5a is given in Figure B.1 in the Appendix B. The y-axis of (a) refers to the uniform (average) background field strength.

The data set was evaluated in the same way with the order of the shots picked randomly to see if there was a difference. Two resulting E_{50} plots are shown in Figure 6.6. The E_{50}

values showed similar behavior as the incremental evaluation. The maximum difference in the three figures at 100 shots were in Figure 6.6a, where the difference between the estimate and the final result from 500 shots was 0.74%.

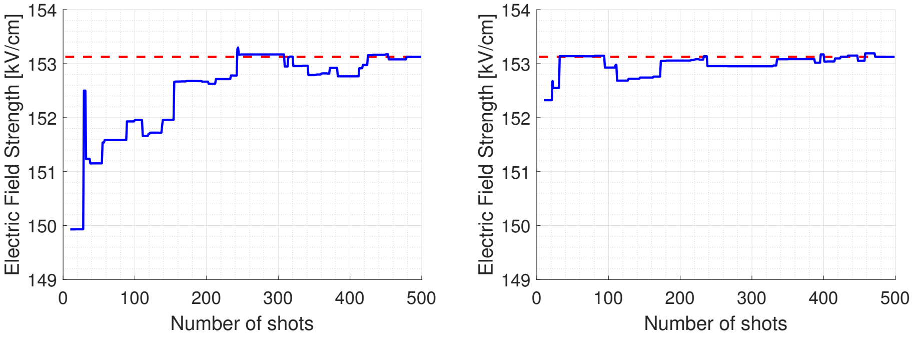

(a) **(b)**

Figure 6.6: E_{50} evaluated with random order of shots. The x-axis refers to the uniform (average) background field strength.

The corresponding standard deviations to the E_{50} in Figure 6.6 were shown in Figure 6.7. The behavior of the standard deviation oscillated around the final value as well. Though the difference at 100 shots was approximately 25% of the standard in Figure 6.7a as an example. Which was relatively bigger compared to the difference of E_{50} at 100 shots.

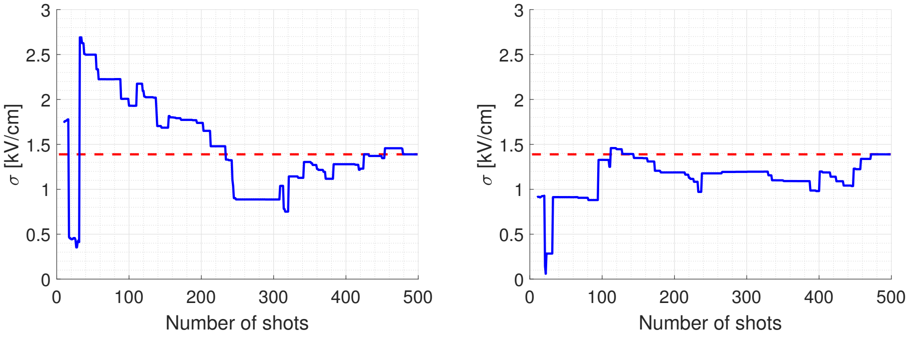

(a) σ for the E_{50} in Figure 6.6a **(b)** σ for the E_{50} in Figure 6.6b

Figure 6.7: σ evaluated with random order of shots.

This showed that 100 shots should be sufficient[1] for a good estimate of the E_{50}. For a good estimate of the standard deviation, 100 shots might not be sufficient and the required number should be investigated further. The expectation was that the standard deviation would decrease as the sample size increased. The explanation for the different behavior might

---

[1] Given a proper test range.

be how the distribution changes with an improper resolution of the breakdown region and how the variance (and standard deviation) was calculated from the Weibull parameters, see Equation 3.33. The steeper the distribution gets the smaller the standard deviation becomes. As the standard deviation represents the spread around the mean, it was expected in the end to end up at the standard deviation dictated by the physical processes. However, even if the standard deviation had some uncertainty, 100 shots was a good compromise between accuracy and time for testing.

6.4 Effect of needle protrusions in SF_6

6.4.1 Single needle and gap distance

The results showed that SF_6 was quite sensitive to the needle protrusions. Figure 6.8 shows a comparison of the results between positive and negative polarity of the needle in SF_6.

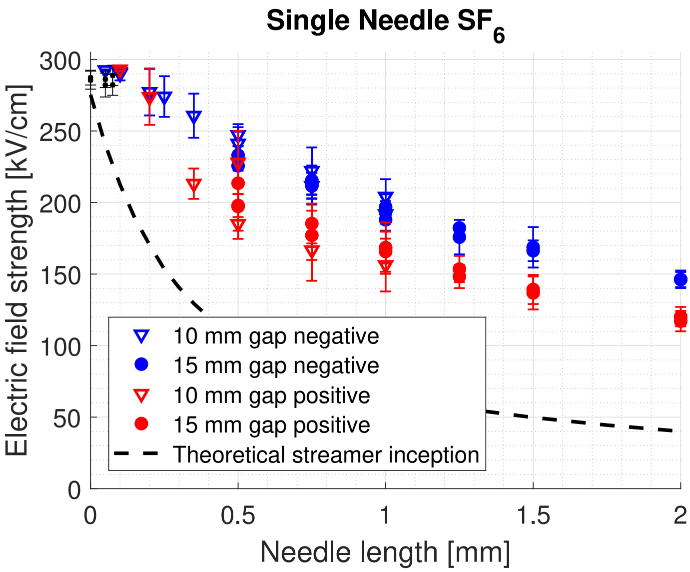

Figure 6.8: Polarity comparison between positive and negative needle in SF_6. The y-axis refers to the uniform (average) background field strength.

As mentioned in Section 5.1, positive polarity was lower than negative polarity and that the positive polarity had a bigger scatter than negative polarity. This difference in scatter was possibly explained by the first electron dependence at small protrusion lengths, where it was difficult to get a first electron in the critical volume in front of a single needle. When comparing the slope/trend of the results, the polarities follow a somewhat parallel dependence, as one would expect from [6]. For the needle lengths below 0.35 mm, the breakdown field strengths of the polarities stop being parallel and positive polarity gets closer to negative polarity, this was likely due to the first electron criterion dictating when the breakdown occur and not the leader criterion at the short needle lengths being the decisive criterion.

6.4.2 Multiple Needles

Increasing the number of needles caused a decrease in the 50 % average background breakdown electric field strength. For negative polarity the E_{50} value had a (non linear) decrease when increasing the number of needles, as shown in Figure 6.9. For positive polarity on the other hand, Figure 6.10, there was a decrease when increasing the number of needles from one to 20 and 100, but the results of 20 and 100 needles had no significant difference. The overlapping of the results for positive polarity might indicate that there was a physical lower limit which was reached already at 20 needles. This might be explained with that going from 1 to 20 needle increased the probability of getting a first electron to start the discharge process. However, this reached a saturation at 20 (or less) needles, which then determined the required field strength for a breakdown. For negative polarity, where a first electron was expected at much lower field strengths, the reduction of the electric field strength when increasing the number of needles was likely due to a reduction of the formative time lag, i.e. it was more likely that one leader channel propagate through the gap and transition to a spark within time of a lightning impulse. It would be interesting to determine the limiting criteria for negative polarity by testing with even more than 100 needles, which should be at leader or streamer inception as the first electron is usually expected to always be available at the fields of needle protrusions [6].

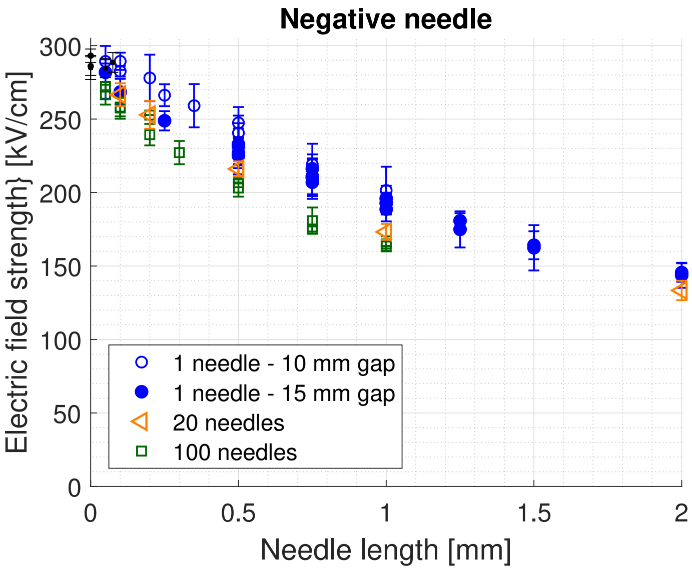

Figure 6.9: Comparison of the E_{50} results for negative polarity of 1, 20 and 100 needles. The y-axis refers to the uniform (average) background field strength.

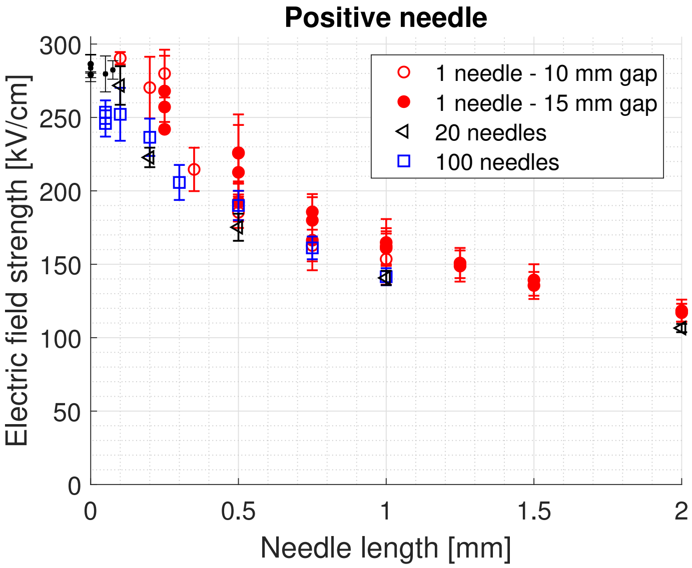

Figure 6.10: Comparison of the E_{50} results for positive polarity of 1, 20 and 100 needles. The y-axis refers to the uniform (average) background field strength.

Comparing the polarities of the 100 needles, Figure 6.11, showed that the difference between the polarities was smaller than for the single needle results.

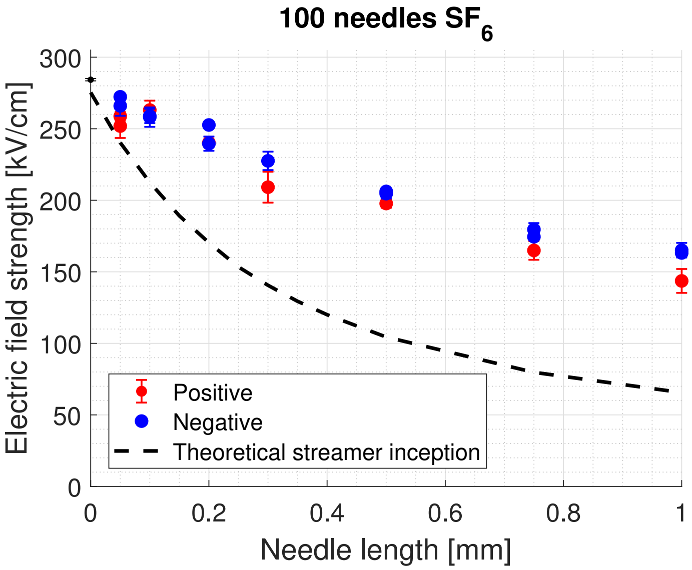

Figure 6.11: Polarity comparison between 100 positive and negative needles in SF_6. The y-axis refers to the uniform (average) background field strength.

6.4.3 Effect of Surface Roughness

The results from the tests with surface roughness showed no polarity difference for the Rogowski electrode. While for the plug, negative polarity was significantly lower than positive polarity. Something that can be explained that for such a small area, the lack of a first electron requires really high electric fields to initiate breakdowns. The recorded 50 % breakdown field strength at approximately 400 kV/cm. Which was higher than the critical field strength of SF_6 at 4 bar, 356 kV/cm (4 bar ·89 kV/cm·bar [13]).

The enlargement effect of increasing the effective surface area of the rough surfaces was larger for positive polarity than for negative polarity. While it was not very large with negative polarity, it was still a reduction.

6.5 Enlargement Law in SF_6

6.5.1 Enlargement Effect

Figures 6.12 and 6.13 show the E_{50} results plotted versus the number of needles for positive and negative polarity respectively. They confirmed the expectation from the enlargement law of a non linear decrease with a linear increase of the enlargement factor. For positive polarity, Figure 6.12 the 500 μm needle length actually had an increase in the breakdown field strength from 20 needles to 100 needles.

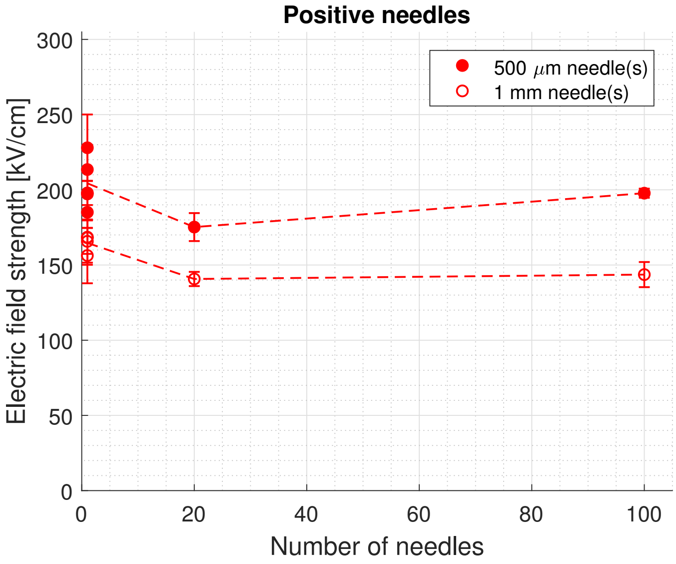

Figure 6.12: The E_{50} versus the number of needles for positive polarity of two needle lengths. The dashed line is given as the average where there were multiple results and is plotted as an eye guide. The y-axis refers to the uniform (average) background field strength.

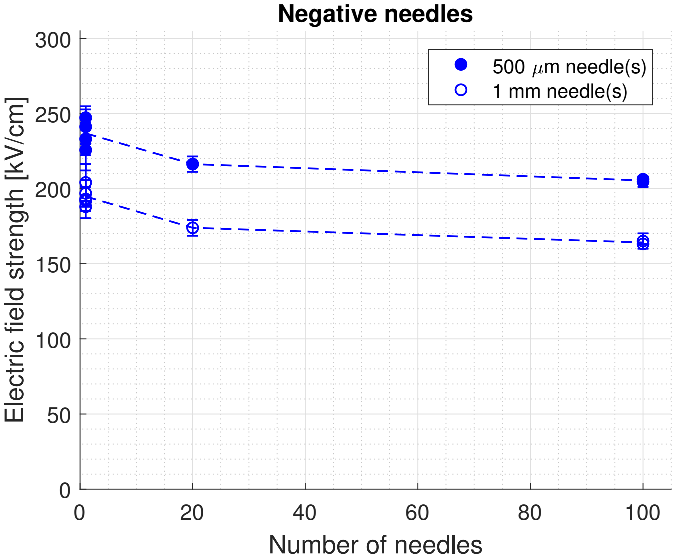

Figure 6.13: The E_{50} versus the number of needles for negative of two needle lengths. The dashed line is given as the average where there were multiple results and is plotted as an eye guide. The y-axis refers to the uniform (average) background field strength.

The expectation from the enlargement law was that when increasing the number of needles, the distributions become steeper and the standard deviation decrease. As the breakdown field strength changed when increasing the number of needles, the standard deviation also changed. To investigate the impact of the standard deviation from increasing the number of needles, the standard deviation was found as a fraction of its E_{50}. Figures 6.14 and 6.15 showed the relative standard deviation for positive and negative polarity respectively, which was the standard deviation divided by the E_{50} value. The reduction of the relative standard deviation from a single to multiple needles for both polarities confirmed that the enlargement law was in effect. The positive relative standard deviation for 20 needles was slightly lower than that of 100 needles, which was opposite of what was expected. For negative needles, the relative standard deviation was as expected where the relative standard deviation of the 100 needles were lower than the relative standard deviation of the 20 needles. The scatter of the relative standard deviation of the single needle was likely due to similar reasons of scatter in the E_{50} values. The results very close to zero was due to very steep distributions, which might be results of bad tests series lacking enough shots in the breakdown region.

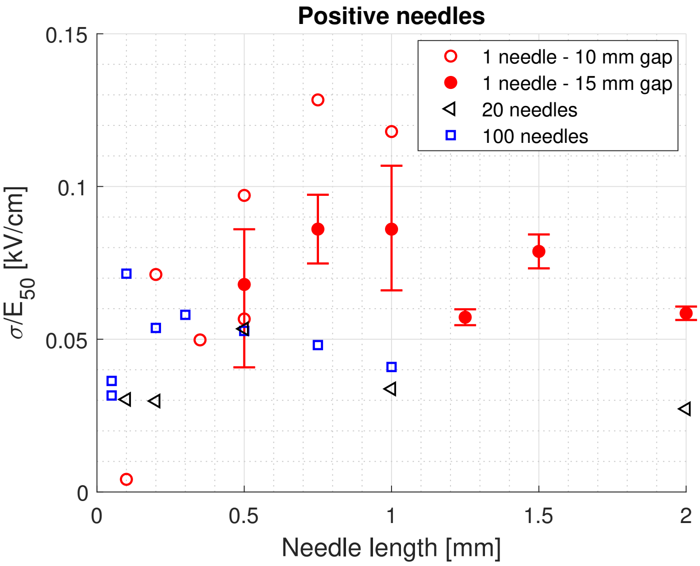

Figure 6.14: The relative sigma of the E_{50} value for positive polarity, for 1, 20 and 100 needles. Where more than one value was used, the average of all values was taken and the maximum and minimum value is indicated by the error bars.

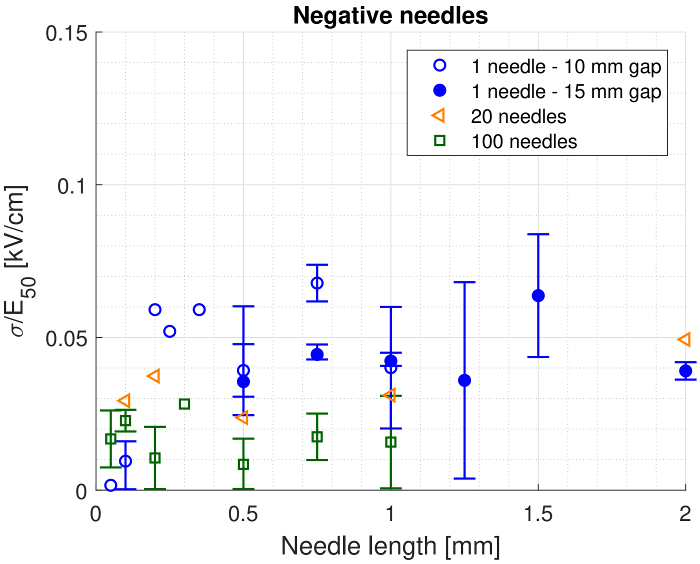

Figure 6.15: The relative sigma of the E_{50} value for negative polarity, for 1, 20 and 100 needles. Where more than one value was used, the average of all values was taken and the maximum and minimum value is indicated by the error bars.

6.5.2 Predictions

Using the single needle three parameter Weibull distribution for predictions worked well for 20 needles of both polarities. For positive polarity, the predictions for 100 needles were more pessimistic than the results. This discrepancy was not understood, but might be that the involved processes scales differently. It might be that at 20 needles, a lower limit has been reached, e.g. for first electron production or leader propagation. It might be that due to different lengths not all needles were equally influencing the breakdown statistics. This should be investigated further. One possibility could be to see if the scaling becomes better when determining the distributions of each individual needle length and combining them as Equation 3.49. Another thing to investigate could be how the scaling behaves for positive polarity, if the the first electron dependency is reduced by irradiating the needles with UV-light or X-rays.

For the surface roughness and increase in area in SF_6, there was also a discrepancy between the results and predictions for positive polarity. The predictions were based on the enlargement factor of just the area, $n = 27.05$. This factor disagreed when used from small to large and large to small area. When the empirical enlargement factor was determined for positive polarity, the factor that would be necessary to go from the plug to the Rogowski field strength. The empirical enlargement factor ends up at $n = 4445$. Calculating the other direction, based on the distribution of the Rogowski, the empirical enlargement factor becomes $n = 3.25 \cdot 10^{18}$. This factor was very high[2], the reason for the empirical enlargement factor being this large was not understood. For negative polarity of the plugs and Rogowski, the results and predictions agreed quite well (Figure 5.14) which removed the doubt that any wrong assumptions had been made in the adjustments of the field enhancement of the plug results. A possibility that the positive first electron productions do not scale according to the area. The scaling could be influenced of the surface structure which is a product of stochastic nature of sandblasting. As well, there was also a difference in the R_a, which might indicate that there were more minor peaks that influenced the results on the Rogowski. How the surface structure impacts the results should be investigated further.

6.6 Effect of needle protrusions in CO_2

6.6.1 Single needle

The positive single needle results in CO_2, Figure 5.7, showed that the breakdowns (and the resulting E_{50} where enough breakdowns happen at the needle) at needle lengths shorter than 1 mm, happen around the critical field strength. Seeger et al [40] found that region was where streamer crossing and spark transition took place. The reduction of the 50 % average background field at 1.5-2 mm, might be explained with leader breakdowns being decisive of the breakdowns. at the lengths lower than 1.5 mm, both streamer crossing, streamer to spark transition and leader breakdowns might be decisive.

---

[2] The factors were verified through inserting it in the prediction equation which gave predictions matching the result

The applied voltage impulse behaved like a DC step pulse, allowing all breakdowns of a single needle occurring within 15 seconds to be evaluated. This was done and is shown in Figure 6.16. The impact of the needle was more visible, however, very few breakdowns occurred at the needle at lengths shorter than 0.5 mm. There was a drop in the results compared to the *early* breakdowns. This change might indicate that for the lightning impulse voltages it was required a sufficiently low statistical and formative time lag, which required higher electric field strengths.

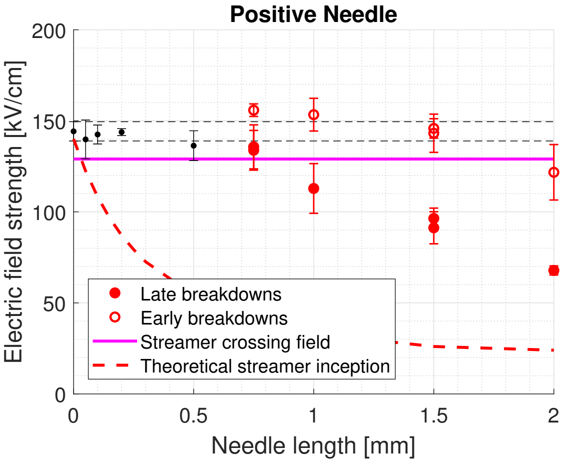

Figure 6.16: Comparison between positive lightning impulse (labeled early) and all (labeled late) breakdowns occurring within 15 seconds. The y-axis refers to the uniform (average) background field strength.

The results from a single needle with negative polarity in CO_2, Figure 5.8, had a large standard deviation for the needle lengths 0.5, 0.75 and 1 mm. This might be due to the uncertainty of having a streamer to spark transition in the time of a lightning impulse. This was visible when the results were compared to the results from 20 (Figure 5.10) and 100 (Figure 5.12) needles. It was also visible when investigating all the breakdowns, shown in figure 6.17. The E_{50} for all breakdowns was reduced to a similar value as 20 and 100 needles, around the streamer crossing and spark transition. The reduction of the streamer crossing for all breakdowns was in line with the observations found by Seeger et al [40].

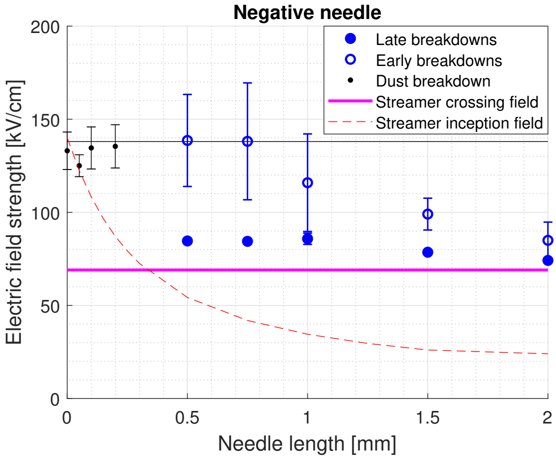

Figure 6.17: Comparison between negative lightning impulse (labeled early) and all (labeled late) breakdowns occurring within 15 seconds. The y-axis refers to the uniform (average) background field strength.

6.6.2 Multiple Needles

All the results from single, 20 and 100 needles for positive polarity were compared in Figure 6.18. As the breakdown values were lower than the streamer crossing after 0.35 mm for 100 needles, and later for the rest. It was assumed to be leader breakdowns that were decisive. The effect of increasing the number of needles created a sensitivity to the needles at shorter lengths. Something which could indicate that when the number of needles was increased, there were more first electrons available. Comparing Figure 6.18 with Figure 6.16 The effect of increasing the number of needles had a similar effect as increasing the applied time of the voltage impulse. This could be explained by that the single needle required sufficient high field strengths to have low enough statistical and formative time lags. The formative time lag, transition and spark formation was not expected to change with the number of needles, only with the applied field. However, increasing the number of needles, should increase the probability of having a first electron and, thus, reducing the statistical time lag. Resulting in streamer inception creating a leader channel which could propagate through the gap and transition to a spark within the time of a lightning impulse.

The results of single, 20 and 100 needles with negative polarity in CO_2 were compared in Figure 6.19. The E_{50} value were reduced down and seemed to saturate at the streamer crossing and streamer to spark transition field strength. This reduction occurred at shorter needle lengths for 20 and 100 needles. The short needle lengths with 100 needles coincided with the theoretical streamer inception calculations made from the COMSOL field simulations of a single needle. At needle lengths above 0.5 mm, there was no difference between the results with 20 needles and the 100 needles. Indicating that the enlargement saturates already at 20 needles (or less). This could indicate that streamer crossing and streamer inception was decisive for breakdowns for negative polarity and at needle lengths

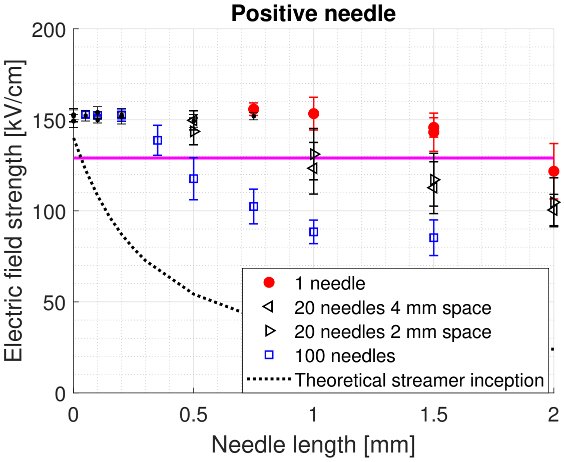

Figure 6.18: Comparison of the E_{50} for positive polarity 1, 20 and 100 needles. The y-axis refers to the uniform (average) background field strength.

lower than 2 mm. Similarly as for positive needles CO_2, the effect of increasing the number of needles behaves as increasing the applied time of the voltage impulse which can be seen from comparing Figures 6.17 and 6.19.

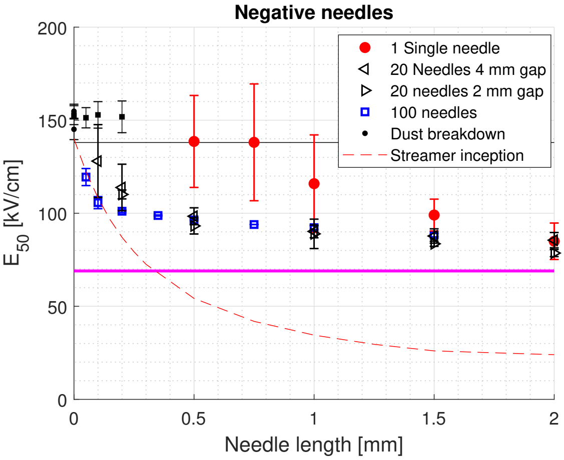

Figure 6.19: Comparison of the E_{50} for negative polarity 1, 20 and 100 needles. The y-axis refers to the uniform (average) background field strength.

6.6.3 Effect of Surface Roughness

The results for the surfaces showed no significant difference between the polarities of the E_{50} of the Rogowski electrode in CO_2. For the plugs, there was a significant difference between positive (Figure 5.15) and negative (Figure 5.16) polarity, where positive polarity was significant higher than negative polarity, which might indicate a lack of first electron for the positive plugs.

6.7 Enlargement Law in CO_2

Figures 6.20 and 6.21 confirmed the expected behavior of a non linear decrease of the E_{50} with a linear increase of the enlargement factor, as expected from the enlargement law. For negative polarity, the ”saturation” between 20 and 100 needles can be seen in Figure 6.21.

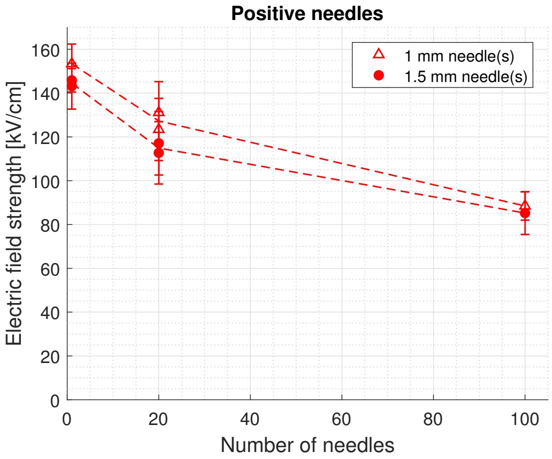

Figure 6.20: The E_{50} versus the number of needles for positive polarity of two needle lengths. The dashed line is given as the average where there were multiple results and is plotted as an eye guide. The y-axis refers to the uniform (average) background field strength.

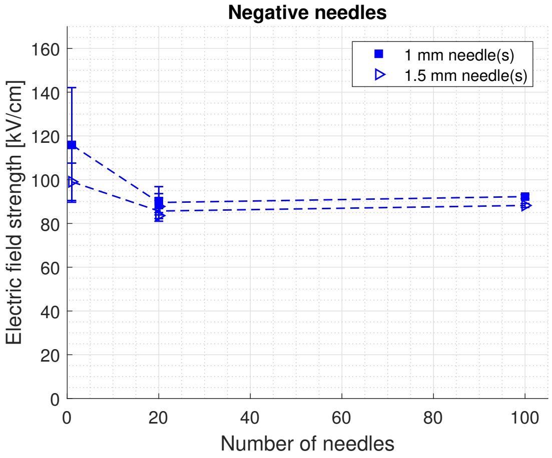

Figure 6.21: The E_{50} versus the number of needles for negative polarity of two needle lengths. The dashed line is given as the average where there were multiple results and is plotted as an eye guide. The y-axis refers to the uniform (average) background field strength.

Figures 6.22 and 6.23 show the relative standard deviation of the results in CO_2. Negative polarity behaved as expected where the relative standard decreased with increasing number of needles confirming the enlargement law. With relative standard deviation of single needle $>$ 20 needles $>$ 100 needles. For positive polarity, the relative standard deviation was more scattered between the number of needles and seemingly increasing with increasing needle length. This was contradictory to what was expected. It was expected to remain at a constant level or decrease with increasing needle lengths, as longer needle lengths leads to higher field enhancements and increase the critical volume for a first electron to appear in, which would decrease the scatter. One explanation for the increase in the positive relative standard deviation might be that at the lower needle lengths the E_{50} is close to the critical field, giving a very small breakdown region and thus a small standard deviation. The breakdown region was small due to the required field strengths already was higher than the critical field strength. Increasing the applied field above this caused ionization and avalanches to be able to start anywhere in the gas in the gap. Thus there was an upper limit when crossed breakdowns ”always” happened. This upper limit was not much higher than that of positive streamer crossing and spark transition field strengths. This could be the reason for the standard deviation being small for shorter needles. When the leader mechanism took over as the decisive breakdown mechanism, the breakdown region increased and gave a bigger standard deviation while reducing the E_{50}. Which would give an increase in the relative standard deviation. This requires further investigation to verify and understand.

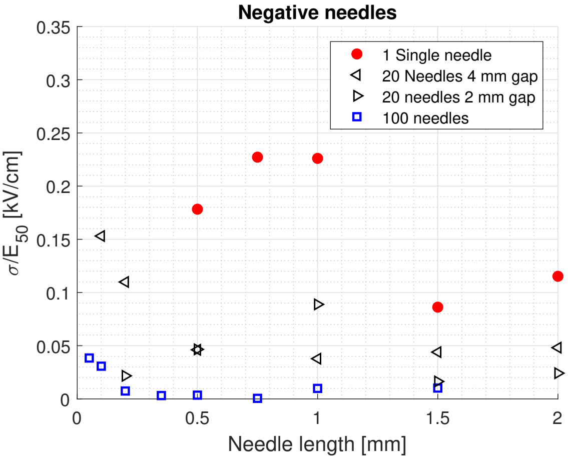

Figure 6.22: The relative sigma of the E_{50} value for negative polarity for 1, 20 and 100 needles.

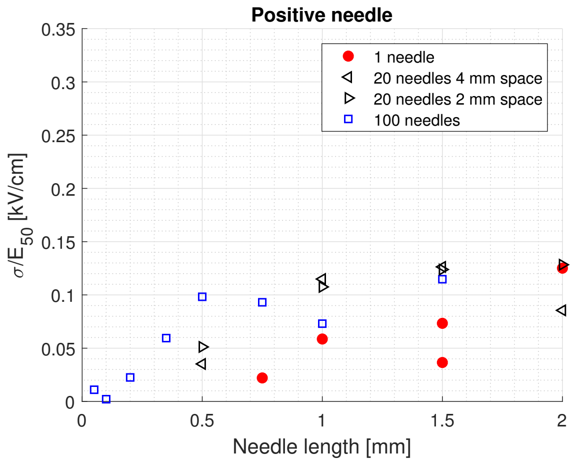

Figure 6.23: The relative sigma of the E_{50} value for positive polarity for 1, 20 and 100 needles.

6.7.1 Predictions

There was a decent agreement when the predictions were compared with the results for both polarities with 20 needles (Figure 5.9 and 5.10) in CO_2.

When the predictions were compared with the results for the 100 positive needles in CO_2 there was no longer an agreement between the two. The predictions were significantly higher than the obtained results. To see if this would change, predictions for the 100 needles were made from the distributions obtained with 20 needles, see Figure 6.24. Still the predictions were too optimistic compared to the results with 100 needles.

This was not well understood, but a possible explanations might be that the single needle distributions were dependent on the first electron criteria, which leads to scatter and higher required electric field strengths. Increasing the number of needles or increasing the time, remove the dependency of the first electron and the other breakdown criterion were important for the required breakdown field strengths. Thus, for multiple needles, the leader inception, propagation and spark transition becomes decisive for breakdowns. The discrepancy between the predictions and the results might be explained that the previously mentioned breakdown criteria scale differently. Determining the involved breakdown mechanism and how they scale should be investigated further. As already mentioned, it would be interesting to investigate the behavior of positive polarity when the first electron dependency was nearly eliminated through UV or X-ray radiation of the needles.

The results of the 100 negative needles also missed the predictions, which were too low compared with the results. Which could be explained with the negative E_{50} results reached a lower limit at streamer crossing and spark transition where no breakdown could occur at lower electric field strengths. To account for these kind of physical limits, the zero position of the initial Weibull distribution must be set at the right value, which at the shorter needle lengths, up to 1.5 mm, might be at the streamer crossing. Using the lower limit at the

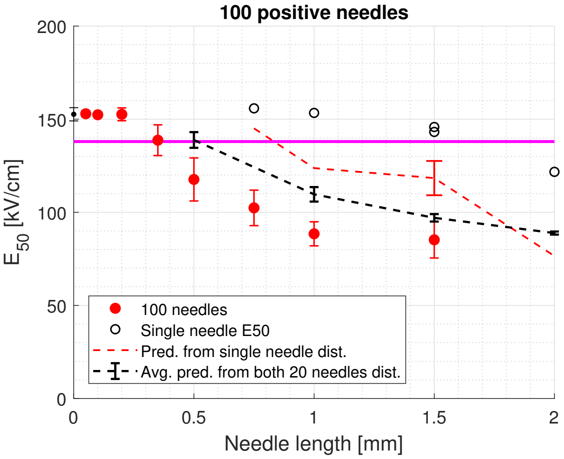

Figure 6.24: E_{50} of 100 negative needles in CO_2, with old predictions based on the single needle distributions and new predictions based on both 20 needle distributions. The y-axis refers to the uniform (average) background field strength.

streamer crossing, the predictions that were below the streamer crossing field strength (purple line) in Figure 5.12, would move up to the streamer crossing. This was done, see Figure 6.25. Still the predictions were too low compared with the results. To determine the field strength required for spark transition for lightning impulse voltages and whether or not this could be set as the exact zero position instead of just streamer crossing would require further investigation.

Comparing the results with the predictions of the surface areas in CO_2, both polarities miss with the predictions, see Figure 5.15 and 5.16. Calculating the empirical enlargement factor based on the positive plug distribution to the Rogowski result, gave the empirical enlargement factor $n = 386259$, which was a lot larger than the enlargement factor of just the area at 27.05. For the negative plug distribution, the empirical enlargement factor when based on the negative plug distribution, was $n = 31680$. Indicating that there might be other processes involved that do not scale equally with area.

6.8 Shielding Effect

As was presented in Section 5.5, two different setups were used for the 20 needles in CO_2. In the first setup the needles had one empty hole between each needle which gave 4 mm spacing. The other had no empty holes between the needles which gave the minimum of 2 mm space between the needles. The 3D model with 9 needles and 25 holes used for simulations with 4 mm space between the needles in COMSOL is presented in Figure 6.26. This model was used to simulate the electric field strength along the center line of the center needle and the corner needle for the needle lengths 1 and 2 mm with both 2 and 4 mm spacing between the needles.

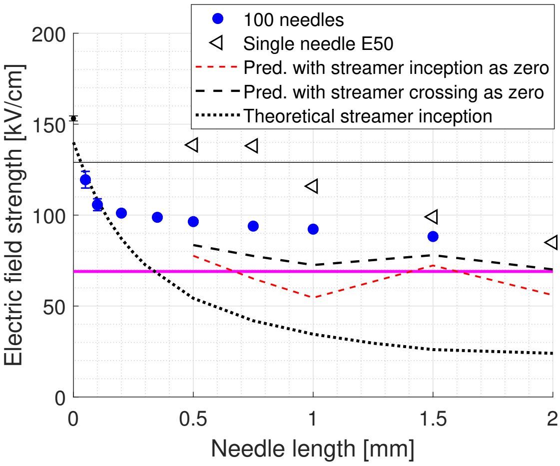

Figure 6.25: E_{50} of 100 negative needles in CO_2, with old predictions where streamer inception was used as zero position for the distribution and new predictions where streamer crossing is used as the zero position for the distributions. The y-axis refers to the uniform (average) background field strength.

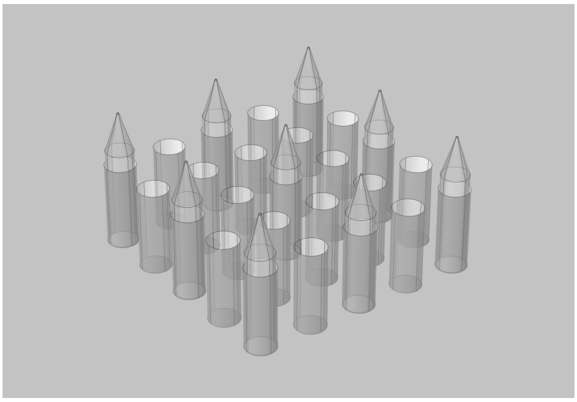

Figure 6.26: Close up of the needle array simulated in COMSOL showing 2 mm needles with 4 mm spacing between the needles.

The simulation results presented in Figure 6.27, showed the electric field strength of a single needle, center and corner needle from the needle array in Figure 6.26 for the different parameters. Figure 6.27a show that there was no noticeable reduction in the field strength for the 4 mm spacing of the needles when the needles were at 1 mm lengths. The simulations also showed that there was a reduction of the electric field strength for the corner needle and a larger reduction for the center needle when decreasing to 2 mm spacing of the needles.

Increasing the needle lengths to 2 mm, see Figure 6.27b, showed more of a decrease in the electric field strengths. There was a shielding effect for all needles. However, for 4 mm spacing, the effect was small compared to the reduction of 2 mm spacing. For the center needle the max field at the needle tip was reduced to 76 % of that of the single needle.

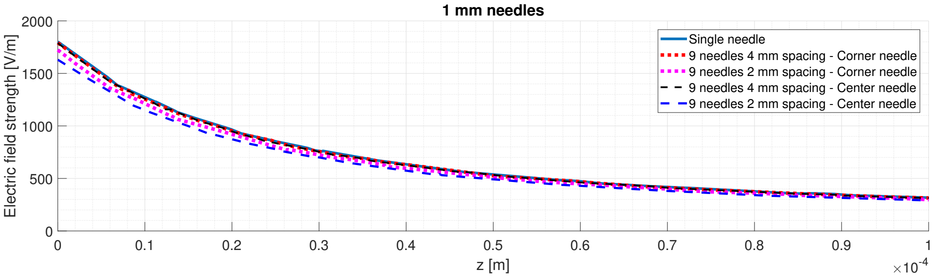

(a) 1 mm needles.

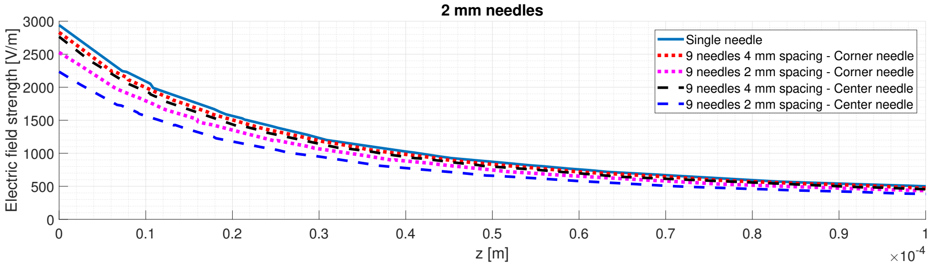

(b) 2 mm needles.

Figure 6.27: Results from electric field strength simulations of the needle array shown in Figure 6.26. Showing the electric field strength the first 100 μm from the needle tip.

These simulations showed that with 4 mm spacing of the needles, the needle behaved as independent needles at 1 mm lengths. However, there was a shielding effect of the needles at 2 mm needle lengths and 4 mm spacing. The reductions were approximately 6.0 % of the maximum field strength for the center needle and approximately 3.8 % reduction of the maximum field strength for the corner needles.

The experimental results with 20 needles in CO_2 showed a slight increase in the electric field strength for the 2 mm spacing with positive polarity, see Figure 5.9. Qualitatively, this would be as expected from the simulations as a reduction in the field enhancement of the needles would require higher background field strengths to reach the same field of the needles without the shielding effect and cause breakdowns. For negative polarity shown in Figure 5.10, the results with 2 mm spacing of the needles were all slightly lower than the results from 4 mm spacing. Unless the proximity effect has a polarity difference, it shows that for the tested lengths, the impact is minimal or within the uncertainties for negative polarity.

6.9 Multiple Needle Effect on the Withstand Field

When working with insulation, the withstand properties are of interest from a design perspective. This is a fluctuating definition, but in the region from 0 to 1 - 2 % probability of breakdowns. From the Weibull distribution fits the 2 % breakdown field strength will be presented in the following sections. Since the low probability values were very dependent on the distribution would require a lot of shots to get precise results, the 95 % confidence interval of the E_2 will be presented to give an indication of the certainty of the estimates. One note for all the following plots including the E_2 confidence region. Technically it was wrong to draw lines between the confidence regions and shade them, as no information was known between the measured points. However, for visibility they were presented as shaded areas, instead of error bars.

6.9.1 SF_6

For single needle with positive polarity, the E_{50}, E_2 and the confidence region of E_2 were plotted in Figure 6.28. Due to much scatter of the single needle results, the confidence region was quite large between 0.5 and 1 mm needle lengths. Besides the scatter, the E_2 followed nicely the trend of E_{50}.

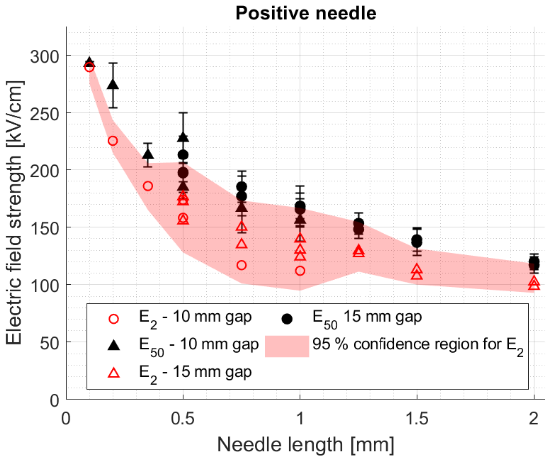

Figure 6.28: E_2 values of the positive single needle distribution, with the 95 % confidence region for E_2 as the shaded red region. At needle lengths with several results, the maximum and minimum value was used for the 95 % confidence region. Compared with the E_{50} as black symbols.

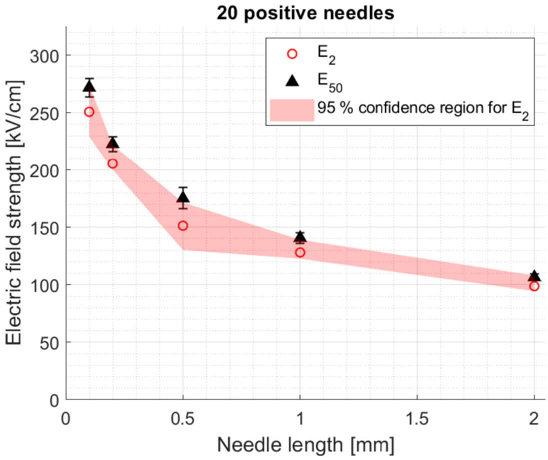

Figure 6.29: E_2 values of the positive 20 needles distribution, with the 95 % confidence region for E_2 as the shaded red region. Compared with the E_{50} as black symbols. The y-axis refers to the uniform (average) background field strength.

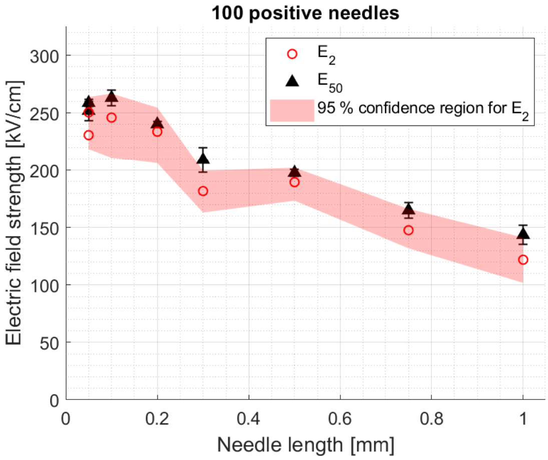

Figure 6.30: E_2 values of the positive 100 needles distribution, with the 95 % confidence region for E_2 as the shaded red region. Compared with the E_{50} as black symbols. Note: x-axis stops at 1 mm compared to 1 and 20 needles that continues to 2 mm. The y-axis refers to the uniform (average) background field strength.

As seen in Figures 6.29 and 6.30 was that the E_2 follows the shape of the distributions. It was also possible to see from the plots how steep each distribution was, the smaller the difference between E_{50} and E_2 the steeper the distribution. The plots also gave indications on how confident the estimates for E_2 were, the narrower the width of the confidence band, the smaller range for the 95 % confidence region of E_2.

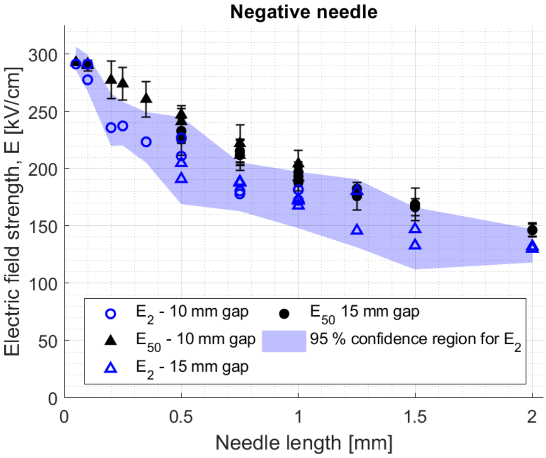

Figure 6.31: E_2 values of the negative single needle distribution, with the 95 % confidence region for E_2 as the shaded blue region. At needle lengths with several results, the maximum and minimum value was used for the 95 % confidence region. Compared with the E_{50} as black symbols. The y-axis refers to the uniform (average) background field strength.

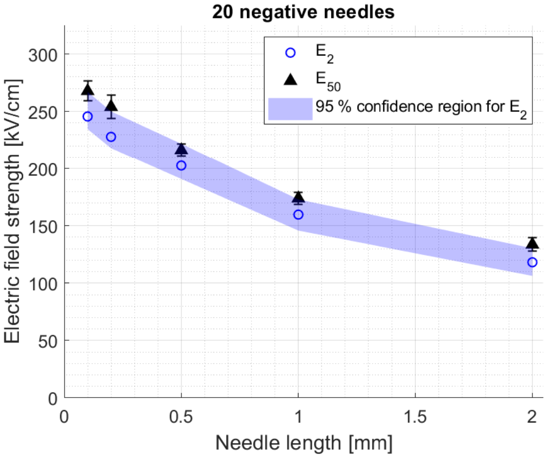

Figure 6.32: E_2 values of the negative 20 needles distribution, with the 95 % confidence region for E_2 as the shaded blue region. Compared with the E_{50} as black symbols. The y-axis refers to the uniform (average) background field strength.

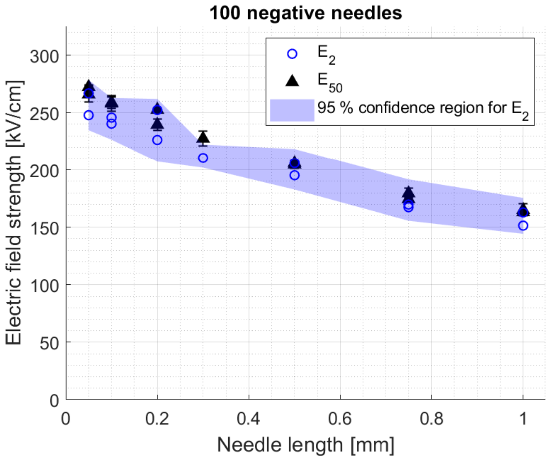

Figure 6.33: E_2 values of the negative 100 needles distribution, with the 95 % confidence region for E_2 as the shaded blue region. Compared with the E_{50} as black symbols. Note x-axis stops at 1 mm compared to 1 and 20 needles that continues to 2 mm. The y-axis refers to the uniform (average) background field strength.

6.9.2 CO_2

The E_2 was found for the results of positive needles in CO_2 shown in Figures 6.34, 6.35 and 6.36. Similarly, the E_2 followed the results of the E_{50}. The figures also showed, that for the most part, the confidence bands of positive needles, did not cover the E_{50}, something the confidence bands did quite often in SF_6. This was a difference, which might show that the relative slope of positive breakdowns in SF_6 and CO_2 were different. It might indicate that different or additional processes were involved in the breakdowns in the two gases.

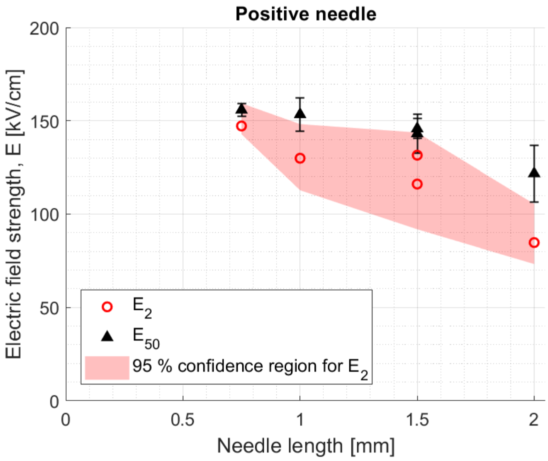

Figure 6.34: E_2 values of the positive single needle distribution, with the 95 % confidence region for E_2 as the shaded red region. At needle lengths with several results, the maximum and minimum value was used for the 95 % confidence region. Compared with the E_{50} as black symbols. The y-axis refers to the uniform (average) background field strength.

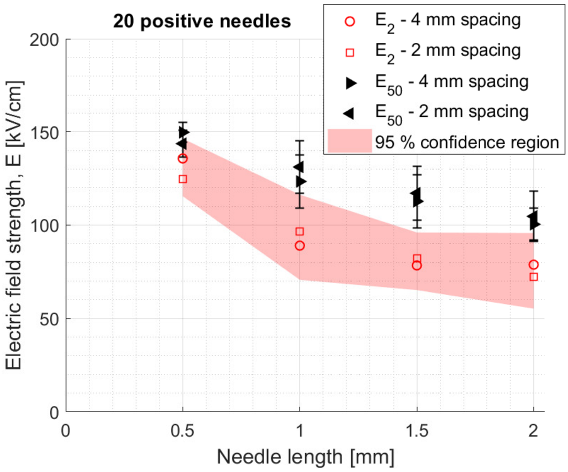

Figure 6.35: E_2 values of the positive 20 needles distribution, with the 95 % confidence region for E_2 as the shaded red region. At needle lengths with several results, the maximum and minimum value was used for the 95 % confidence region. Compared with the E_{50} as black symbols. The y-axis refers to the uniform (average) background field strength.

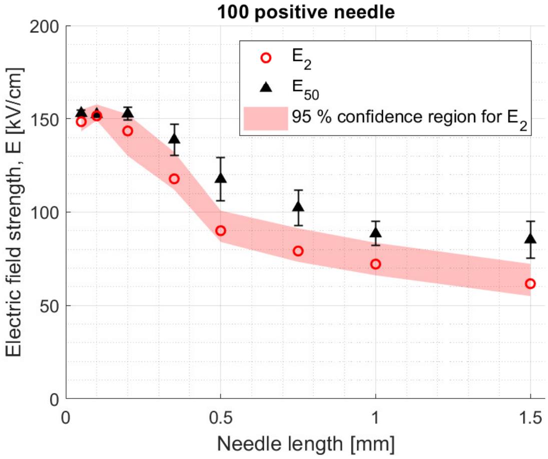

Figure 6.36: E_2 values of the positive 100 needles distribution, with the 95 % confidence region for E_2 as the shaded red region. At needle lengths with several results, the maximum and minimum value was used for the 95 % confidence region. Compared with the E_{50} as black symbols.Note: x-axis stops at 1.5 mm compared to 1 and 20 needles that continues to 2 mm. The y-axis refers to the uniform (average) background field strength.

An interesting observation for the E_2 value of a single negative needle in CO_2, see Figure 6.37, was that even if there was a change in the E_{50} of all the results, the E_2 remained constant. The large difference between E_{50} and E_2 indicated that the *breakdown region* for a single negative needle was quite large between 0.5 and 1 mm needle lengths. The E_2 result at 1 mm negative needle (at 62.72 kV/cm), was most likely too low considering the streamer crossing (at 69 kV/cm [40]) as the physical limitation for breakdowns. Implementing this limit would raise the E_2, as it was a result of the distribution function and the zero position of the Weibull distribution.

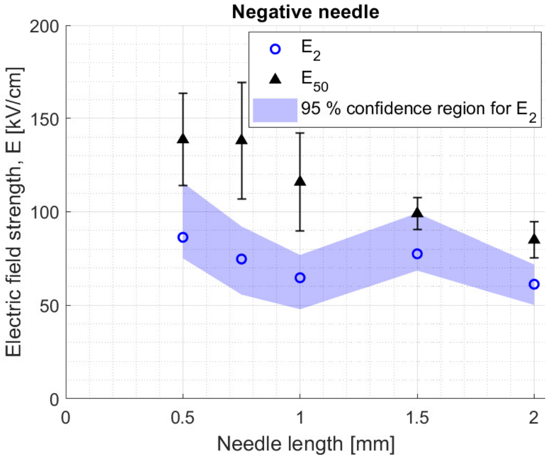

Figure 6.37: E_2 values of the negative single needle distribution, with the 95 % confidence region for E_2 as the shaded blue region. At needle lengths with several results, the maximum and minimum value was used for the 95 % confidence region. Compared with the E_{50} as black symbols. The y-axis refers to the uniform (average) background field strength.

From Figure 6.38, one can see that the distributions become steeper, as the difference between E_{50} and E_2 was smaller than for single needle when 20 needles were used.

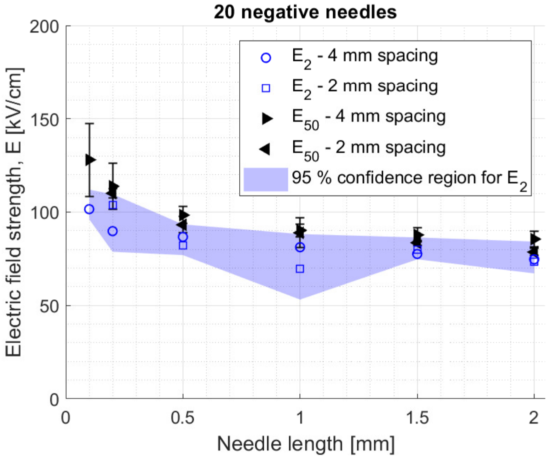

Figure 6.38: E_2 values of the negative 20 needles distribution, with the 95 % confidence region for E_2 as the shaded blue region. Compared with the E_{50} as black symbols. The y-axis refers to the uniform (average) background field strength.

For the 100 needles the E_2 indicated very steep distributions, and a very small confidence region for E_2. This indicates that the E_{50} and E_2 were very close to a physical breakdown limit at streamer crossing and streamer to spark transition. This follows from the enlargement law how distributions become very steep when are closed the zero position.

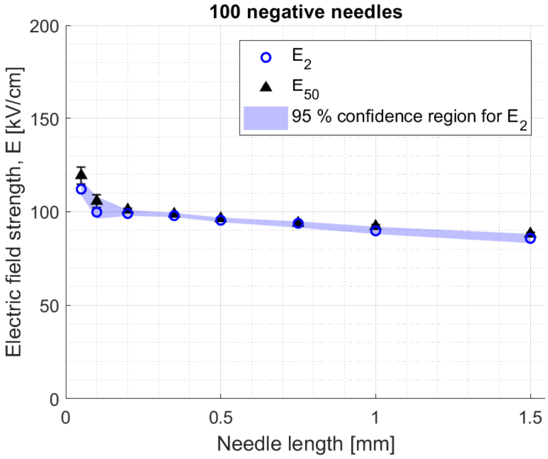

Figure 6.39: E_2 values of the negative 100 needles distribution, with the 95 % confidence region for E_2 as the shaded blue region. Compared with the E_{50} as black symbols. Note x-axis stops at 1.5 mm compared to 1 and 20 needles that continues to 2 mm. The y-axis refers to the uniform (average) background field strength.

Comparing the E_{50} and E_2 for positive and negative polarity for 100 needles, Figure 6.40, showed the different behavior of the polarities. Where the E_{50} of positive polarity becomes lower and becomes similar to the negative polarity around 1 mm needles. E_2 has a *crossover* around 0.5 mm and positive polarity becomes lower than negative polarity earlier, Which was of importance from a withstand perspective. Another observation was that the confidence region of the E_2 value was larger for positive polarity than for negative, which indicate that the region where both breakdowns and holds occur was larger for positive polarity.

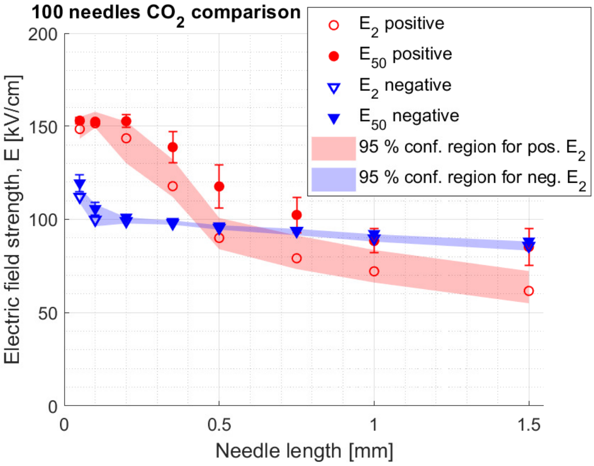

Figure 6.40: Comparison of E_{50} and E_2 for the two polarities with 100 needles in CO_2. With the confidence regions shaded. The y-axis refers to the uniform (average) background field strength.

6.9.3 Difference between E_{50} and E_2

The difference between E_{50} and E_2 where presented as number of standard deviations, σ, see Figure 6.41. The difference between E_{50} and E_2 was around 2.5 times the standard deviation, excluding the few low values, which was quite different from what is proposed by Küchler [48]. 2.5 times the standard deviation for the normal distribution would be in the range of 0.621 % probability. Similar observations was made for the difference in CO_2 as well, shown in Figure 6.42. For the most part the distance was around 2.5 times the standard deviation, but there were some outliers for negative polarity which are have lower distances. Considering Figure 6.4, the comparison show that the E_{50} standard deviation of the two distributions were similar. but from the 2 % probability of the three parameter Weibull distribution had a greater difference from the E_{50} than what the E_2 did for the Normal distribution. Thus, the explanation for this different behavior from the normal distribution was a result of the Weibull distribution. However, as the Weibull distribution is an asymmetric distribution, it should be investigated how the different parameters of the Weibull distribution affects the difference between E_{50} and E_2 (given in number of standard deviations) or if 2.5 times the standaard deviation was a valid approximation.

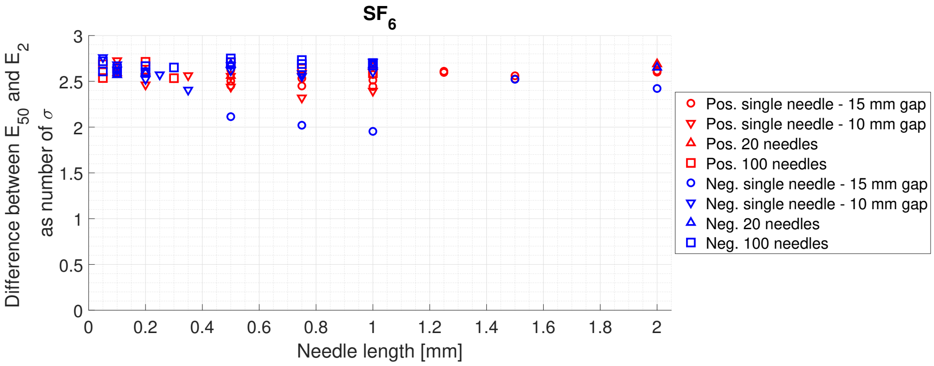

Figure 6.41: The difference between E_{50} and E_2 given as a number of sigma for each test performed for all needles in SF_6.

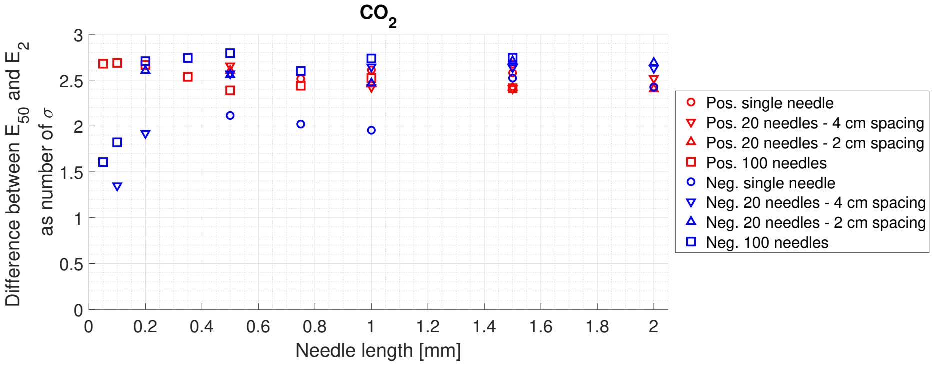

Figure 6.42: The difference between E_{50} and E_2 given as a number of sigma for each test performed for all needles in CO_2.

6.10 Leader and Streamer Observations

In the photographs taken during the experiments, parallel breakdowns paths were observed quite often as shown in Figures 6.43 and 6.44. The hypothesis about these parallel breakdowns were that they occur simultaneously.

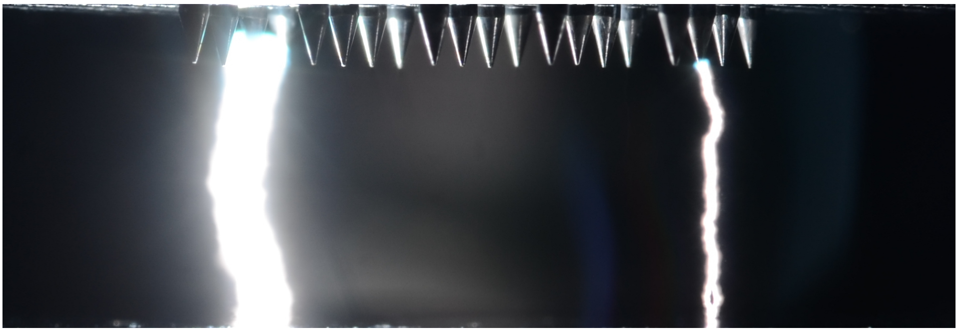

Figure 6.43: 20 needles at 2 mm and positive polarity in SF_6.

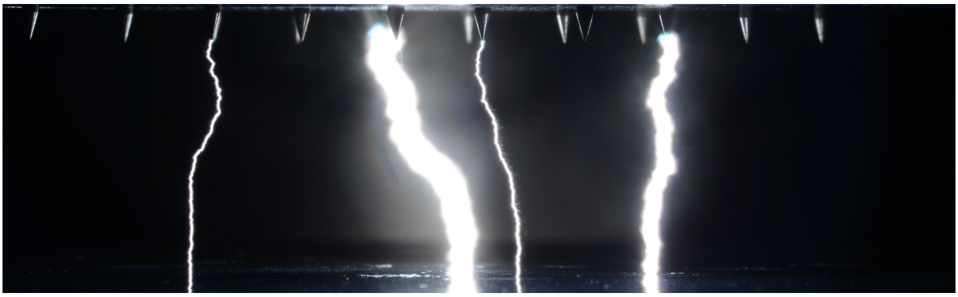

Figure 6.44: 16 needles at 2 mm and positive polarity in SF_6.

What was also seen, was that the light from the main breakdown channel illuminated channels where leader development had occurred, but not fully crossed the gap before the main breakdown channel crossed and form a spark, known as arrested discharges. They were visible because the leader formation heated up the gas and created a different gas density which then refracted the light differently than the colder surrounding gas. Shown for positive in Figure 6.45 and negative polarity in Figure 6.47. These pictures could be considered as a type of *shadowgraphy*, where the reflection of the main breakdown channel behaved as the background light source. An example of how shadowgraphy have been used in scientific work can be found in [93].

Figure 6.45: Positive leader channel with 0.5 mm needles in SF_6. Enhanced with "sharpen effect" to better show the details.

Figure 6.45 shows stepped leader propagation in positive polarity. Figure 6.46 showed how the main breakdown channel formed along all the branches in a positive leader. Figure 6.47 showed negative leader channels in SF_6 forming from the needle tips. Figures 6.45 and 6.47 show streamers feeding into the leader channels also increased the temperature of the gas near the tip of each leader branch.

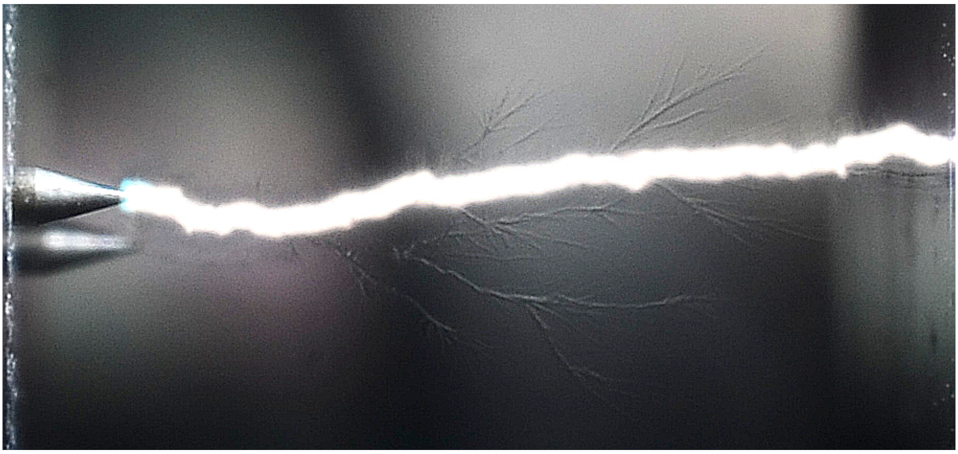

Figure 6.46: Positive leader in SF_6 with 2 mm needle, showing main breakdown plasma channel and leader branches from the main channel.

Figure 6.47: Negative leader channels with 1 mm needles in SF_6. Enhanced with ”sharpen effect” to better show the details.

In CO_2 leader channels was observed with less frequency and the ones that was observed had different structures than the ones seen in SF_6, see Figure 6.48. This might also be a streamer to spark channel, due to the interpretation of the E_{50} at 0.1 mm length at positive polarity.

Figure 6.48: Leader or streamer channel with 100 positive needles at 0.1 mm lengths in CO_2.

With negative polarity of the needles in CO_2, heated channels causing density differences occurred more frequently, see Figure 6.49. This picture showed that each needle had initiated a breakdown channel, which heated up. Many of the channels crossed the gap, but they did not cause the main breakdown channel. At this needle length, the channels might be streamers, leaders or a mixtures of both. However, it was believed that it was streamer crossing and streamer to spark transition which were decisive for breakdowns at 0.5 mm needle length and negative polarity. Further investigation should be done to see if and potentially how much secondary streamers are able to heat up the gas. It could be interesting to investigate how parallel breakdown channels, like seen in Figure 6.49, behave and interact with each other. If parallel streamers can merge and heat one common channel.

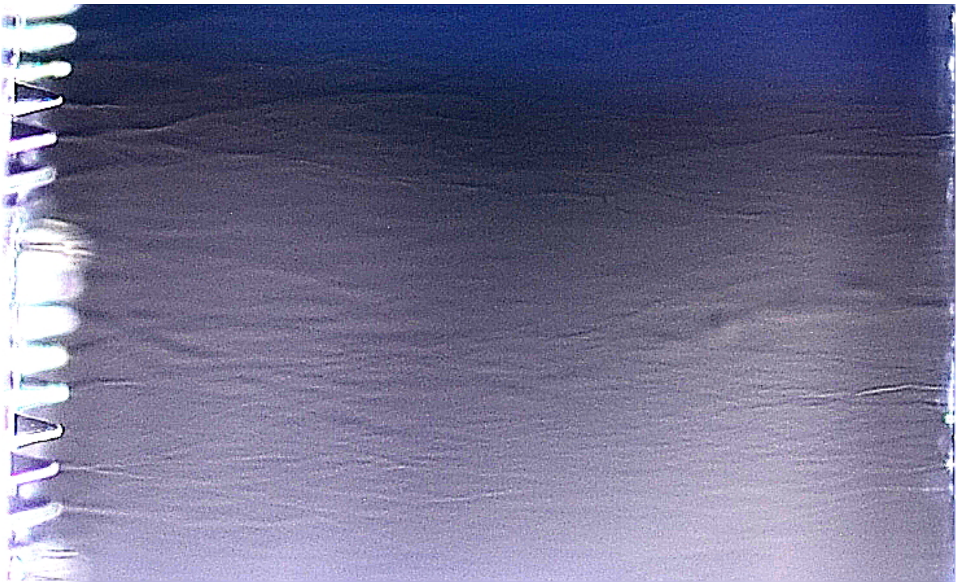

Figure 6.49: Heated channels at negative polarity in CO_2 with 100 needles at 0.5 mm length

Similarly to what is seen in Figure 6.48 in CO_2, other partly crossing illuminating channels were observed as shown for negative polarity in SF_6 in Figure 6.50.

Figure 6.50: Partly illuminated Leader or streamer channel in SF_6 for 20 needles at negative polarity.

These partly illuminated channels were observed more frequently in CO_2, shown in Figures 6.51 and 6.52 for negative polarity. Figure 6.53 show the same in positive polarity. A polarity difference was seen here, where negative polarity had straighter channels, while positive polarity branched more.

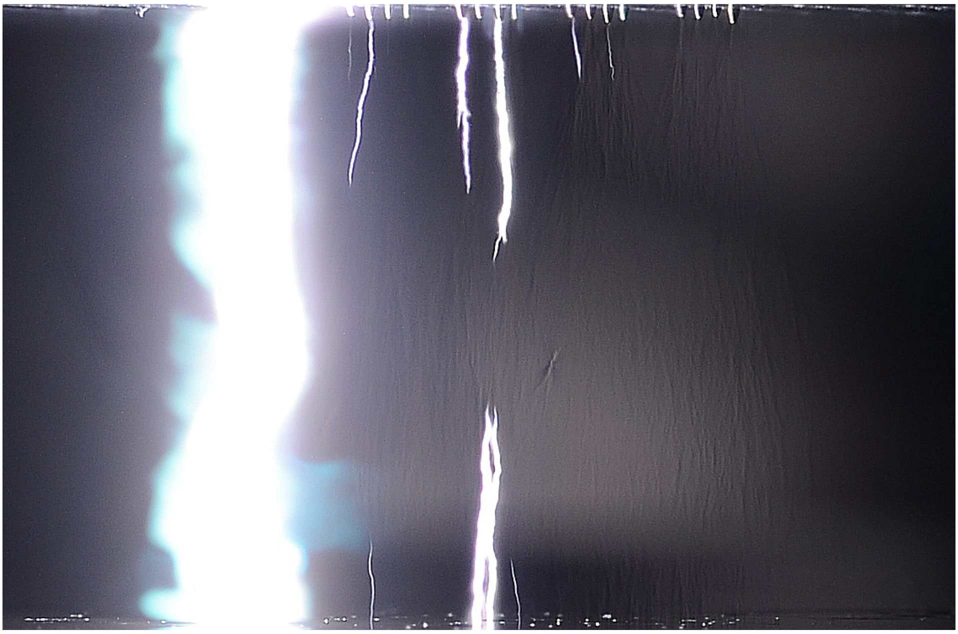

Figure 6.51: 20 needles at 0.2 mm and negative polarity in CO_2

Figure 6.52 showed how parts of the channel was illuminated in the middle of the gap, without a continuous luminous channel. I.e. heating of the channel occurred locally until it emitted enough light to be captured with the camera, without the streamer to spark transition occurring.

Figure 6.52: 20 needles at 1.0 mm and negative polarity in CO_2

Figure 6.53: 20 needles at 0.5 mm and positive polarity in CO_2

Similar behavior was seen with rough surfaces as well, as Figures 6.54 and 6.55 show for negative polarity of the plug in SF_6.

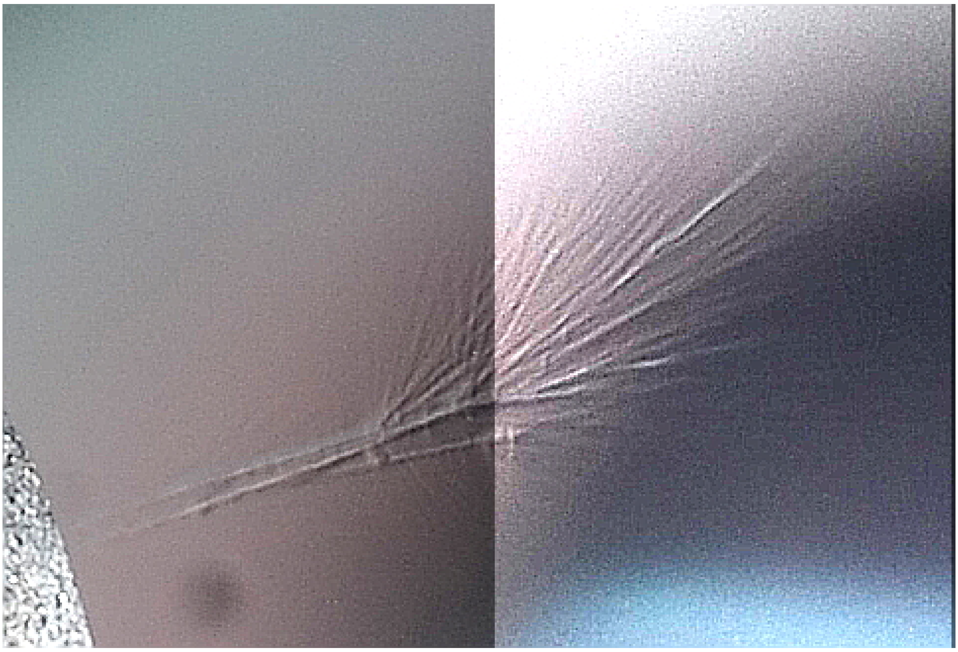

Figure 6.54: Negative polarity of the rough surface plug in SF_6. Roughly each half has been edited with different brightness and contrast to better show the two parallel channels.

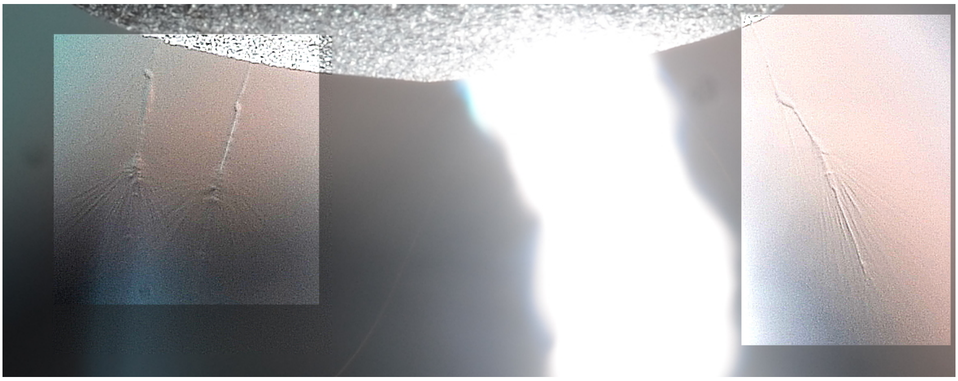

Figure 6.55: Multiple breakdown channels in the brighter areas of the picture in SF_6 with negative polarity on the plug.

Heated channels were not observed with positive polarity for the rough surfaces in SF_6 or in CO_2. It was possible that the heating was stronger for positive polarity and the channels could not *die* out before crossing the gap, causing breakdowns. However, illuminating channels were observed for both polarities in CO_2, see Figures 6.56 and 6.57.

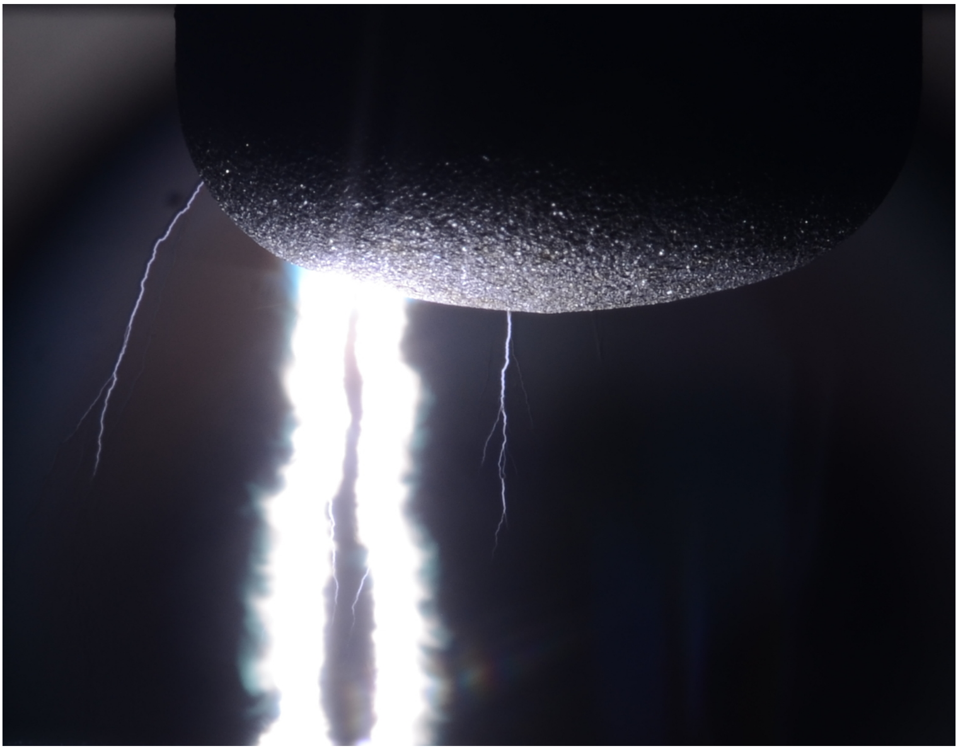

Figure 6.56: Positive plug polarity in CO_2

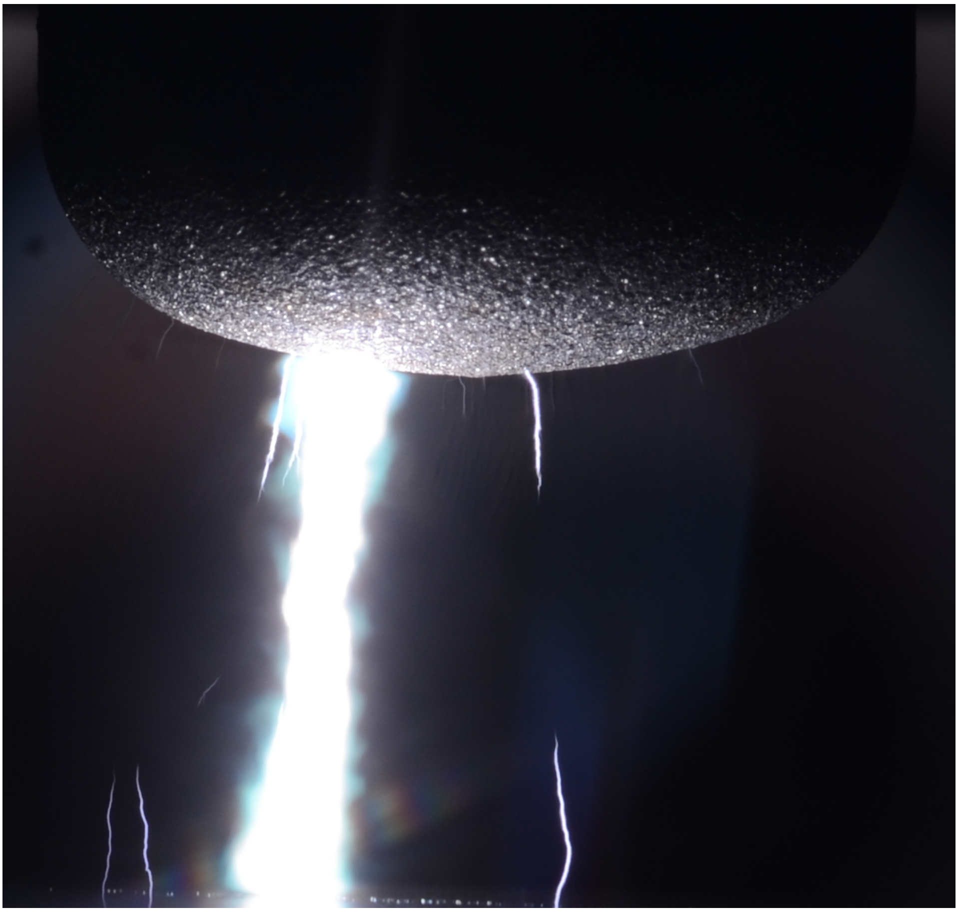

Figure 6.57: Negative plug polarity in CO_2

These pictures showed that at both polarities, multiple breakdown channels start when there were sufficient with first electrons. Then there was a *race* to cross the gap and become the main breakdown channel. It was also surprising that this could happen in the short time scale from the impulse was applied to the breakdown of the voltage was recorded with the scope. The channels that were slightly illuminating, as seen in Figure 6.57, were more frequent at negative polarity, which most likely was linked with there being no lack of first electron for this polarity. One could use these pictures to determine channel properties after complete heating of the gas, e.g. radius, propagation angles etc. Which was not done in this thesis. Appendix C show more interesting pictures, without any added commentary.

6.11 Very fast breakdowns and Displacement currents

It was observed that when the Van de Graaff generator was charged to too high voltages, compared to what the E_{50} of the gap and needles were. A significantly lower voltage was measured by the scope with breakdowns at times much faster than the rise time of the voltage impulse. Typically a voltage would be recorded as 9 kV, when the 50 $\%$ breakdown voltage of the gap was 200 kV. When the pictures of the tests were investigated, similar photographs to what is shown in Figure 6.58. These were explained with the steep rise time of the voltage impulse and the high voltage combined which created large displacement currents, $I = dU/dt$. This moved the test into similar areas as very fast transients in GIS (VFT). With actual lightning, this might occur, but the aim of the thesis was to find the equivalent to standard test lightning impulse voltages, these very fast breakdowns were discarded for the evaluation when they were observed. It was believed that most of these breakdown channels occurred simultaneously, but since the photographs were taken with a long exposure time, one would need a high speed camera with frame speeds in the nanoseconds range to verify this hypothesis.

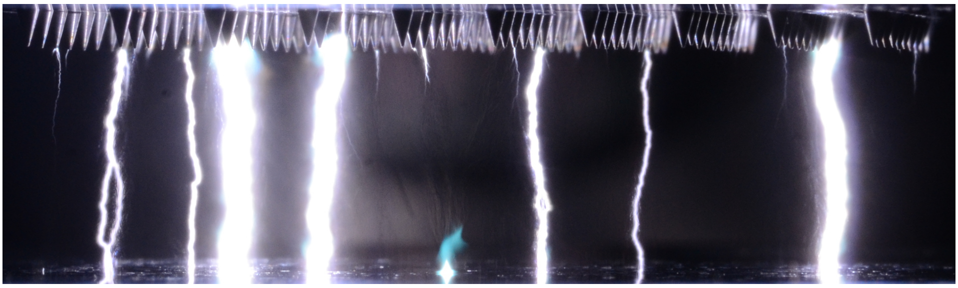

Figure 6.58: Parallel breakdowns occurring when a too high voltage was applied to the gap in CO_2 with 100 1.5 mm needles at positive polarity.

6.12 Areas of Improvement

The following section will go through the potential error sources of the experiment and post processing.

6.12.1 Dust Contamination of the Pressure Vessel

One thing that could have been improved was the amount of dust within the pressure chamber. The dust fibres were reduced as the cleaning method changed, but still there was dust contamination. For shorter needle lengths this made breakdowns occur other places than at the needles. However, this is the case in real equipment, and the cost of having a dust free environment would be too high for pragmatic work and equipment.

6.12.2 Uncertainty of Needle Lengths

There were uncertainties with the actual lengths of the needles, and to keep the plots ”clean” these were not plotted in any figures. For single needle the method of determining the length and the precision of the motor and the camera, gave an uncertainty in the range 10-20 μm. For the multiple needle setup, there was a noticeable difference in needle lengths for all the needles. As the measured distance from homing for the shortest and longest needle was measured was up to 0.2 mm in distance, for the worst case. Giving a maximum uncertainty of the actual length of +/- 0.1 mm, which was quite significant for the short needle lengths. However, with the setup and needles that were used, this was the best that could be done. More precision would require more time and would be more expensive. As shown, the average of the first and last needle was not a very bad estimate of the actual average of the 20 needles, as explained in Section 4.3.2. A consequence of having the uncertainty for the multiple needles, was that for the shorter needle lengths of 0.05 and 0.1, there were likely some needles that had not emerged from the plate. Making the effective number of needles lower than 20 or 100. An expectation while performing the experiments was that the longer needles would have a majority of breakdowns which would erode them over the tests series, reducing the uncertainty. One thing that could be tested was how multiple needles at different lengths behave compared to the same number of needles with exactly the same length as the average of the different needles.

Another issue was erosion of the needles. From optical investigations, it was evident that each breakdown eroded off a small part of the needle tip, as can be seen in the comparison of a new and worn needle after 800+ (estimated due to too many to count) of breakdowns at the needle in Figure 6.59. The observation was that the needles melt closer and closer to hemispherical shapes from the original conical shape. The change per breakdown and per series was small, which gives an additional uncertainty to each test series, but it was considered negligible. After the early tests, the needles were changed with a higher frequency.

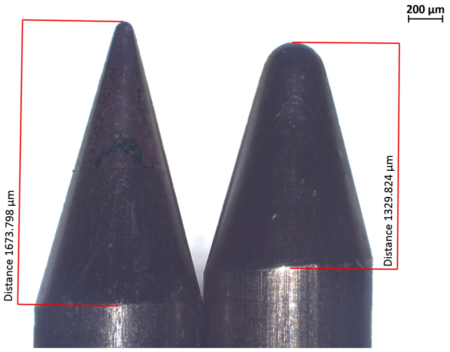

Figure 6.59: Comparison of a new needle to the left and a worn needle to the right

The reduction of the field enhancement of the needle depending on the tip was simulated and shown in Figure 6.60. The Figure show the electric field strength of the needle for a needle with a similar tip radius of 33 μm to the actual needles and a rounded needle with a radius of 130 μm. It showed a quite significant difference in the first 70 μm from the needle tip. A tip radius of 130 μm was probably of the more extreme used, but illustrates the differences when the needles were worn. It should be investigated how much the actual behavior of different needle shapes influenced the breakdown field strengths.

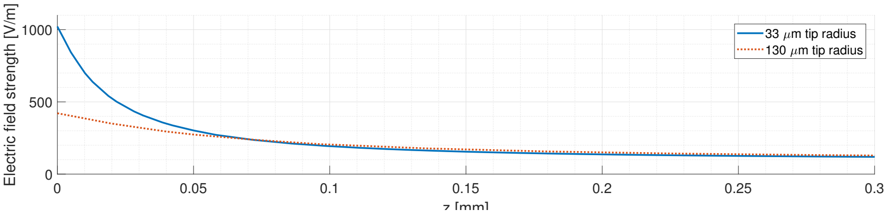

Figure 6.60: Comparison of the field strength of a similar to the real needle with a tip radius of 33 μm compared with the field enhancement of a very rounded needle with a tip radius of 130 μm.

6.12.3 Theoretical Streamer Inception Calculations

For the simulations and calculations of streamer inception, the *worst case* field was used, which should give a lower streamer inception estimation. As the results for 100 needles in CO_2 showed that the results were below the theoretical of the streamer inception field strengths. This could be due to uncertainties in the needle lengths, in the fit function of the effective ionization coefficient α_{eff} or in the COMSOL simulations. To adjust for this the value for the theoretical streamer inception field for fitting the three parameter Weibull distribution was set to 90 $\%$ of the theoretical calculated value.

6.12.4 Self-Consistency of the Turnbull Algorithm and Bootstrap

As part of creating the three-parameter Weibull fit and confidence bands, the Turnbull algorithm was given a self-consistency limit of $1 \cdot 10^{-5}$. Which should be small enough, but requires further investigation for certainty. Similarly, the number of bootstrap iterations was set to 1000. This should probably be closer to 5 000 or 10 000 to give proper confidence bands. But was kept low to save time due to the bootstrap being a quite time consuming algorithm.

6.13 Future Work

Some suggestions to continuation have been presented throughout the discussion. In the following some additional suggestions for future work based on observations made in this thesis will be presented.

An interesting thing to determine with this, or a similar setup, if there are several protrusions with different lengths, which one will dominate the statistics. Even though there were slight length differences, the idea was to test e.g. a single 1 mm protrusion with 100, 0.5 mm (or smaller) protrusions. In theory the breakdown distribution should be the combined distribution of all the protrusions. The interesting thing would be to see if the multiple small protrusions or if the larger protrusion dominate.

There are not only the Weibull or the Normal distributions which have been used for describing and fitting dielectric performance of insulation. The three parameter Weibull was a good fit, especially considering that it has a zero value, something the normal distribution does not. Which can be argued that breakdowns have a physical lower limit as well. Future investigations should look into other alternatives. Previous work has used distribution functions like the double exponential distribution function [12]. An interesting distribution which the author would have liked to investigate was the Generalized Extreme Value (GEV) distribution. This was used by Peppas et al to investigate the breakdown performance of nanofluids [94]. The GEV combines the Fréchet, Gumbel and Weibull distribution. Peppas et al found that this their results followed the Weibull distribution and GEV better than the Gumbel or normal distribution [94]. For that reason the GEV could be interesting to investigate for breakdowns in gas.

Considering the behavior of the distribution functions more work should be put into evaluation of how good they fit the data. One method that should be considered is using the Kolmogorov–Smirnov as done by Given et al [95] or the Anderson–Darling statistic as done by [94], and possible other tests, something that was not done in this thesis.

For the work done with the surfaces, only two surfaces areas and one degree of roughness were considered. Due to the behavior of the the breakdown field strength of the plugs compared with the Rogowski and the predictions. More surfaces areas should be tested along with more degrees of roughness. One should also try to get a better idea of the peak density and better data on how the peaks were distributed along the surfaces to see if there are differences affecting the scaling that can be explained.

Chapter 7

Conclusion

The results obtained in the experimental work show that both SF_6 and CO_2 were sensitive to the needle protrusions, where SF_6 was more sensitive than CO_2. Increasing the number of needles in SF_6 to 20 and 100 gave a non-linear decrease of the breakdown field strengths where it seemed to reach a saturation already at 20 needles, as there was no significant further decrease when increasing to 100 needles. For negative polarity there was a non-linear decrease as well with an increasing number of needles.

In CO_2, the breakdown behavior did not show any influence from the single needle at positive polarity at lengths lower than 1 mm where the breakdown field was at the critical field in CO_2. At lengths longer than 1 mm, there was a decrease from the critical field which was explained by positive leader mechanism for the single positive needle. Increasing the number of needles caused the breakdown field strengths decrease for, as for SF_6, non-linearly for positive polarity. For negative polarity, there was not much impact at needle lengths lower than 0.75 mm from the critical field in CO_2. At needle lengths larger than 0.75 mm, the breakdown field strength decreased to a level slightly above negative streamer crossing for the 2 mm needle. When increasing the number of needles to 20 and 100 needles, there was no significant difference. The breakdown field strengths decreased along the theoretical streamer inception and saturated at a level above negative streamer crossing at 0.2-0.5 mm. This was explained with the streamer crossing and spark transition field strength for negative polarity in CO_2. Thus the negative breakdown characteristic was determined by streamer inception, streamer crossing and streamer to spark transition at 6 bar. The big scatter of the 0.5, 0.75 and 1 mm lengths for single needle at negative polarity, could be a result of the lack of time for streamer to spark transition when lightning impulse voltages were applied. The obtained results should be a good reference for the design purposes when using protrusion fields as design criteria.

There was a significant decrease of the results for the breakdown field strengths when using real surface roughness for positive polarity in SF_6 and both polarities in CO_2. For negative polarity in SF_6, there was a slight decrease in the breakdown field strength.

The attempt to predict the results based on the distributions show that the (simplified) enlargement law for predictions must be used with care when designing equipment. The enlargement law cannot be applied to every situation and expected to give the correct prediction. The enlargement law assumes the enlarged distribution to be a combination of identical distributions. It does not consider that the different statistical processes involved. To get a good prediction one would need to isolate the distributions of each individual process, i.e. first electron, streamer crossing, spark formation. Then enlarge them separately before combining them. The enlargement law does not consider physical limitations, unless they were put in as the zero point for the distribution. As the results for negative needles in CO_2 indicated, with a lower limit at negative streamer crossing for negative polarity in the tested protrusion range. It was expected at longer needle lengths than 2 mm, negative leaders could also be decisive.

While the results showed that the predictions fit well with negative polarity for the needle protrusions and the negative surfaces in SF_6, the enlargement law should be carefully used for negative polarity unless how far it can be scaled becomes determined.

Bibliography

[1] N. Konrad, "Einige beobachtungen über den durchgang der electricität durch gase und dämpfe," *Annalen der Physik*, vol. 274, no. 12, pp. 663–672. [Online]. Available: https://onlinelibrary.wiley.com/doi/abs/10.1002/andp.18892741210

[2] M. Rabie and C. M. Franck, "Assessment of Eco-friendly Gases for Electrical Insulation to Replace the Most Potent Industrial Greenhouse Gas SF_6," *Environmental Science & Technology*, vol. 52, no. 2, pp. 369–380, 2018, pMID: 29236468. [Online]. Available: https://doi.org/10.1021/acs.est.7b03465

[3] V. Grosse, "Lichtbogenlöschmittel für elektrische apparate. german patent," Patent 977 250, 1938.

[4] M. Maiss and C. A. M. Brenninkmeijer, "Atmospheric SF_6: Trends, sources, and prospects," *Environmental Science & Technology*, vol. 32, no. 20, pp. 3077–3086, 1998. [Online]. Available: https://doi.org/10.1021/es9802807

[5] M. Seeger, "Perspectives on research on high voltage gas circuit breakers," *Plasma Chemistry and Plasma Processing*, vol. 35, no. 3, pp. 527–541, May 2015. [Online]. Available: https://doi.org/10.1007/s11090-014-9595-4

[6] M. Bujotzek and M. Seeger, "Parameter dependence of gaseous insulation in SF_6," *IEEE Transactions on Dielectrics and Electrical Insulation*, vol. 20, no. 3, pp. 845–855, June 2013.

[7] M. Seeger, L. Niemeyer, and M. Bujotzek, "Leader propagation in uniform background fields in SF_6," *Journal of Physics D: Applied Physics*, vol. 42, no. 18, p. 185205, sep 2009.

[8] U. N. F. C. on Climate Change. (1995) Global warming potentials. [Accessed: April 13, 2018]. [Online]. Available: https://unfccc.int/ghg_data/items/3825.php

[9] G. Mazzanti, G. Stomeo, and S. Mancini, "State of the art in insulation of gas insulated substations: main issues, achievements, and trends," *IEEE Electrical Insulation Magazine*, vol. 32, no. 5, pp. 18–31, September 2016.

[10] M. Seeger, P. Stoller, and A. Garyfallos, "Breakdown fields in synthetic air, CO_2, a CO_2/O_2 mixture, and CF_4," *IEEE Transactions on Dielectrics and Electrical Insulation*, vol. 24, no. 3, pp. 1582–1591, jun 2017. [Online]. Available: http://ieeexplore.ieee.org/document/7962048/

[11] ABB AB, "LTA - CO_2 high voltage circuit breaker - enhancing eco-efficiency," 2014. [Online]. Available: https://library.e.abb.com/public/929e0d91615171fdc1257ddb003725fb/LTA$%$20Enhancing$%$20eco-efficiency.pdf

[12] W. Hauschild and W. Mosch, *Statistical techniques for high-voltage engineering*, ser. IEE power series. London: Peter Peregrinus on behalf of the Institution of Electrical Engineers, 1992, vol. 13.

[13] W. Mosch and W. Hauschild, *Hochspannungsisolierungen mit Schwefelhexafluorid*. Heidelberg: Dr. Alfred Hütig Verlag, 1979.

[14] X. Li, H. Zhao, and A. B. Murphy, "SF_6 -alternative gases for application in gas-insulated switchgear," *Journal of Physics D: Applied Physics*, vol. 51, no. 15, p. 153001, 2018. [Online]. Available: http://stacks.iop.org/0022-3727/51/i=15/a=153001

[15] M. Seeger et al, "CIGRE Reference Paper on Recent development of alternative gases to SF_6 for switching applications," *Electra*, no. 291, pp. 26–29, April 2017.

[16] T. Nitta, N. Yamada, and Y. Fujiwara, "Area effect of electrical breakdown in compressed SF_6," *IEEE Transactions on Power Apparatus and Systems*, vol. PAS-93, no. 2, pp. 623–629, March 1974.

[17] A. Pedersen, "Limitations of breakdown voltages in SF_6 caused by electrode surface roughness," in *Conference on Electrical Insulation & Dielectric Phenomena - Annual Report 1974*. IEEE, oct 1974, pp. 457–464.

[18] A. Pedersen, P. W. Karlsson, E. Bregnsbo, and T. M. Nielsen, "Anomalous breakdown in uniform field gaps in SF_6," *IEEE Transactions on Power Apparatus and Systems*, vol. PAS-93, no. 6, pp. 1820–1826, Nov 1974.

[19] S. Berger, "Onset or breakdown voltage reduction by electrode surface roughness in air and SF_6," *IEEE Transactions on Power Apparatus and Systems*, vol. 95, no. 4, pp. 1073–1079, July 1976.

[20] I. W. McAllister, "A multiple protrusion model for surface roughness effects in compressed SF_6," *Elektrotechnische Zeitschrift A*, vol. 99, pp. 283–284, 1978.

[21] B. H. Crichton, D. I. Lee, and D. J. Tedford, "Prebreakdown in Compressed SF_6 and SF_6/N_2 Mixtures in Projection Perturbed Uniform Fields," in *4th International Conference on Gas Discharges*, no. 143. IEE Conference Publication, 1976, pp. 199–202.

[22] I. Bortnik, M. Ierusalimov, V. Borin, V. Varivodov, V. Vertikov, O. Ilenko, and Y. Kuz'mina, "Evaluation of the requirements on the surface finish of electrodes in SF_6 insulation." *Electric Technology U.S.S.R*, no. 4, pp. 43–49, Jan. 1985.

[23] Y. Oiu, R. Li, E. Kuffel, and M. Liu, "Effect of electrode surface roughness on breakdown of SF_6 gas insulation," in *Conference Record of the 1988 IEEE International Symposium on Electrical Insulation*. IEEE, 1988, pp. 93–96. [Online]. Available: http://ieeexplore.ieee.org/document/13875/

[24] R. Li and Y. Qiu, "A new multi-ridge model for electrode surface roughness effect in SF_6," in *Proceedings., Second International Conference on Properties and Applications of Dielectric Materials*, Sep 1988, pp. 105–108 vol.1.

[25] S. M. El-Makkawy, "Electrode surface roughness initiated breakdown in compressed SF_6 gas," in *Electrical Insulation and Dielectric Phenomena, 1994., IEEE 1994 Annual Report., Conference on*, Oct 1994, pp. 948–953.

[26] C. Lederle and J. Kindersberger, "The influence of surface roughness and coating on the impulse breakdown voltage in SF_6," in *The 17th Annual Meeting of the IEEE Lasers and Electro-Optics Society, 2004. LEOS 2004.*, Oct 2004, pp. 522–525.

[27] C. Lederle and J. Kindersberger, "The influence of surface roughness and dielectric coating on ac and dc breakdown voltage in SF_6," in *14th International Symposium on High Voltage Engineering*, Aug 2005, pp. 1–6.

[28] M. Seeger, L. Niemeyer, and M. Bujotzek, "Partial discharges and breakdown at protrusions in uniform background fields in SF_6," *Journal of Physics D: Applied Physics*, vol. 41, no. 18, p. 185204, sep 2008.

[29] D. R. Young, "Electric breakdown in CO_2 from low pressures to the liquid state," *Journal of Applied Physics*, vol. 21, no. 3, pp. 222–231, 1950. [Online]. Available: https://doi.org/10.1063/1.1699638

[30] K. P. Brand and J. Kopainsky, "Breakdown field strength of unitary attaching gases and gas mixtures," *Applied physics*, vol. 18, no. 4, pp. 321–333, Apr 1979. [Online]. Available: https://doi.org/10.1007/BF00899684

[31] M. Shiiki, M. Sato, M. Hanai, and K. Suzuki, *Dielectric Performance of CO_2 Gas Compared with N_2 Gas.* Boston, MA: Springer US, 2001, pp. 365–370. [Online]. Available: https://doi.org/10.1007/978-1-4615-0583-9_51

[32] T. Uchii, Y. Hoshina, T. Mori, H. Kawano, T. Nakamoto, and H. Mizoguchi, *Investigations on SF_6-Free Gas Circuit Breaker Adopting CO_2 Gas as an Alternative Arc-Quenching and Insulating Medium.* Boston, MA: Springer US, 2004, pp. 205–210. [Online]. Available: https://doi.org/10.1007/978-1-4419-8979-6_28

[33] K. Juhre and E. Kynast, "High pressure N_2, N_2/CO_2 and CO_2 gas insulation in comparison to SF_6 in GIS applications," in *Proceedings of the XIVth International Symposium on High Voltage Engineering*, Aug 2005.

[34] S. Meijer, J. J. Smit, and A. Girodet, "Comparison of the breakdown strength of N_2, CO_2 and SF_6 using the extended up-and-down method," in *2006 IEEE 8th International Conference on Properties applications of Dielectric Materials*.

[35] S. Okabe, H. Goshima, A. Tanimura, S. Tsuru, Y. Yaegashi, E. Fujie, and H. Okubo, "Fundamental insulation characteristic of high-pressure CO_2 gas under actual equipment conditions," *IEEE Transactions on Dielectrics and Electrical Insulation*, vol. 14, no. 1, pp. 83–90, Feb 2007.

[36] M. Hikita, S. Ohtsuka, N. Yokoyama, S. Okabe, and S. Kaneko, "Effect of electrode surface roughness and dielectric coating on breakdown characteristics of high pressure CO_2 and N_2 in a quasi-uniform electric field," *IEEE Transactions on Dielectrics and Electrical Insulation*, vol. 15, no. 1, pp. 243–250, February 2008.

[37] S. Ka, K. Inami, H. Hama, G. Ueta, J. Wada, and S. Okabe, “Lightning impulse and ac breakdown characteristics of CO_2 gas under quasi-uniform electric field using real-size gas-insulated switchgear model,” in *18th International Symposium on High Voltage Engineering*, Aug 2013, pp. 1549–1553.

[38] T. Yoshida, S. Ka, Y. Shimizu, K. Inami, H. Hama, G. Ueta, J. Wada, and S. Okabe, “Metallic particle motion and its sparkover property at AC voltages in N_2, CO_2, dry air and SF_6,” in *9th International Workshop on High Voltage Engineering (IWHV 2014)* , Nov. 2014.

[39] T. Yoshida, Y. Shimizu, K. Inami, H. Hama, G. Ueta, J. Wada, and S. Okabe, “Partial discharge and breakdown properties in N_2, CO_2, dry air and SF_6 initiated by metallic particles fixed on high voltage conductor and attached on spacer surface at ac voltages,” in *The 20th International Symposium on High Voltage Engineering* , Aug. 2017.

[40] M. Seeger, J. Avaheden, S. Pancheshnyi, and T. Votteler, “Streamer parameters and breakdown in CO_2,” *Journal of Physics D: Applied Physics*, vol. 50, no. 1, p. 015207, 2017.

[41] E. H. Cohen, “The electric strength of highly compressed gases,” *Proceedings of the IEE - Part A: Power Engineering*, vol. 103, pp. 57–68(11), February 1956. [Online]. Available: http://digital-library.theiet.org/content/journals/10.1049/pi-a.1956.0055

[42] T. Dunz, B. Fruth, L. Niemeyer, L. Ullrich, K. Diederich, and M. Hässig, “Electrical field on rough electrode surfaces and its influence on the statistical properties of SF_6 breakdown,” in *Proceedings of the 6th International Symposium of High Voltage Engineering*. ISH, 1989.

[43] H. Hama and S. Okabe, “Factors dominating dielectric performance of real-size gas insulated system and their measures by dielectric coatings in SF_6 and potential gases,” *IEEE Transactions on Dielectrics and Electrical Insulation*, vol. 20, no. 5, pp. 1737–1748, Oct 2013.

[44] M. Honda, H. Okubo, H. Aoyagi, and A. Inui, “Impulse breakdown characteristics of coated electrodes in SF_6 gas,” *IEEE Transactions on Power Delivery*, vol. 2, no. 3, pp. 699–708, July 1987.

[45] S. Menju, H. Aoyagi, K. Takahashi, and H. Qhno, “Dielectric breakdown of high pressure SF_6 in sphere and coaxial cylinder gaps,” *IEEE Transactions on Power Apparatus and Systems*, vol. PAS-93, no. 5, pp. 1706–1712, Sept 1974.

[46] H. Hama, K. Inami, T. Ootsuka, Y. Shimizu, E. Nagao, K. Oosumi, and M. Yoshimura, *Improvement of SF_6 Gas Insulation System by Applying Thick Dielectric-Layered Electrode and its Application to High Voltage Equipment*. Boston, MA: Springer US, 2004, pp. 319–328. [Online]. Available: https://doi.org/10.1007/978-1-4419-8979-6_44

[47] D. J. Whitehouse, *Surfaces and their measurement*. London: Kogan Page Science, 2002.

[48] A. Küchler, *High voltage engineering : Fundamentals - Technology - Applications*. Heidelberg: Springer Vieweg, 2017.

[49] Y. Zhang, J. Su, X. Qiu, R. Li, L. Zhao, J. Cheng, and B. Zeng, "Micro-effects of surface polishing treatment on microscopic field enhancement and long vacuum gap breakdown," *AIP Advances*, vol. 6, no. 9, p. 095103, 2016. [Online]. Available: https://doi.org/10.1063/1.4962549

[50] R. Arora and W. Mosch, *High Voltage Insulation Engineering*. New Delhi, India: New Age International Publishers, 2008.

[51] W. Schmidt and R. Van Brunt, "Comments on the effect of electron detachment in initiating breakdown in gaseous dielectrics," in *Gaseous Dielectrics III*. Pergamon, 1982, pp. 561 – 563.

[52] E. Kuffel, W. S. Zaengl, and J. Kuffel, *High Voltage Engineering Fundamentals*, 2nd ed. Oxford, MA, USA: Newnes, 2000.

[53] H. Z. Raether, "Die entwicklung der elektronenlawine in den funkenkanal," *Physik*, vol. 112, pp. 464–489, 1939.

[54] J. M. Meek, "A theory of spark discharge," *Phys. Rev.*, vol. 57, pp. 722–728, Apr 1940.

[55] V. Cooray, *The Lightning Flash*, 2nd ed. London, United Kingdom: The Institution of Engineering and Technology, 2014.

[56] E. Marode, "The mechanism of spark breakdown in air at atmospheric pressure between a positive point and a plane. i. experimental: Nature of the streamer track," *Journal of Applied Physics*, vol. 46, no. 5, pp. 2005–2015, 1975.

[57] E. Marode, "The mechanism of spark breakdown in air at atmospheric pressure between a positive point and plane. ii. theoretical: Computer simulation of the streamer track," *Journal of Applied Physics*, vol. 46, no. 5, pp. 2016–2020, 1975.

[58] E. Marode, F. Bastien, and M. Bakker, "A model of the streamer-induced spark formation based on neutral dynamics," *Journal of Applied Physics*, vol. 50, no. 1, pp. 140–146, 1979.

[59] G. V. Naidis, "Dynamics of streamer breakdown of short non-uniform air gaps," *Journal of Physics D: Applied Physics*, vol. 38, no. 21, p. 3889, 2005. [Online]. Available: http://stacks.iop.org/0022-3727/38/i=21/a=009

[60] A. Agnihotri, W. Hundsdorfer, and U. Ebert, "Modeling heat dominated electric breakdown in air, with adaptivity to electron or ion time scales," *Plasma Sources Science and Technology*, vol. 26, no. 9, p. 095003, 2017. [Online]. Available: http://stacks.iop.org/0963-0252/26/i=9/a=095003

[61] G. V. Naidis, "Simulation of streamer-to-spark transition in short non-uniform air gaps," *Journal of Physics D: Applied Physics*, vol. 32, no. 20, p. 2649, 1999. [Online]. Available: http://stacks.iop.org/0022-3727/32/i=20/a=311

[62] M. Cernak, E. M. van Veldhuizen, I. Morva, and W. R. Rutgers, “Effect of cathode surface properties on glow-to-arc transition in a short positive corona gap in ambient air,” *Journal of Physics D: Applied Physics*, vol. 28, no. 6, p. 1126, 1995. [Online]. Available: http://stacks.iop.org/0022-3727/28/i=6/a=015

[63] A. Larsson, “The effect of a large series resistance on the streamer-to-spark transition in dry air,” *Journal of Physics D: Applied Physics*, vol. 31, no. 9, p. 1100, 1998. [Online]. Available: http://stacks.iop.org/0022-3727/31/i=9/a=011

[64] I. Gallimberti and N. Wiegart, “Streamer and leader formation in SF_6 and SF_6 mixtures under positive impulse conditions. i. corona development,” *Journal of Physics D: Applied Physics*, vol. 19, no. 12, p. 2351, 1986.

[65] I. Gallimberti and N. Wiegart, “Streamer and leader formation in SF_6 and SF_6 mixtures under positive impulse conditions. ii. streamer to leader transition,” *Journal of Physics D: Applied Physics*, vol. 19, no. 12, p. 2363, 1986.

[66] L. Niemeyer, L. Ullrich, and N. Wiegart, “The mechanism of leader breakdown in electronegative gases,” *IEEE Transactions on Electrical Insulation*, vol. 24, no. 2, pp. 309–324, Apr 1989.

[67] H. E. Nechmi, A. Beroual, A. Girodet, and P. Vinson, “Fluoronitriles/CO_2 gas mixture as promising substitute to SF_6 for insulation in high voltage applications,” *IEEE Transactions on Dielectrics and Electrical Insulation*, vol. 23, no. 5, pp. 2587–2593, October 2016.

[68] D. Xiao, *Gas Discharge and Gas Insulation*, 1st ed., ser. Energy and Environment Research in China. Berlin Heidelberg: Springer-Verlag, 2016, vol. 6.

[69] Y. A. Safar, N. H. Malik, and A. H. Qureshi, “Impulse breakdown behavior of negative rod-plane gaps in SF_6-N_2, SF_6-Air and SF_6-$C0_2$ mixtures,” *IEEE Transactions on Electrical Insulation*, vol. EI-17, no. 5, pp. 441–450, Oct 1982.

[70] M. S. Bhalla and J. D. Craggs, “Measurement of ionization and attachment coefficients in carbon dioxide in uniform fields,” *Proceedings of the Physical Society*, vol. 76, no. 3, p. 369, 1960.

[71] T. Uchii, Y. Hoshina, H. Kawano, K. Suyuki, T. Nakamoto, and M. Toyoda, “Fundamental research on SF_6-free gas insulated switchgear adpoting CO_2 gas and its mixtures,” in *Proceedings of International Symposium on EcoTopia Science 2007, ISETS07 (2007)*, 2007.

[72] W. Wang and A. Bogaerts, “Effective ionisation coefficients and critical breakdown electric field of co_2 at elevated temperature: effect of excited states and ion kinetics,” *Plasma Sources Science and Technology*, vol. 25, no. 5, p. 055025, 2016. [Online]. Available: http://stacks.iop.org/0963-0252/25/i=5/a=055025

[73] D. K. Davies, “Ionization and attachment coefficients in CO_2:N_2:he and pure CO_2,” *Journal of Applied Physics*, vol. 49, no. 1, pp. 127–131, 1978. [Online]. Available: https://doi.org/10.1063/1.324332

[74] F. M. Dekking, *A Modern Introduction to Probability and Statistics : Understanding Why and How*, ser. Springer Texts in Statistics, 2005.

[75] Y. Dodge, *The Concise Encyclopedia of Statistics*, 1st ed., ser. Springer reference, 2008.

[76] W. Weibull, "A statistical distribution function of wide applicability," *Transactions of the American Society of Mechanical Engineers*, vol. 32, pp. 293–297, 1951.

[77] M. Abramowitz and I. A. Stegun, *Handbook of mathematical functions : with formulas, graphs, and mathematical tables*, ser. Dover books on mathematics. New York: Dover, 1965.

[78] H. Dai and H. Wang, *Analysis for time-to-event data under censoring and truncation*. Academic Press, 2017.

[79] R. J. V. de Graaff, "A 1,5000,000 volt electrostatic generator," *Proceeding of the American Physical Society Minutes of the Schenectady Meeting*, no. 38, pp. 1919–1920, 1931.

[80] A. J. Martins and H. M. Pinto, "Van de graaff generator," *Proceedings of the 2nd International Conference on Handson Science, HSci 2005*, pp. 161–168, July 2005.

[81] Thorlabs Inc., "1/2" (12 mm or 13 mm) Travel Motorized Actuators." [Online]. Available: https://www.thorlabs.com/newgrouppage9.cfm?objectgroup_id=1882

[82] P. D. E. Project, *Phelps database*, 2010 (accessed February 27, 2018). [Online]. Available: www.lxcat.net

[83] N. G. Trinh, "Electrode design for testing in uniform field gaps," *IEEE Transactions on Power Apparatus and Systems*, vol. PAS-99, no. 3, pp. 1235–1242, May 1980.

[84] *Hyperion compact*, OPM Optische Präzisionsmesstechnik GmbH, (accessed July 11, 2018). [Online]. Available: http://www.opm-messtechnik.de/download/Hyperion_en.pdf

[85] A. Dobson, *An introduction to generalized linear models*, 2nd ed. New York: Chapman and Hall, 2002.

[86] *Generalized linear model regression*, MathWorks, (accessed July 11, 2018). [Online]. Available: https://www.mathworks.com/help/stats/glmfit.html

[87] *Generalized linear model values*, MathWorks, (accessed July 11, 2018). [Online]. Available: https://www.mathworks.com/help/stats/glmval.html

[88] B. W. Turnbull, "Nonparametric estimation of a survivorship function with doubly censored data," *Journal of the American Statistical Association*, vol. 69, no. 345, pp. 169–173, 1974. [Online]. Available: http://www.jstor.org/stable/2285518

[89] S. Giolo, "Turnbull's nonparametric estimator for interval-censored data," *Technical Reports - Department of Statistics Universidade Federal do Paraná*, 2004.

[90] C. Kelley, *Iterative Methods for Optimization*. Society for Industrial and Applied Mathematics, 1999. [Online]. Available: https://epubs.siam.org/doi/abs/10.1137/1.9781611970920

[91] B. Efron, "Bootstrap methods: Another look at the jackknife," *The Annals of Statistics*, vol. 7, no. 1, pp. 1–26, 1979. [Online]. Available: http://www.jstor.org/stable/2958830

[92] F. E. Harrell, Jr., *Regression Modeling Strategies : With Applications to Linear Models, Logistic and Ordinal Regression, and Survival Analysis*, 2nd ed., ser. Springer Series in Statistics, 2015.

[93] M. H. Key, C. L. S. Lewis, J. G. Lunney, A. Moore, T. A. Hall, and R. G. Evans, "Pulsed-x-ray shadowgraphy of dense, cool, laser-imploded plasma," *Phys. Rev. Lett.*, vol. 41, pp. 1467–1470, Nov 1978. [Online]. Available: https://link.aps.org/doi/10.1103/PhysRevLett.41.1467

[94] G. D. Peppas, V. P. Charalampakos, E. C. Pyrgioti, M. G. Danikas, A. Bakandritsos, and I. F. Gonos, "Statistical investigation of ac breakdown voltage of nanofluids compared with mineral and natural ester oil," *IET Science, Measurement Technology*, vol. 10, no. 6, pp. 644–652, 2016.

[95] M. J. Given, M. P. Wilson, I. V. Timoshkin, S. J. MacGregor, T. Wang, M. A. Sinclair, K. J. Thomas, and J. M. Lehr, "Modifications to the von laue statistical distribution of the times to breakdown at a polymer-oil interface," *IEEE Transactions on Dielectrics and Electrical Insulation*, vol. 24, no. 4, pp. 2115–2122, 2017.

Appendix A

Test Circuit

Figure A.1 show the full size picture of the test circuit schematics.

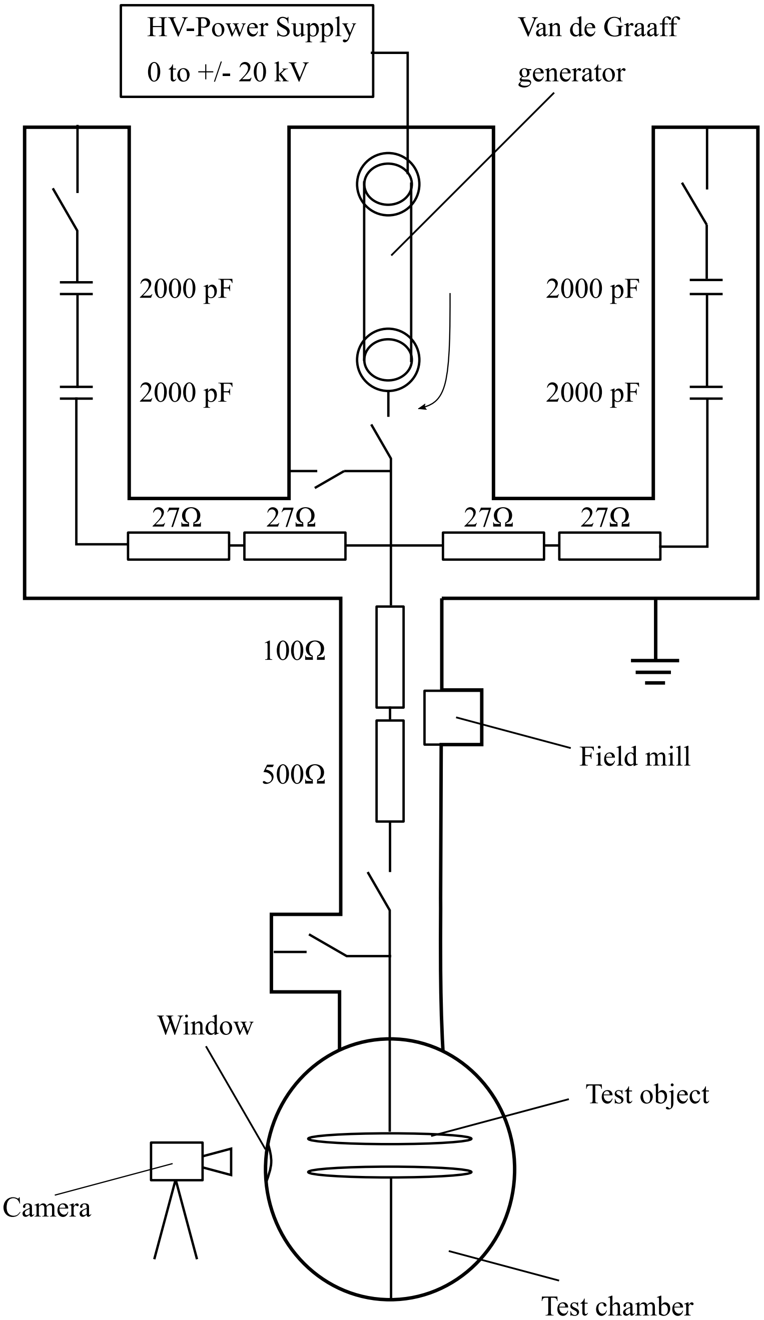

Figure A.1: Schematic of the test circuit used.

Appendix B

Accuracy of Using 100 shots

As discussed in Section 6.3, the plots within were cut to better show the oscillation around the final value. When considering the *uncut* plot, see Figure B, the resulting E_{50} after 60-65 shots is close to the E_{50} of 500 shots.

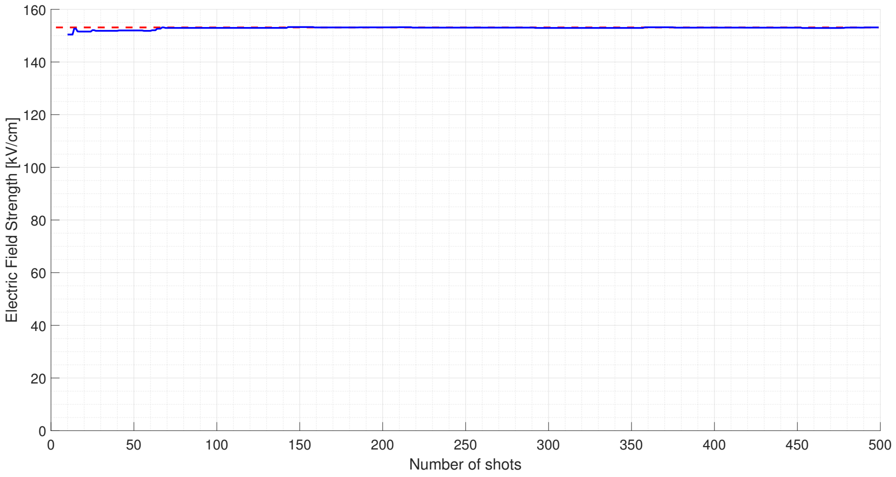

Figure B.1: E_{50} as a function of number of shots evaluated in the chronological order tested. Figure 6.5a without cutting the y-axis.

Appendix C

Interesting Photographs

As approximately 30 000 photos were taken during this thesis, there were a lot of photos with interesting observations. Some of the more interesting were included in the main text, while some more will be added in the following without any order or explanation.

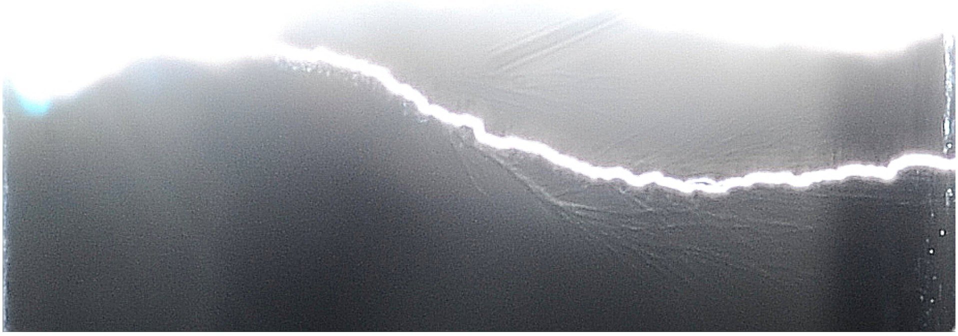

Figure C.1: SF_6, positive needles at 0.5 mm

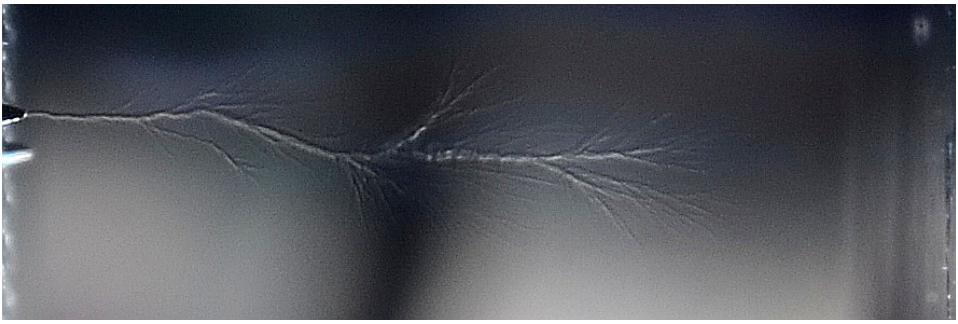

Figure C.2: SF_6, positive needles at 0.5 mm

Figure C.3: SF_6, positive needles at 2 mm

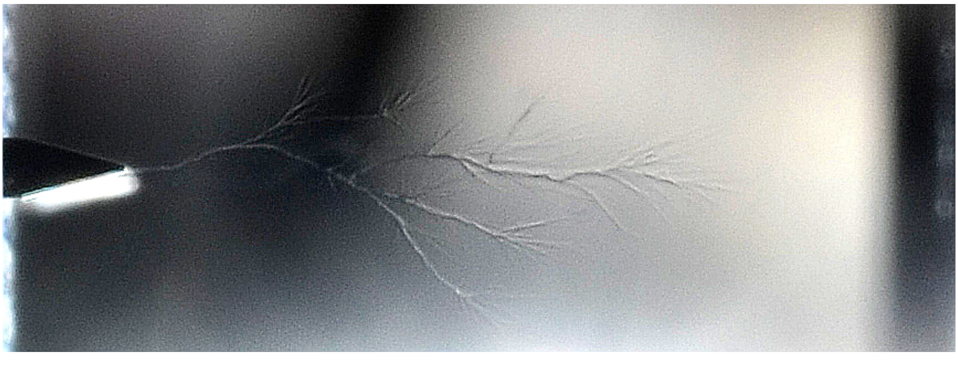

Figure C.4: SF_6, positive needles at 2 mm

Figure C.5: SF_6, negative needles at 0.2 mm

Figure C.6: SF_6, negative needles at 1 mm

Figure C.7: SF_6, positive needles at 2 mm

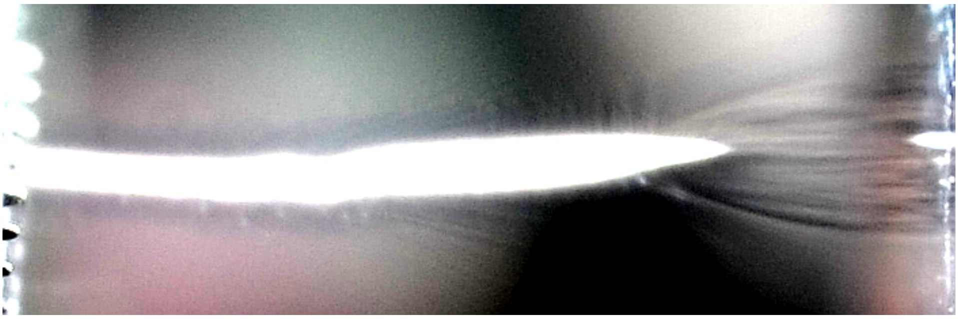

Figure C.8: SF_6, negative needles at 0.2 mm

Figure C.9: SF_6, negative needles at 0.75 mm

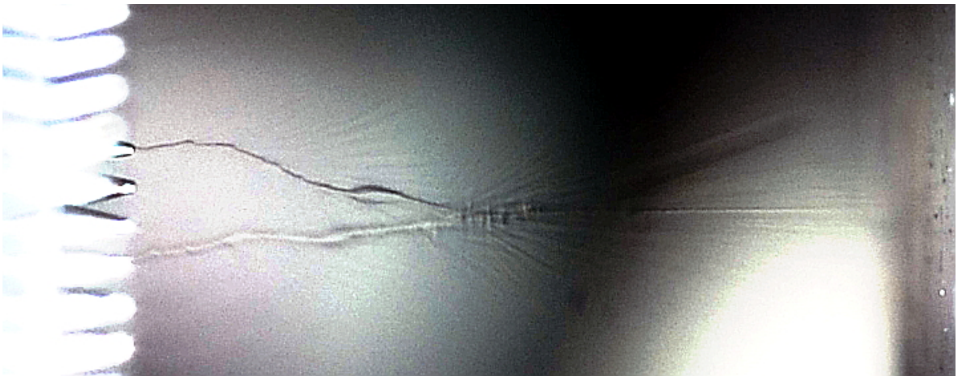

Figure C.10: SF_6, negative needles at 0.75 mm

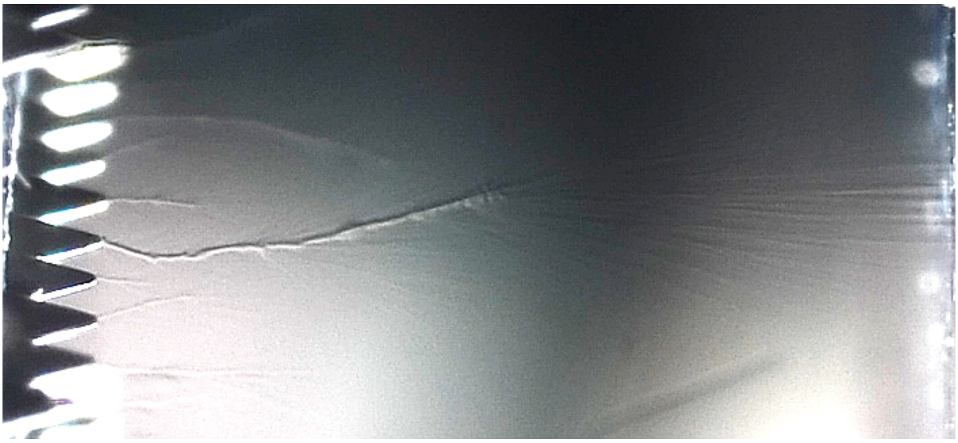

Figure C.11: SF_6, negative needles at 1 mm

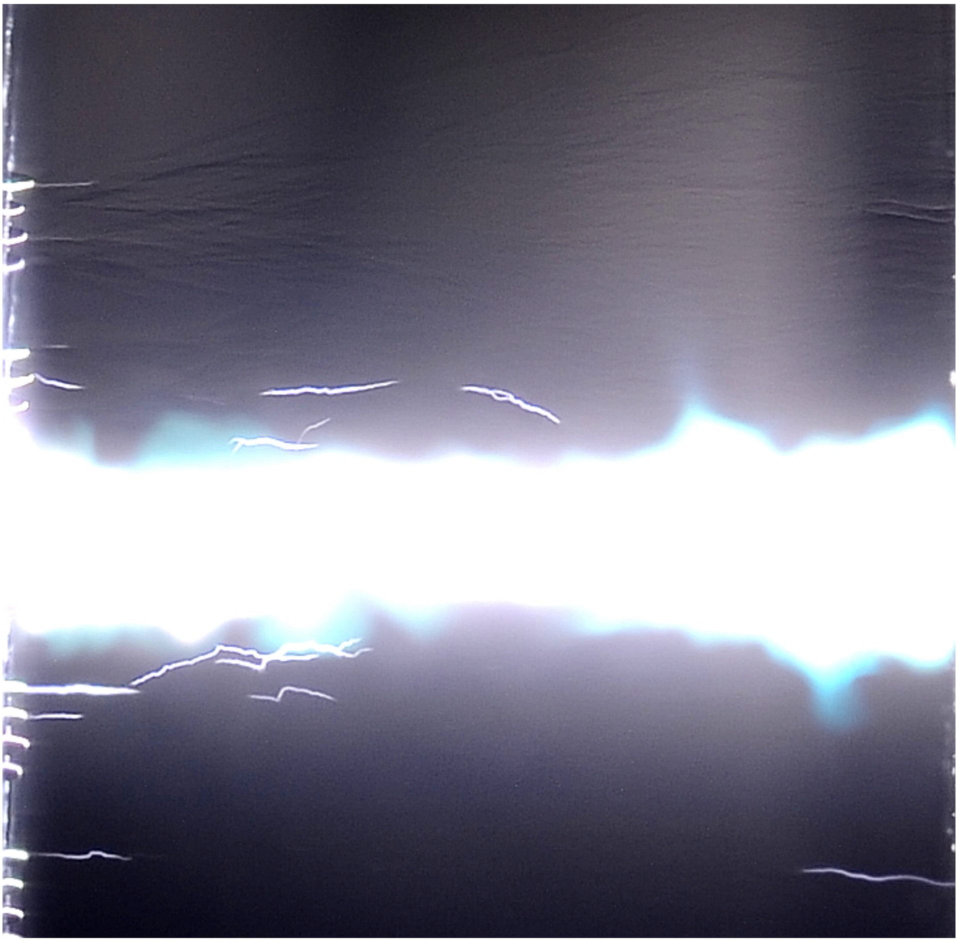

Figure C.12: CO_2, negative needles at 0.2 mm

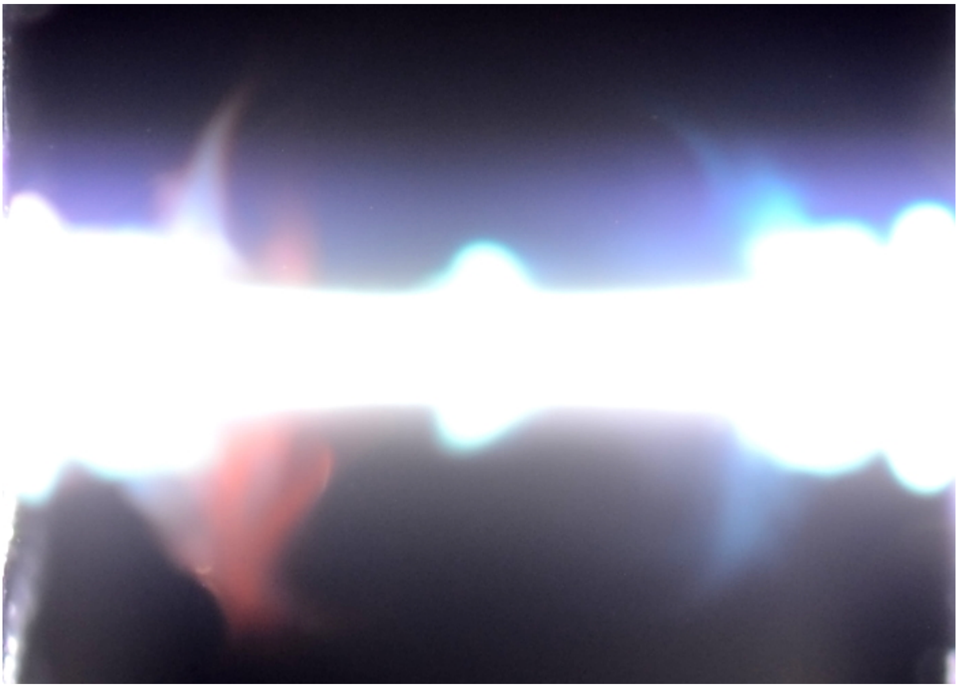

Figure C.13: Colors visible in CO_2. Possibly decomposed CO_2 giving color when returning from excited state.

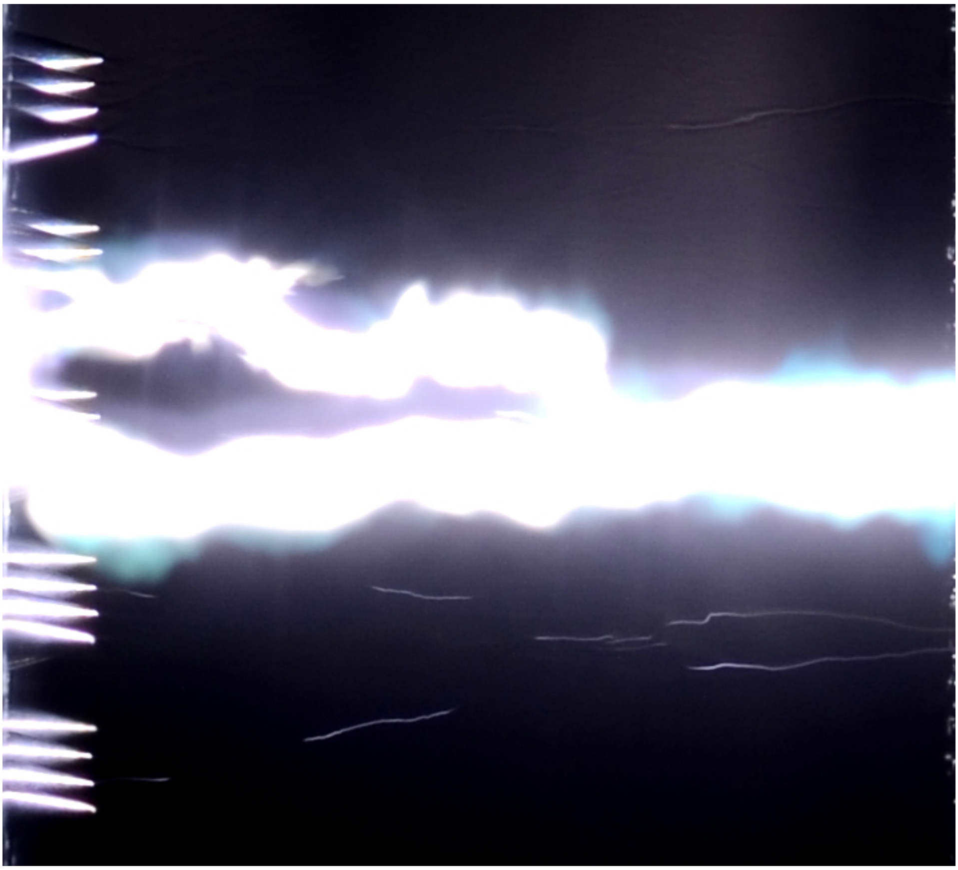

Figure C.14: CO_2, negative needles at 1 mm

Figure C.15: CO_2, positive needles at 1 mm

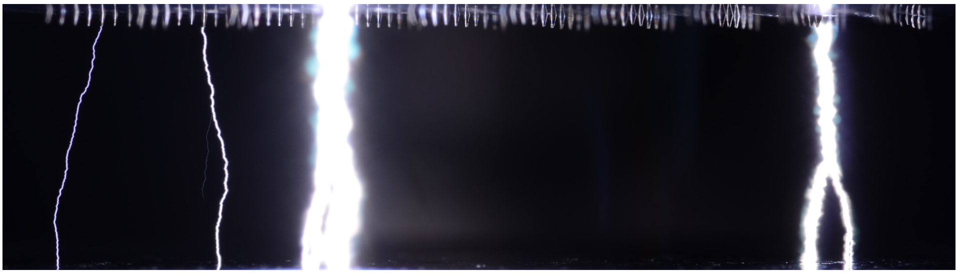

Figure C.16: CO_2, positive needles at 0.5 mm